MIT/PCM-based RF Switches for Tunable Filter Application

by

Junwen Jiang

A thesis

presented to the University of Waterloo

in fulfillment of the

thesis requirement for the degree of

Doctor of Philosophy

In

Electrical and Computer Engineering

Waterloo, Ontario, Canada, 2019

Examining Committee Membership

The following served on the Examining Committee for this thesis. The decision of the Examining Committee is by majority vote.

External Examiner	Ke-Li Wu Professor
Supervisor(s)	Raafat R. Mansour Professor
Internal Member	John Long Professor
Internal Member	Guoxin Miao Associate Professor
Internal-external Member	Eihab Abdel-Rahman Associate Professor

Author’s Declaration

I hereby declare that I am the sole author of this thesis. This is a true copy of the thesis, including any required final revisions, as accepted by my examiners.

I understand that my thesis may be made electronically available to the public.

Abstract

Tunable filters are promising for reducing the size of communication systems by replacing switch filter bank, also they are gaining more attention for satellite applications which will need to change the frequency bands. One of the main requirements for tunable filters is to maintain low passband insertion loss and high stopband rejection over the tuning range. The key to achieving this goal is using high quality factor (high-*Q*) resonators such as three-dimensional (3D) structure resonators (dielectric resonators, coaxial resonators, waveguide resonators, etc.). For high-*Q* tunable filters, not only do the resonators need to have high unloaded *Q*, the tuning elements also need to have low loss. Over the past years, various tuning techniques have been employed to realize tunable filters, including solid-state tuning, mechanical tuning, piezoelectric tuning, magnetic tuning, and MEMS tuning. All of these techniques have both advantages and drawbacks in terms of insertion loss, DC power consumption, tuning speed, non-linearity, and reliability.

The objective of the research presented in this thesis is to investigate the feasibility of using metal-insulating transition (MIT) material and phase-change material (PCM) to realize high-*Q* tunable/ reconfigurable filters for base station in communication and satellite applications. Fabrication methods of MIT material VO_2 (Vanadium Dioxide) and PCM GeTe (Germanium Telluride) are first investigated to obtain optimal MIT/PCM materials with high resistivity ratio between different states. RF switches based on both VO_2 and GeTe integrated with micro-heaters are then developed. VO_2-based variable attenuators are realized at both X-band and Ka-band. A switch capacitor bank is also designed and fabricated, integrating GeTe RF switches and MIM (metal-insulator-metal) capacitors in a six-layer microfabrication process.

A novel structure for wideband dielectric substrate-based filters is developed. The cavity of the filter is separated into two thin dielectric substrates (DSs), a metal frame for holding the dielectric substrates, and two metal covers. The filter is compact in size and ideal for integration with antennas because of its relatively thin profile. Since it uses separated DSs attached to the two sides of the metal frame, the input/output probe can be placed at the middle of the cavity, leading to a significant increase in the input/output coupling compared to conventional dielectric resonator filters.

Additionally, the filter structure lends itself to realizing relatively large values of inter-resonator coupling. A five-pole Chebyshev filter with a fractional bandwidth of 9.6%, a four-pole filter having two transmission zeros with a fractional bandwidth of 9%, and a three-pole filter with a fractional bandwidth of 13% are designed, fabricated and tested. The filter structure promises to be useful in sub-6 GHz 5G base station applications that require the use of low-cost, miniature, high-*Q* wideband filters with a thin profile.

Furthermore, a novel tuning structure with multiple strip lines is developed in this work. The tuning structure is designed to employ RF switches to tune 3D filters, eliminating the need to use variable capacitor loading, which is known to degrade the filter's loaded *Q* over the tuning range. Two- and three-pole filters with combline configuration are designed, fabricated and measured with wire bonding, MEMS switches, and VO_2 switches. With wire bonding, all of the tuning states demonstrate measured *Q* higher than 2000, whereas with the fabricated VO_2 switches, the measured *Q* was lower. The test data confirm however the tunability and feasibility of using the proposed tuning scheme to realize a reasonable high-*Q* tunable filters that maintain *Q* values over the tuning range. A DS-loaded three-pole tunable filter is designed, fabricated, and measured. The results show the potential of realizing a tunable dielectric filter with a low loss VO_2-based switch.

Acknowledgements

I would like to sincerely thank my supervisor Dr. Raafat Mansour, for all his support throughout my cherished years at the University of Waterloo. His guidance and advice have had a major impact on the outcome of this thesis.

I am also so grateful to have the full support by my parents, my wife (C. Feng) and my lovely son. With their encouragement and accompany, I had a wonderful time during my Ph.D. study and allowed me to meet this important goal in my life.

I would also like to say thank you to the members of my committee, Professor John Long, Professor Guoxin Miao, and Professor Eihab Abdel-Rahman for the knowledge they provided during my research and Professor Ke-Li Wu from the Chinese University of Hong Kong for taking the time to serve as my external examiner.

I also want to deeply acknowledge the special people who have become my friends during these years and their kindness and support have contributed a great part to my life.

Table of Contents

Examining Committee Membership ii

Author's Declaration iii

Abstract iv

Acknowledgements vi

List of Figures xi

List of Tables xix

List of Abbreviations xx

Chapter 1 Introduction 1

1.1 Motivation 1

1.2 Objectives 2

1.3 Thesis Outline 3

Chapter 2 Literature Survey 4

2.1 Properties and Fabrication Methods of VO_2 5

2.1.1 VO_2 Properties 5

2.1.2 VO_2 Phase Transition Mechanism 7

2.1.3 VO_2 Deposition Techniques 9

2.2 Properties and Fabrication Methods of GeTe 13

2.2.1 Properties of GeTe 13

2.2.2 Deposition Methods of GeTe 14

2.3 Applications of VO_2 and GeTe 15

2.3.1 VO_2/GeTe-based RF Switches 15

2.3.2 VO_2 and GeTe-based RF Tunable Filters 17
2.3.3 Other Reconfigurable Applications 22
2.3.4 Comparing MEMS and MIT/PCM Switches 22
2.4 High-*Q* Tunable Filters 24
Chapter 3 MIT/PCM-based RF Switches and Reconfigurable RF Passive Devices 29
3.1 VO_2-based Series and Parallel RF Switches 29
3.1.1 Introduction 29
3.1.2 VO_2 Deposition and Characterization 30
3.1.3 Design and Fabrication 34
3.1.4 Simulation and Measurement Results 38
3.1.5 Summary 40
3.2 VO_2-based Variable Attenuator 40
3.2.1 Introduction 40
3.2.2 Design and Fabrication 41
3.2.3 Simulation and Measurement Results 43
3.2.4 Summary 49
3.3 GeTe-based RF Switches 49
3.3.1 Design and Fabrication 49
3.3.2 Simulation and Measurement Results 52
3.3.3 Summary 55
3.4 GeTe-based 4-Bit Capacitor Bank 55
3.4.1 Introduction 55

3.4.2 Design and Fabrication 56
3.4.3 Simulation and Measurement Results 60
3.4.4 Summary 63
Chapter 4 Wideband Dielectric Substrate-based Cavity Filter 64
4.1 Introduction 64
4.2 Proposed Compact DS-loaded Cavity Resonator 66
4.2.1 Comparing Proposed Structure with Other DS-loaded Cavity Resonator Structures 67
4.2.2 Choosing DS Thickness 71
4.2.3 Inter-resonator Coupling 72
4.2.4 Advantages of Assembly for the Proposed Structure 74
4.3 Two-pole Filter with Vertical Coupling 75
4.4 Five-pole Filter with Parallel Coupling 77
4.5 Four-pole Filter with Transmission Zeros 79
4.6 *Q* Improvement with Teflon Holding Structure 82
4.6.1 Possible Factors that Decreased the *Q* Factor 82
4.6.2 Teflon Holding Structure for Resonator and a Three-pole Filter 83
4.7 Discussion 88
4.8 Summary 89
Chapter 5 VO_2-based Tunable Filters 90
5.1 Introduction 90
5.2 Tunable Combline Filters 91
5.2.1 Design and Simulation Results of Tunable Combline Filters 91

5.2.2 Measurement Results with Wire Bonding 97
5.2.3 Measurement Results with MEMS Switches 100
5.2.4 Measurement Results with VO_2 Switches 101
5.2.5 Insertion Loss Discussion 105
5.2.6 Power Handling Discussion 108
5.3 Tunable Dielectric Substrate-based Filter 112
5.3.1 Design and Simulation Results 113
5.3.2 Measurement Results with Wire Bonding 115
5.3.3 Measurement Results with VO_2 Switches 117
5.4 Summary 117
Chapter 6 Conclusion 119
6.1 Contributions of the Thesis 119
6.2 Future Work 121
Bibliography 122

List of Figures

Figure 2-1. Metal-insulator-transition temperature (T_{MIT}) of selected oxides (bulk crystals) [23]. 5

Figure 2-2. a) Resistivity vs. temperature for a VO_2 film deposited by PLD [9]; b) sheet resistance vs. temperature for a 600-nm-thick VO_2 deposited by RF sputtering [11]. 6

Figure 2-3. Crystallographic structures of VO_2: (a) metallic (rutile) structure above T_{MIT}; (b) insulated (monoclinic) structure below T_{MIT}. Large and small spheres denote vanadium (V) and oxygen (O) atoms, respectively **Error! Reference source not found.**. 7

Figure 2-4. Phase diagram of vanadium oxide system [44]. 10

Figure 2-5. Effect of different oxygen flow rates on performance [45]. 11

Figure 2-6. Effect on resistivity ratio caused by different substrate temperatures during deposition [46]. 11

Figure 2-7. (a) DC sputtering apparatus; (b) RF sputtering apparatus; (c) magnetron sputtering apparatus [53][54]. 12

Figure 2-8. Typical experimental arrangement for PLD [53]..... 13

Figure 2-9. Diagram showing heat profiles used to switch between two phases [4]..... 14

Figure 2-10. Measurement results of: a) pulse voltage to amorphized; b) pulse voltage to crystallize [4]. 14

Figure 2-11. Potential applications of VO_2 [23]. 16

Figure 2-12. (a) Layout of fabricated tunable bandpass filter; (b) overscale view of one tunable element [15]..... 17

Figure 2-13. Simulated (dotted lines) and measured (solid lines) insertion (a) and return losses (b) of tunable filter [15]. 18

Figure 2-14. Tunable band stop filter: (a) optical image of the band stop filter; (b) measured S21 versus simulated S21 [17]. 19

Figure 2-15. Tunable cavity filter with VO_2: (a) design configuration of a resonator; (b) measured results for a two pole filter [65]. 20

Figure 2-16. (a) Image of bandpass filter; (b) measurement and simulation results [66]. 21

Figure 2-17. Tunable microstrip line bandpass filter with GeTe: (a) image of fabricated filter; (b) measured results [67]. 22

Figure 2-18. ON-state resistance and cut-off frequencies for RF switches using different techniques [69]. 23

Figure 2-19. Tunable combline filter: (a) configuration of resonator; (b) picture of two-pole tunable filter; (c) measured results for two-pole tunable filter [71]. 25

Figure 2-20. (a) Conceptual drawing of all-silicon evanescent-mode cavity filter with tunable center frequency; (b) cross-sectional view of packaged device [72]. 26

Figure 2-21. (a) RF characterization set-up of two-resonator all-silicon BPF; (b) front view of manufactured die of diaphragm; (c) front view of manufactured die of cavity; (d) side view of manufactured die of DC biasing electrode; (e) measured results [72]. 27

Figure 2-22. (a) Half side of tunable two-pole evanescent-mode cavity filter; (b) fabricated picture of tunable evanescent-mode cavity filter with RF-MEMS cantilever-switch capacitance network chip [73]. 27

Figure 2-23. Measured and fitted S-parameters for three filter responses [73]. 28

Figure 3-1. QNC lab AJA sputtering system for RF reactive sputter. 31

Figure 3-2. X-ray diffraction (XRD) pattern for thin-film VO_x: (a) thin-film V_2O_3; (b) thin-film VO_2; (c) thin-film V_2O_5 [74]. 32

Figure 3-3. AFM scanning pictures: (a) thin-film V_2O_3; (b) thin-film VO_2; (c) thin-film V_2O_5. 33

Figure 3-4. Sheet resistance of VO_2 thin-film versus voltage applied to micro-heater. 33

Figure 3-5. Design structure of VO_2-based switches: (a) series switch; (b) parallel switch. 35

Figure 3-6. 3D view of each layer of the designed VO_2-based switches: (a) series switch; (b) parallel switch.....35

Figure 3-7. Copper-based insulator-on-alumina VO_2 fabrication process. 36

Figure 3-8. Fabricated VO_2-based switches: (a) series switch; (b) parallel switch. 37

Figure 3-9. EM simulation results: (a) series switch; (b) parallel switch. 38

Figure 3-10. Measurement results of series switch: (a) switch ON, (b) switch OFF. 38

Figure 3-11. Measurement results of parallel switch: (a) switch ON; (b) switch OFF. 39

Figure 3-12. Measurement and simulation comparison for ON-state insertion loss (S21 ON) and OFF-state isolation (S21 OFF): (a) series switch; (b) parallel switch. 39

Figure 3-13. Schematic of variable attenuator. 41

Figure 3-14. 3D view of each layer of variable attenuator structure. 42

Figure 3-15. Image of fabricated variable attenuator showing dimensions for 30 GHz variable attenuator [85]. 42

Figure 3-16. Graph depicting (a) test structure and (b) sheet resistance (in logarithmic scale) of the VO_2 thin-film versus voltage applied to the micro-heater. 44

Figure 3-17. EM simulation results for 10 GHz variable attenuator: (a) insertion loss; (b) return loss. 45

Figure 3-18. Measurement results for 10 GHz variable attenuator: (a) insertion loss; (b) return loss. 46

Figure 3-19. EM simulation results for 30 GHz variable attenuator: (a) insertion loss; (b) return loss. 47

Figure 3-20. Measurement results for 30 GHz variable attenuator: (a) insertion loss; (b) return loss. 48

Figure 3-21. 3D view for each layer of designed GeTe-based series switch. 50

Figure 3-22. Image of fabricated GeTe series switch. 51

Figure 3-23. Fabrication process for GeTe-based series switch. 52

Figure 3-24. Simulation results for W_heater = 4 μm: (a) switch OFF; (b) switch ON. 53

Figure 3-25. Simulation results for W_heater=15 μm: (a) switch OFF; (b) switch ON. 54

Figure 3-26. Measurement results for W_heater=4 μm: (a) switch OFF; (b) switch ON. 54

Figure 3-27. Measurement results for W_heater=15 μm: (a) switch OFF; (b) switch ON. 55

Figure 3-28. Schematic of 4-bit capacitor bank. 57

Figure 3-29. Fabrication process for Ge-Te-based switched capacitor bank [93]. 58

Figure 3-30. Simulation model for 4-bit capacitor bank. 59

Fig. 3-31. Image of fabricated 4-bit capacitor bank. 59

Figure 3-32. Simulation results for 4-bit capacitor bank. 61

Figure 3-33. Circuit model for 4-bit capacitor bank. 62

Figure 3-34. Measurement results for 4-bit capacitor bank. 62

Figure 3-35. Measurement results plotted on a Smith chart. 63

Figure 4-1 3D diagram of proposed DR-loaded cavity resonator. 66

Figure 4-2 Image of the dielectric substrate. (a) DSs not diced; (b) DSs diced. 67

Figure 4-3 Diagram (a) and electrical field of the used resonance mode (b) of the proposed DR loaded cavity resonator. 67

Figure 4-4 Several structures for DS-loaded cavity resonators. (a)-(g) is a side view of the resonators and (a')-(g') is the 3D view of the resonators. 69

Figure 4-5 Input group delay of structure (e), (f), and (g) in Figure 4-4 with one port EM simulation. 70

Figure 4-6 Change of parameters versus different thicknesses of DS: (a) change of resonance frequency; (b) change of *Q*; (c) change of spurious free window. 72

Figure 4-7 Electrical field of the coupled resonator in vertical coupling, (a) 3D view of the arrangement of the coupling resonators; (b) first mode; (c) second mode. 73

Figure 4-8 Electrical field of coupled resonator in vertical coupling: (a) 3D view of coupling resonator arrangement; (b) first mode; (c) second mode. 73

Figure 4-9 Side view of the metal frame when the DS is mounted. 74

Figure 4-10 Eigenmode simulation for resonance frequency: (a) resonance frequency versus DS misalignment along y axis (Shift_y); (b) resonance frequency versus DS misalignment along z axis (Shift_z). 74

Figure 4-11 3D diagram of the two-pole filter. 75

Figure 4-12 Picture of the fabricated two-pole filter, (a) disassembled filter; (b) assembled filter. 76

Figure 4-13 EM simulation model for the two-pole filter. 76

Figure 4-14 Simulation and measurement results of two-pole filter with larger span. 76

Figure 4-15 3D diagram of five-pole filter. 77

Figure 4-16 Picture of fabricated five-pole filter: (a) disassembled filter and (b) assembled filter (total size 17 mm × 14 mm × 53 mm). 78

Figure 4-17 EM simulation model for five-pole filter. 78

Figure 4-18 Simulation and measurement results of five-pole filter with larger span. 79

Figure 4-19 3D diagram of four-pole filter. 80

Figure 4-20 Picture of the fabricated four-pole filter, (a) disassembled filter; (b) assembled filter... 80

Figure 4-21 EM simulation model for four-pole filter. 81

Figure 4-22 Simulation and measurement results of four-pole filter. 81

Figure 4-23 EM simulation model with silver paste, (a) 3D view; (b) front view. 82

Figure 4-24. *Q* versus thickness of silver paste layer with EM simulation. 83

Figure 4-25. EM simulation model for a resonator. 84

Figure 4-26. Image of the resonator with the Teflon support. (a)the Teflon support; (b) DS mounted on middle frame with Teflon holding structure and Teflon screw; (c) disassembled resonator..... 84

Figure 4-27 Simulated return loss for the resonator..... 85

Figure 4-28 Measured results for the resonator: (with Teflon holding structures. 85

Figure 4-29 Three-pole filter: (a) EM simulation Model, (b) fabricated filter. 86

Figure 4-30 Simulation and measurement results of the three-pole filter with Teflon holding structure. 87

Figure 4-31 Measurement results of the three-pole filter with silver paste. 87

Figure 5-1 Proposed structure for tunable combline filter. 92

Figure 5-2 Image of tunable combline filter. 92

Figure 5-3. Electrical field of resonator for different states: (a) state 1 with both strip lines not connected to the ground, (b) state 3 with both strip lines connected to the ground with wire bond.... 93

Figure 5-4 Tuning structure configuration: (a) 2-bit tuning structure (b) 4-bit tuning structure. 93

Figure 5-5 PCB of 4-bit tuning structure with Omron MEMS switches, 18mm x 18mm in size..... 94

Figure 5-6 Simulation results for 2-bit tuning structure with wire bond connection. 95

Figure 5-7 EM simulation results for 4-bit tuning structure with MEMS switches. 95

Figure 5-8 EM simulation model for three-pole tunable filter..... 96

Figure 5-9 Image of three-pole combline filter. 96

Figure 5-10 Simulation results for three-pole filter with wire bond connection..... 97

Figure 5-11 Measured results for 2-bit tuning structure with wire bond connections. 98

Figure 5-12 Measured results with wire bonding. 99

Figure 5-13 Measured results with wire bonding large span. 99

Figure 5-14 Measured insertion loss for 4-bit tuning structure using MEMS switches. 100

Figure 5-15 Measured return loss for 4-bit tuning structure using MEMS switches. 100

Figure 5-16 Six-layer fabrication process for VO_2. 101

Figure 5-17 Mask of six-layer process. 102

Figure 5-18 Picture of fabricated VO_2 switch for tunable filters. 103

Figure 5-19 Hysteresis curve of thin-film VO_2. 103

Figure 5-20 Image of two-pole tunable filter assembled with VO_2 switches. 104

Figure 5-21 Measured results for two-pole combline filter with VO_2 switches. 104

Figure 5-22 Measured results for two-pole combline filter with VO_2 switches with large span 105

Figure 5-23 Insertion loss when assigning different R_s. 106

Figure 5-24 Simulation results when assigning different R_s. 106

Figure 5-25 Simulated results with R_s assigned to 2 Ω, 10 Ω, and 50 Ω. 107

Figure 5-26 Measured results with voltage across micro-heater at 5V, 4.5V and 4.2V. 107

Figure 5-27 Simulation model showing port locations. 108

Figure 5-28 Simulation schematic with 6 ports. 109

Figure 5-29 Top view of the simulation port setup for the two-pole filter. 110

Figure 5-30 Simulated results with R_s assigned to 1 Ω, 4 Ω, 7 Ω and 10 Ω. 110

Figure 5-31 Simulated results with R_s assigned to 1 kΩ, 10 kΩ, 100 kΩ and 1 MΩ. 111

Figure 5-32 Dielectric substrates as ordered. 112

Figure 5-33 Diced dielectric substrates. 112

Figure 5-34 3D diagram of three-pole tunable filter. 113

Figure 5-35 EM simulation model of three-pole tunable filter. 114

Figure 5-36 Simulation results for three-pole tunable filter. 114

Figure 5-37 Image of fabricated three-pole tunable filter: (a) VO_2 switch on PCB; (b) full image of DSs and VO_2 switch assembled on PCB; (c) PCB on a cover; (d) assembled filter 115

Figure 5-38 Measured results with wire bonding. 116

Figure 5-39 Measured results with wire bonding. 116

Figure 5-40 Measured results with VO_2 switch: (a) insertion loss; (b) return loss. 117

List of Tables

Table 2-1. VO_2-based RF switches..... 15

Table 2-2. GeTe-based RF switches..... 15

Table 2-3 Operating parameter comparison among MEMS, VO_2 and GeTe [69]. 24

Table 3-1. VO_2 deposition parameters 32

Table 3-2. Summary of W and GeTe deposition parameters 60

Table 4-1 EM simulation results of different structures..... 70

Table 4-2 VO_2-based RF switches..... 88

Table 5-1 Simulation results for three-pole combline filter 97

Table 5-2 Measurement results for 2-Bit tuning structure..... 98

Table 5-3 Measurement results for three-pole combline filter with wire-bonding..... 99

Table 5-4 Measurement results for two-pole combline filter with VO_2 switches 105

Table 5-5 Simulation results for three-pole tunable filter 114

Table 5-6 Measured results for three-pole tunable filter with wire bonding..... 116

List of Abbreviations

ADS	Advance Design System
AFM	Atomic Force Microscopy
DC	Direct Current
DS	Dielectric Substrate
EM	Electromagnetic
FET	Field-effect Transistor
GeTe	Germanium Telluride
HFSS	High Frequency Structure Simulator
MEMS	Microelectromechanical Systems
MIM	Metal-air-metal
MIT	Metal-insulator Transition
PCB	Printed Circuit Board
PCM	Phase Change Material
PECVD	Plasma-enhanced Chemical Vapor Deposition
PLD	Pulsed Laser Deposition
PVD	Physical Vapor Deposition
Q	Quality Factor
RF	Radio Frequency
RIE	Reactive-ion Etching
RRU	Remote Radio Units
VO2	Vanadium dioxide
XRD	X-ray Diffraction
TM	Transverse Megnetic

Chapter 1
Introduction

1.1 Motivation

High-*Q* tunable filters are particularly promising components for the base station of modern multiband wireless communication systems and satellite applications. The need for tunability and reconfigurability in wireless communication systems is due to the vast numbers of bands that are packed in each system, resulting in a significant increase in the number of filters required. However, the availability and implementation of tunable filters may significantly reduce how many filters are needed, thus resulting in significant size and cost reductions in certain wireless communication systems.

Tunable filters can also reduce costs for the network operator in the following way. Consider a remote radio units (RRU) installed on top of standard 15-storey communication towers. After serving only a few years, the frequency or bandwidth of the wireless system needs to be changed. With tunable/reconfigurable hardware, the change can be done remotely without reinstalling the RRU. Reduction in mass is especially important for decreasing launching costs for satellite

applications. Tunable/reconfigurable filters can help simplify satellite systems by reducing mass and size while still meeting the necessary requirements.

The main critical requirements for tunable filters are high-*Q*, out-of-band rejection, tuning range, size, power handling, linearity, and tuning speed. In order to achieve a high-*Q* tunable filter, the resonators need to be high-*Q* and the tuning element must be relatively low loss.

Over the years, various tuning techniques have been applied to tunable filters, including mechanical tuning, magnetic tuning, piezoelectric tuning, and MEMS tuning. Mechanical tuning can realize high-*Q* and is easy to implement, but it is a bulky approach and results in low tuning speeds. Ferrite-based magnetic tuning offers a fast switching speed and can handle high power, but it is also a bulky approach and suffers from high DC power consumption. Piezoelectric tuning possesses the advantages of mechanical tuning and a relatively small size, but it offers only a limited tuning range [2]. On the other hand, MEMS tuning is known to have low loss, high power handling, and high linearity. However, reliability is still an problem with RF MEMS devices.

To address this challenge, metal-insulating transition (MIT) material such as VO_2 and phase-change material (PCM) such as GeTe will be investigated as tuning elements. MIT/PCM-based tuning elements offer low loss, fast tuning speed, low power consumption, and high reliability. In addition, they are easily amenable of monolithic integration with a wide range of tunable RF devices such as tunable filters, phase shifters, impedance tuners and variable attenuators.

1.2 Objectives

The objective of the research presented in this thesis is to investigate the feasibility of using metal-insulating transition (MIT) material and phase-change material (PCM) to realize high-*Q* tunable or reconfigurable filters. The ultimate objective is to realize high-*Q* tunable filters through the integration of high-*Q* 3D resonators with MIT/PCM-based tuning elements.

The research is divided into several main tasks, as follows:

- Development of VO_2 and GeTe RF switches

  This task includes the development of a fabrication process of VO_2 and GeTe films at the University of Waterloo. It involves investigating the development and optimization of a fabrication process for the realization of low loss, high isolation MIT/PCM-based switches.
- Development and demonstration of MIT/PCM tunable devices such as integrated switch capacitor bank and variable attenuators

  The research in this task includes design and development of fabrication processes for realizing tunable passive devices integrated with MIT/PCM switches.
- Development of 3D filters that are easily amenable to integrating with VO_2/GeTe-based tuning elements for the realization of MIT/PCM-based tunable filters.

  This task involves the design and development of tuning structures that employ MIT/PCM switches for tuning 3D filters such as 3D combline filters and dielectric resonator filters.

1.3 Thesis Outline

Following the motivation and objectives presented here in Chapter 1, Chapter 2 provides an overview of the properties, fabrication processes, and applications of metal-insulator-transition material VO_2 and phase-change material GeTe. It also summarizes the work reported in the literature on tunable filters. In Chapter 3, a VO_2 deposition method with RF sputtering is discussed, along with RF switches and variable attenuators realized with thin-film VO_2. This is followed by an overview of GeTe-based RF switches and capacitor banks. Chapter 4 presents a wideband dielectric substrate-based filter. The design, fabrication, and measurement results for three-pole, five-pole, and four-pole filters are presented and discussed, followed by the presentation of a new assembly structure to improve the *Q* of the filter. Tunable filters employing VO_2 switches are introduced in Chapter 5. Two-pole and three-pole tunable combline filters are designed, fabricated, and measured with both commercial RF MEMS switches and VO_2 switches for comparison. A dielectric substrate-based tunable filter employing VO_2 switches is then presented. Finally, a brief summary of the contributions of the thesis with proposed future work is given in Chapter 6.

Chapter 2

Literature Survey

Metal-insulator transition (MIT) materials such as VO_2 and phase-change materials (PCM) such as GeTe are capable of switching between a metal state and an insulator state when subjected to external excitation [3-4]. Both MIT and PCM have gained increasing attention in RF and microwave applications due to their ability to build high-performance RF switches [5-13] and tunable or reconfigurable devices [14-20].

MIT materials have been of interest for more than half a century, when Morin reported the phase transitions in binary transition-metal oxides [22]. Morin concluded that transition-metal oxides such as VO_2, V_2O_2, VO and Ti_2O_3 exhibit increases in resistivity by several orders of magnitude when their temperature drops from high to low across their transmission temperature [23]. Figure 2-1 shows the metal-insulator-transition temperature (T_{MIT}) of some transition-metal oxides. Among these materials, the T_{MIT} of VO_2 (68°C) is near room temperature, which makes it the most-studied strongly correlated MIT material [22].

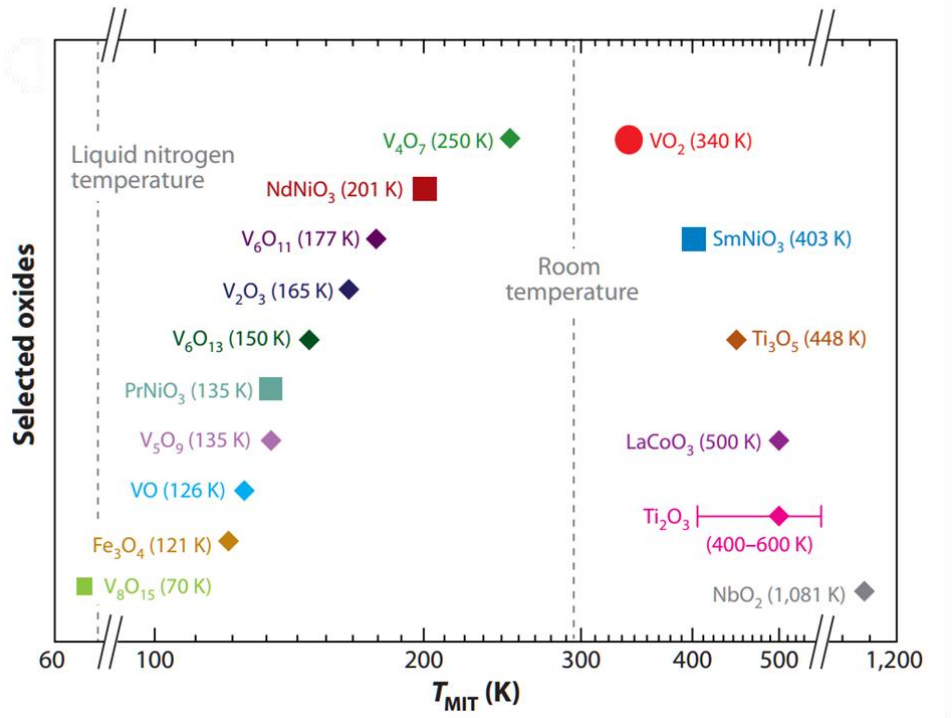

Figure 2-1. Metal-insulator-transition temperature (T_{MIT}) of selected oxides (bulk crystals) [23].

2.1 Properties and Fabrication Methods of VO_2

2.1.1 VO_2 Properties

Vanadium oxide (VO_2) is gaining interest among MIT materials due to the significant change in its resistance during the metal-insulator transition near room temperature (around 68 ℃). A five-order change in resistivity of VO_2 over 0.1 K during MIT was reported by Kucharczyk in 1979 [21]. Figure 2-2 (a) shows the resistivity of a VO_2 film deposited by pulse laser deposition (PLD) when the temperature changes from 25 ℃ to 102 ℃. As can be seen, the resistivity changes from 0.5 Ω·cm to 5×10^{-5} Ω·cm (four orders of magnitude change) [9]. Figure 2-2 (b) shows the sheet resistance of 600-nm-thick VO_2 deposited by RF sputtering when the temperature changes from 20 ℃ to 85 ℃. The sheet resistance undergoes a nearly five-order of magnitude change [11]. The mechanisms of such a transition will be discussed in a later section.

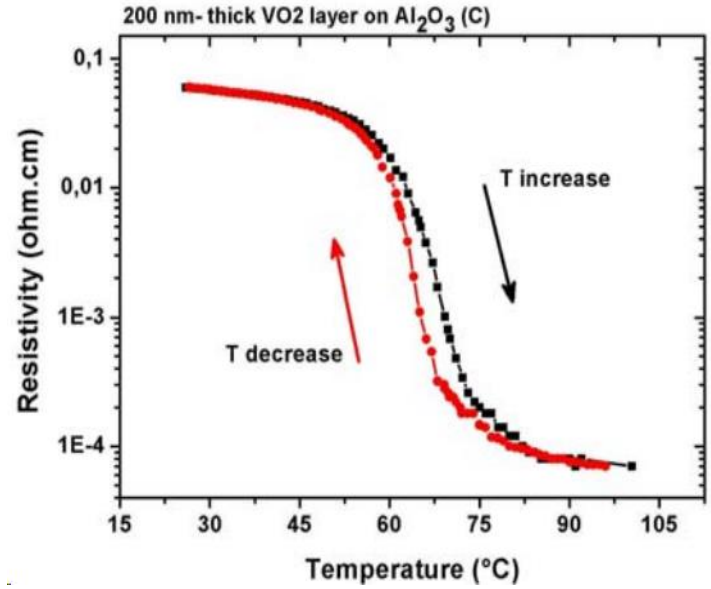

(a)

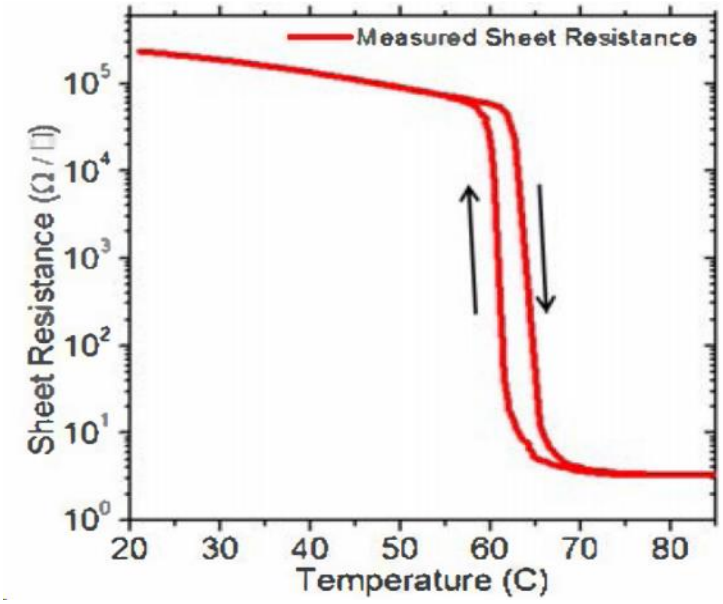

(b)

Figure 2-2. a) Resistivity vs. temperature for a VO_2 film deposited by PLD [9]; b) sheet resistance vs. temperature for a 600-nm-thick VO_2 deposited by RF sputtering [11].

The structural transformation of a crystal lattice from a monoclinic (M1) phase in a low temperature insulator to a tetragonal/rutile (R) phase in a high temperature metal has also been reported during the metal-insulator-transition of VO_2 [24]**Error! Reference source not found.**. The structures of the two states are shown in Figure 2-3**.** Figure 2-3 (a) shows the R phase of VO_2. In this phase, all the V atoms are equally spaced along a linear chain of VO_6 octahedrals parallel to the crystallographic c-axis (c_R), with V-V distances of 2.86 Å. During the MIT from the metallic R phase to an insulating M1 phase, two distinctive sets of V-V distances (2.65 and 3.12 Å) will form due to the pairing and tilting of VO_6 octahedrals, as shown in Figure 2-3 (b).

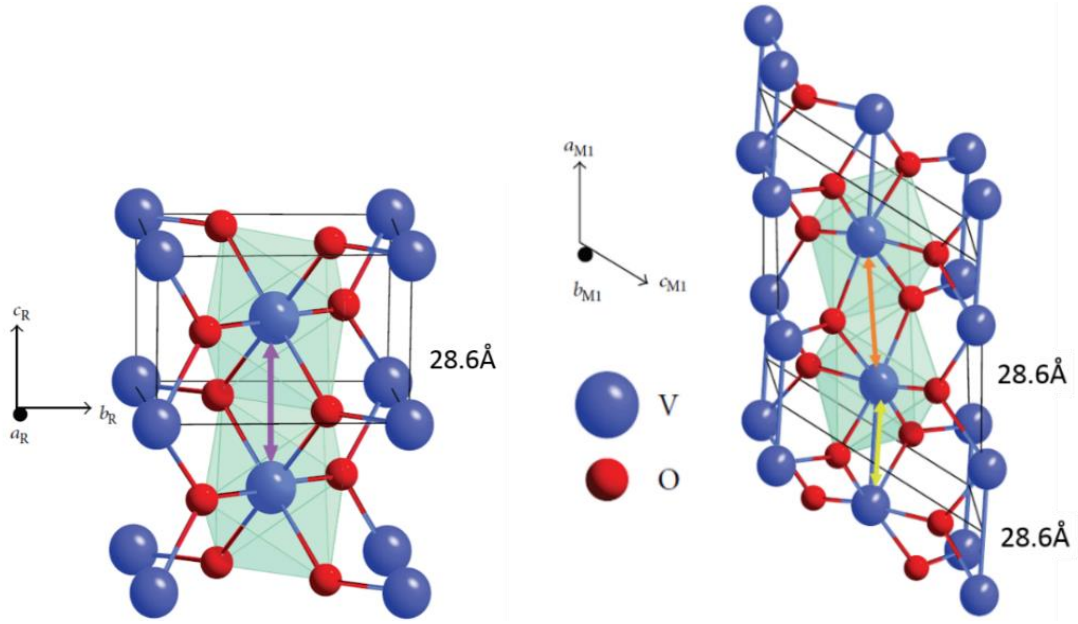

(a) (b)

Figure 2-3. Crystallographic structures of VO_2: (a) metallic (rutile) structure above T_{MIT}; (b) insulated (monoclinic) structure below T_{MIT}. Large and small spheres denote vanadium (V) and oxygen (O) atoms, respectively **Error! Reference source not found.**.

2.1.2 VO_2 Phase Transition Mechanism

There are basically four types of insulators: Bloch-Wilson insulators, Mott-Hubbard insulators, Peierls insulators, and Anderson insulators [21]. Except for Bloch-Wilson insulators, the other three types are all able to perform a metal-insulator transition (MIT). The MIT of Mott-Hubbard

insulators occurs due to electron-electron interactions [26], whereas the MIT of the Peierls insulators is due to electron-phonon interactions [28] and the MIT of Anderson insulators caused by disorder-induced localization [29]. The MIT mechanism of VO_2 is still under debate between Mott-Hubbard-type insulators and a Peierls-type insulators, but recent experimental [30][31] and theoretical [32] research shows that we need to move beyond standard single-band Mott and Peierls transition models.

2.1.2.1 Optical excitation

By using optical excitation, many researchers have reported ultra-fast insulator-to-metal transition at the scale of picoseconds or faster. Becker, et al., realized a 5-ps transition time of sputtered VO_2 thin film using optical pump-probe methods with 780-nm Ti: sapphire laser as a pump source [33]. Cavalleri and colleagues obtained a 100 fs to 50 ps transition time using the same method with 800-nm 50-fs optical pulse as the pump source [34]. Employing a terahertz pump-probe method, Kubler, et al., achieved 130 fs and about 10 ps by using the temporal delay time of the first cycle of electronic conductivity change and the saturation of conductivity change as the criteria for determining the phase transition [35]. Kim, et al., reported a 300-fs transition time by using a time-resolved X-ray diffraction method with a 780-nm 20-fs optical pulse as the pump source [36]. A four-dimensional ultrafast electron microscopy was utilized by Lobastov and his colleagues with a 770-nm femtosecond laser pulse, from which they achieved a 3.1±0.1 ps transition time [37].

In light of these reported results, VO_2 emerges as a possible material to realize ultrafast optical switches. However, most of the results showed an insulator-to-metal transition, while few reports studied the time scales of transition from the metallic state to the insulator state. More investigations on this form of transition need to be done [38]. If such an ultrafast switch were to be electrically excited, it would be able to compete with the current silicon-based logic devices [21].

2.1.2.2 Thermal excitation

Thermal excitation is very straight-forward: simply by heating VO_2 to above 68 ℃, the resistivity drops up to five orders according to the quality of the VO_2 film. The transition temperature (T_{MIT}) can be different due to different substrate and deposition conditions. It can also be changed by doping. As shown in Figure 2-2 (a), when the temperature exceeds 62 ℃, resistivity drops significantly as the temperature increases; after 75 ℃, it becomes almost constant. Hysteresis affects the resistivity of heating and cooling the VO_2 thin film. The temperature span of hysteresis can vary from 0.1 ℃ to 10 ℃ along different substrate orientations [21], [39].

2.1.2.3 Electrical excitation

The electrical field control of VO_2 metal-insulator transition is desirable for fast and reliable electronic devices. Some experiments are done for electrical excitation and to specify whether VO_2 is a Mott-type insulator or a Peierls-type one. Stefanovich et al. demonstrated an experiment to trigger VO_2 metal-insulator transition with an electrical field at room temperature. Their results suggest that the metal-insulator transition in VO_2 is purely an electronic (Mott-Hubbard) transition. They also claimed that the Mott transition in VO_2 should be considered as a "trigger mechanism" that initiates a structural Peierls-like transition, accompanied by a symmetry change from monoclinic to tetragonal [40]. Furthermore, Sieu Ha et al. demonstrated an abrupt drop in insertion loss using both DC voltage and RF power [41].

2.1.3 VO_2 Deposition Techniques

The vanadium oxide system is a large and complex family. Figure 2-4 shows the phase diagram of the vanadium oxide system. In addition to VO_2, there are around 20 different vanadium oxide components, some of which (e.g., V_2O_3 and V_2O_5) also have metal-insulator transition abilities. The transition temperatures for V_2O_3 and V_2O_5 are around -123 ℃ [42] and 280 ℃ [43], respectively. However, most of the vanadium oxide does not have phase-transition ability.

Several vanadium oxides, such as V_2O_3, V_6O_{11}, V_6O_{13}, V_7O_{13}, and V_2O_5, have a V/O ratio close to VO_2, which makes it difficult to deposit high quality (i.e., high purity) VO_2. Oxygen partial pressure and temperature are two key factors in the VO_2 deposition process. Figure 2-5 shows the effect on performance of different oxygen flow rates, while Figure 2-6 illustrates the effect on resistivity ratio due to different substrate temperatures during deposition. Only a well-optimized depositing process can achieve more than three orders of magnitude in resistance change. In order to obtain high quality thin-film VO_2, various technique have been used, such as sputtering [3][10][11][48], pulse laser deposition (PLD) [12][14][15][41], chemical vapor deposition [47], sol-gel coating [49], epitaxial growth [50], and electron beam evaporation [51]. Two of the most popular VO_2 depositions techniques in recent times are sputtering and PLD, which will be reviewed in a later section.

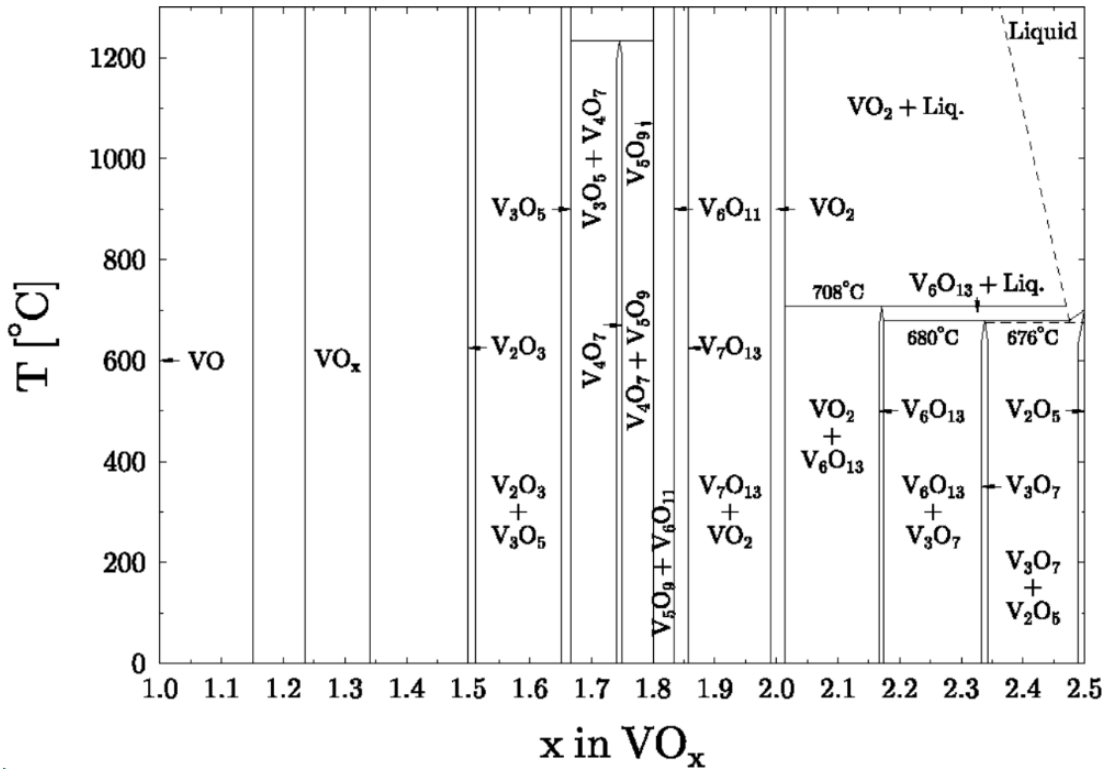

Figure 2-4. Phase diagram of vanadium oxide system [44].

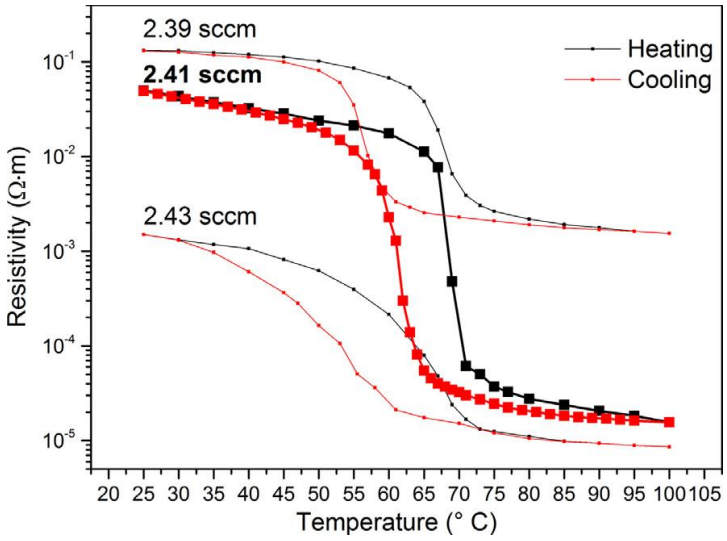

Figure 2-5. Effect of different oxygen flow rates on performance [45].

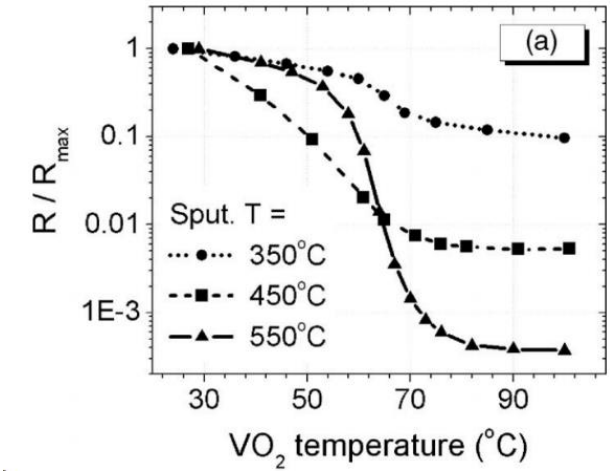

Figure 2-6. Effect on resistivity ratio caused by different substrate temperatures during deposition [46].

2.1.3.1 Sputtering

Sputtering is one of the most commonly used physical vapor deposition (PVD) processes [52]. Figure 2-7 shows three of the more popular methods used for sputtering: DC, RF, and magnetron sputtering. As shown in Figure 2-7, DC sputtering utilizes a DC discharge, and RF sputtering uses a capacitor to set the DC bias and an impedance-matching network coupling to the reactive load. Compared to DC sputtering, RF sputtering can operate at a lower sputtering gas pressure

and lower voltage while producing a higher deposition rate. Magnetron sputtering can use either DC or RF sputtering plus a planar magnetron, which helps both types of sputtering to obtain a higher deposition rate [53].

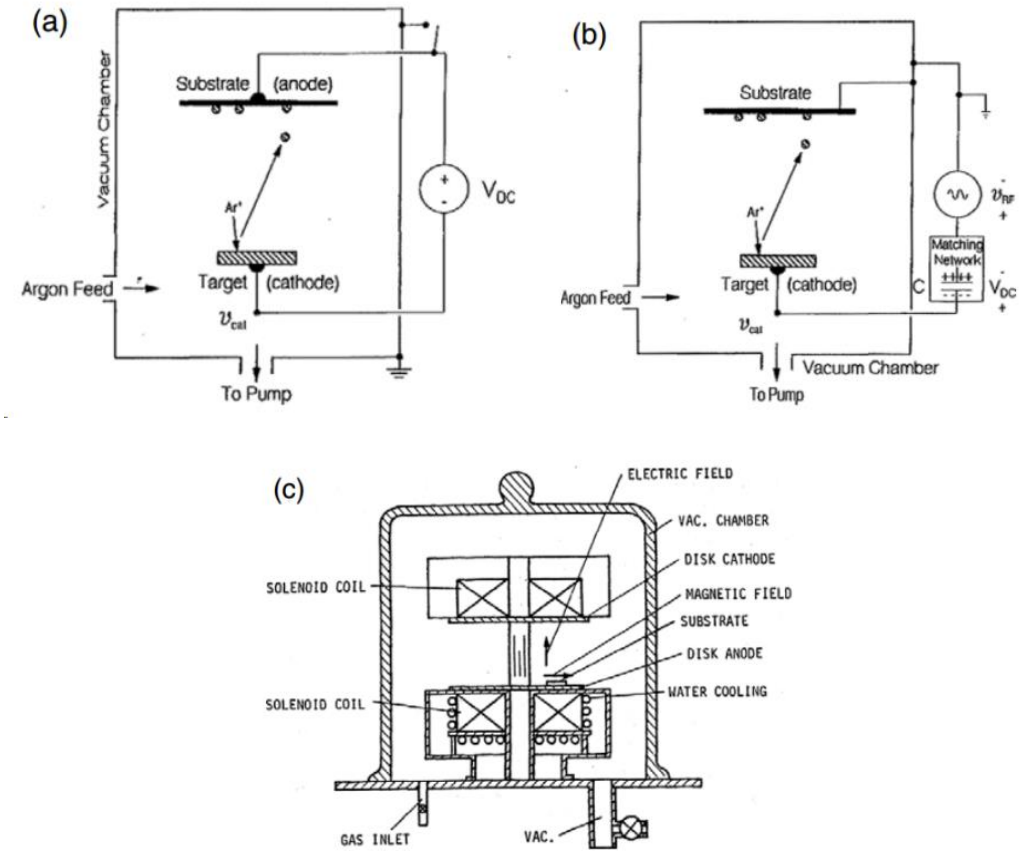

Figure 2-7. (a) DC sputtering apparatus; (b) RF sputtering apparatus; (c) magnetron sputtering apparatus [53][54].

2.1.3.2 Pulsed laser deposition

Pulsed laser deposition (PLD) is a relatively new deposition technique used for oxide growth. A typical experimental arrangement for PLD is shown in Figure 2-8. A high-powered pulsed laser beam is used in PLD, focusing on the target inside a vacuum chamber. The target then vaporizes and a thin film is deposited on the substrate. In recent years, PLD has become the most popular technique for VO_2 thin-film fabrication because it shows a highly oriented crystalline

structure even without any post-annealing [38]. High quality thin-films VO_2 have been successfully deposited on both (0001) and (1010) sapphire substrates with PLD [41].

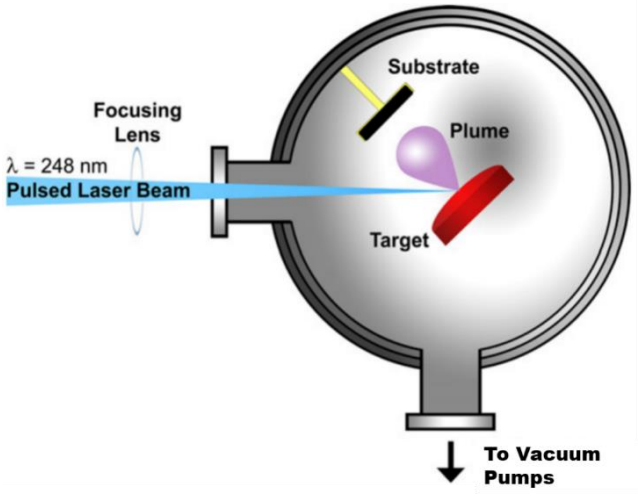

Figure 2-8. Typical experimental arrangement for PLD [53].

2.2 Properties and Fabrication Methods of GeTe

2.2.1 Properties of GeTe

The two stable phases of GeTe are a highly resistive amorphous phase and a highly conductive crystalline one. Switching between the two phases can be realized by different temperature pulses. A diagram of the heat profiles used to switch between amorphous and crystalline phases is shown in Figure 2-9. According to Khoo, sputtered GeTe is usually in an amorphous state [55]. A lower temperature (T_c about 190 ℃) and a longer timeframe are needed to transfer GeTe to a crystalline phase. Moreover, in order to reverse-transfer it back to the amorphous phase, a short and high temperature (T_m about 750 ℃) pulse needs to be applied, since a melt-quench process is required to take GeTe to the melting point and then rapidly cool it to create amorphous glass.

Figure 2-10 shows a five-order-of-resistance change in GeTe thin film, which is realized by using a micro-heater to apply a heat pulse [4]. It also shows that different pulse widths (heating times) can be applied to trigger the transition with different temperatures, making it more flexible for different applications.

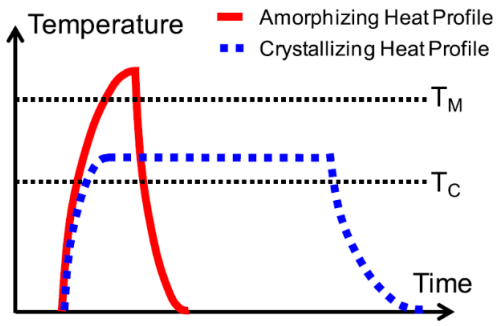

Figure 2-9. Diagram showing heat profiles used to switch between two phases [4].

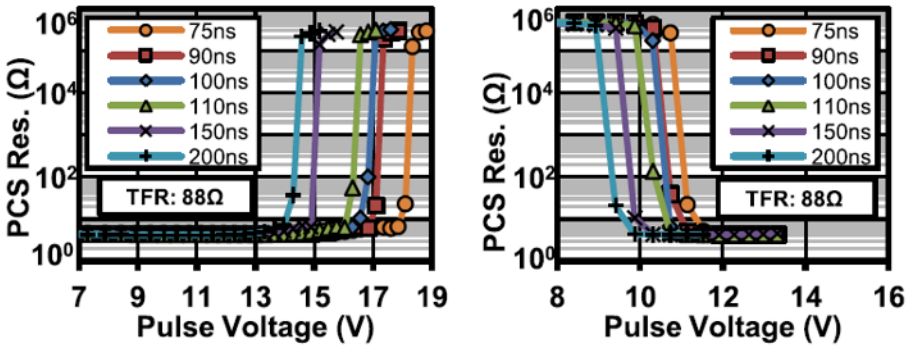

Figure 2-10. Measurement results of: a) pulse voltage to amorphized; b) pulse voltage to crystallize [4].

2.2.2 Deposition Methods of GeTe

Several processes have been applied to deposit GeTe thin film. Khoo et al. used RF-magnetron sputtering from stoichiometric targets and fabricated GeTe with different substrate temperatures. Amorphous GeTe is realized for all films with different temperatures [55]. Gwin also used RF magnetron sputtering and obtained GeTe film with five orders of resistance change [56]. Plasma-enhanced chemical vapor deposition of conformal GeTe was deposited by Gourvest et al. [57]. Pulsed laser deposition was used to fabricate GeTe-rich GeTe-Sb_2Te_3, and more than five orders of sheet resistance change were realized by Bouska et al. [58]. Meanwhile, Jung used a vapor-liquid-solid method to deposit GeTe nanowires [58].

2.3 Applications of VO_2 and GeTe

VO_2 is already being used for numerous applications, including smart thermochromic windows [60], microbolometers [61], spatial light modulators [62], optical switching [63] – [64], and electrical switching [49]. More applications can be seen in Figure 2-11 from Zheng Yang's summary [23]. In recent years, some studies about the potential application of VO_2 and GeTe in millimeter waves and RF microwave fields have been reported [5-17]. In the rest of this section, we will discuss some of the RF and microwave applications of VO_2/GeTe.

2.3.1 VO_2/GeTe-based RF Switches

Table 2-1 lists four papers for RF switches based on VO_2. All of them show good RF performance, especially [13], whose results show an ON-state insertion loss of <1 dB and an OFF-state isolation of >12 dB up to 220 GHz. This is promising for millimeter wave applications.

Table 2-2 lists four RF switches based on GeTe. As can be seen, the power consumption in [7] is only 82 mW in one switching cycle, which is very important for portable applications.

Table 2-1. VO_2-based RF switches

Reference	Order of Resistivity Change of VO_2	ON-state Insertion Loss	OFF-state Isolation	Switching Time
[9] Crunteanu et al.	3	3 dB @ 30 GHz	>21 up to 35 GHz	Several hundred nanoseconds
[11] Hillman et al.	4	<0.2 dB up to 50 GHz	>21.5 dB up to 50 GHz	N/A
[12] Pan et al.	5	<5 dB up to 20 GHz	>30 dB up to 20 GHz	N/A
[13] Hillman et al.	N/A	<1 dB up to 220 GHz	>12 dB up to 220 GHz	N/A

Table 2-2. GeTe-based RF switches

Reference	ON-state DC Resistance	Insertion Loss	Cut-off Frequency	Switching Time	Power Consumption
[6] Wang et al.	5 Ω	0.6 dB till 20 GHz	3.7 THz	600.5 µs per cycle	92 mW in one switching cycle
[7] Wang et al.	3.9 Ω	0.5 dB till 20 GHz	~4 THz	404 µs per cycle	82 mW in one switching cycle
[8] Shim et al.	N/A	0.63 dB @ 25 GHz	N/A	0.5-20 µs tuning speed	N/A
[9] El-Hinnawy	1.2 Ω	0.3 dB @ 20 GHz	7.3 THz	N/A	0.5 W to switch between states

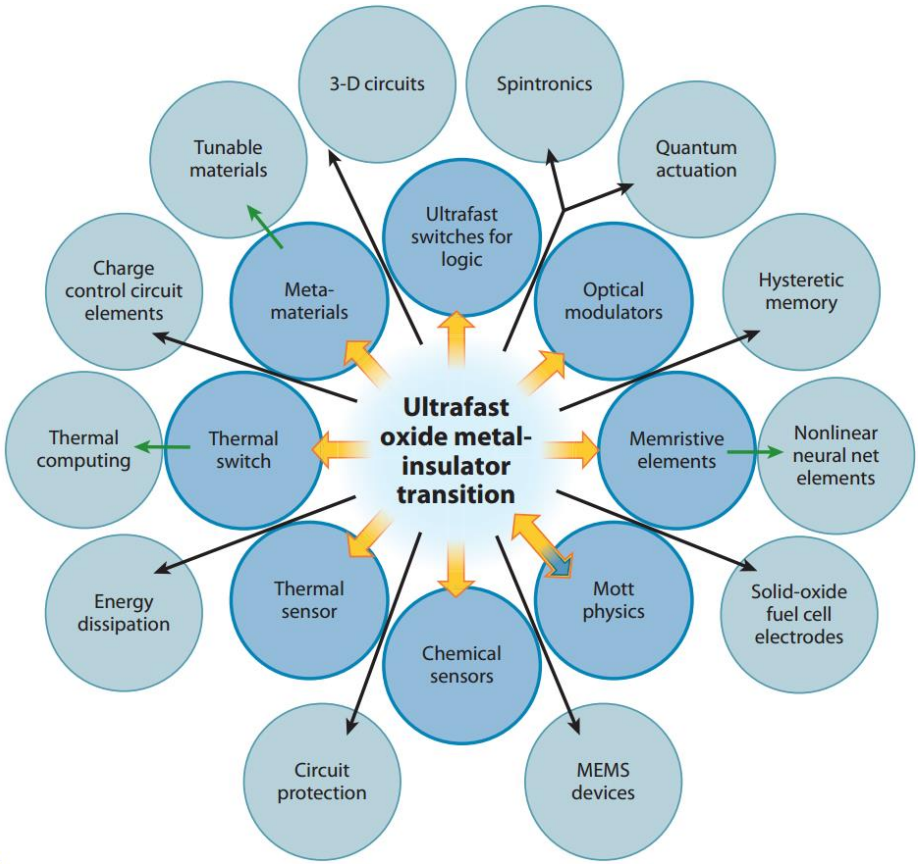

Figure 2-11. Potential applications of VO_2 [23].

2.3.2 VO_2 and GeTe-based RF Tunable Filters

Several attempts have been made to realize tunable or reconfigurable filters using VO_2 switches. Julien Givernaud and colleagues designed a "switchable stop band filter" with a switchable (ON or OFF) rejection band and a "discrete tunable stop-band filter" with a stop bandwidth and a tunable position based on VO_2 [14]. David Bouyge and colleagues designed two reconfigurable bandpass filters based on split-ring resonators and VO_2 switches [15][16]. The first designs they made are shown in Figure 2-12. As can be seen in the figure, the filter consists of two split-ring resonators and eight VO_2 switches on two sides of the resonators. The VO_2 switches are actuated by directly applying DC bias voltage on the VO_2 materials, which eliminates the use of micro-heaters to actuate the transition. The drawback is that high voltage is needed to obtain low resistance of the VO_2 switch due to the high resistance of the bias lines for DC supplies. The simulation and measurement results are shown in Figure 2-13 [15]. A tuning range close to 10% of the center frequency is realized, while the insertion loss is quite large due to the low-*Q* planar resonators themselves, along with the relatively high resistance of the VO_2 material. The second design is a tunable filter whose resonators can be switched ON and OFF to determine the tunable filter passband [16].

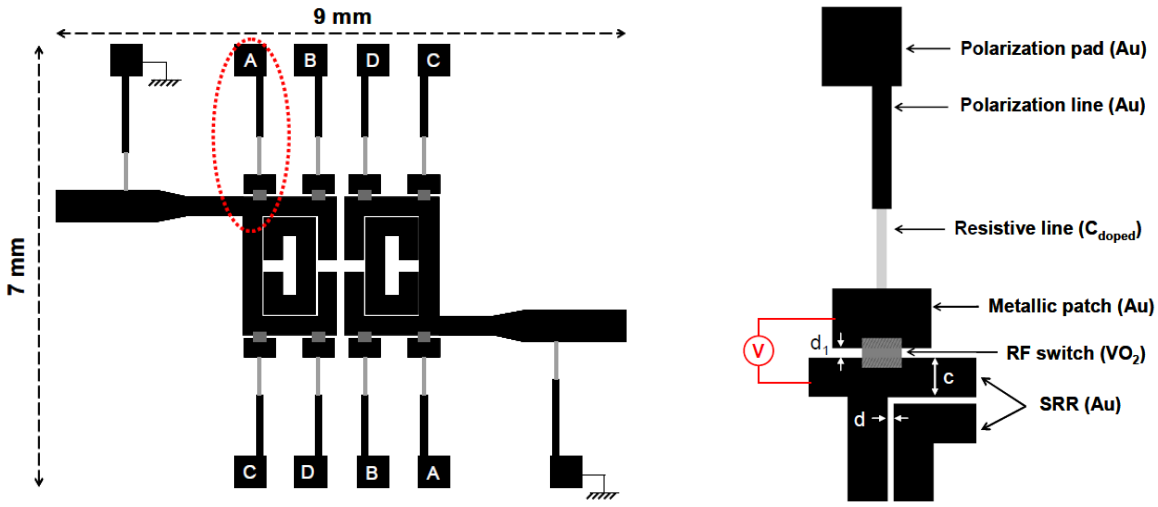

(a) (b)

Figure 2-12. (a) Layout of fabricated tunable bandpass filter; (b) overscale view of one tunable element [15].

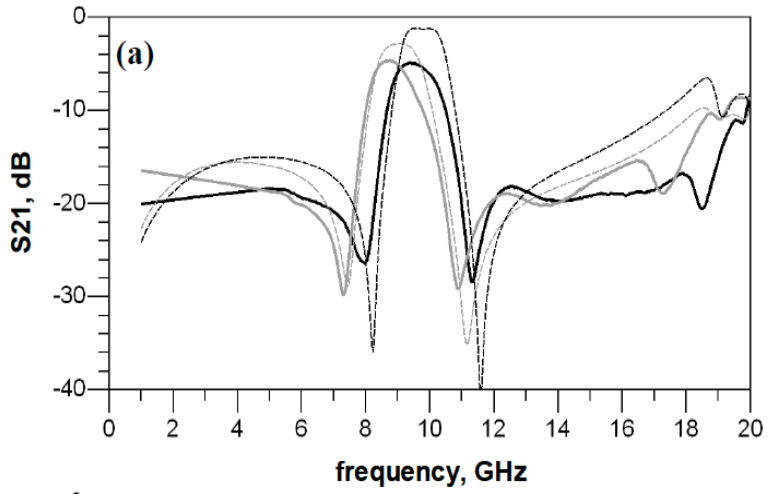

(a)

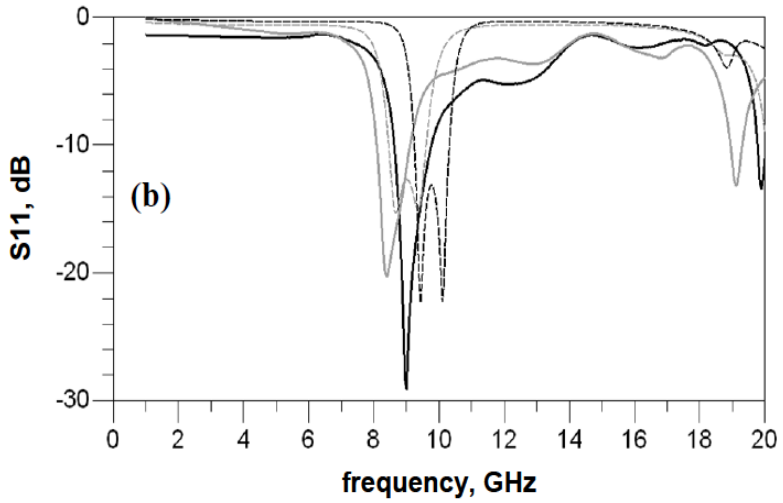

(b)

Figure 2-13. Simulated (dotted lines) and measured (solid lines) insertion (a) and return losses (b) of tunable filter [15].

A tunable bandstop filter (22.5-19.8 GHz) is realized using a VO_2-based tunable capacitor by Vitale and colleagues [17]. This design uses the metal and insulator states of VO_2 to control the gap of a horizontal metal-air-metal (MIM) capacitor. In so doing, it realizes a tunable capacitor

and uses the tunable capacitor to realize a tunable filter. A bandstop filter with a tunability of 12% in the center frequency from 22.5 GHz to 19.8 GHz is realized.

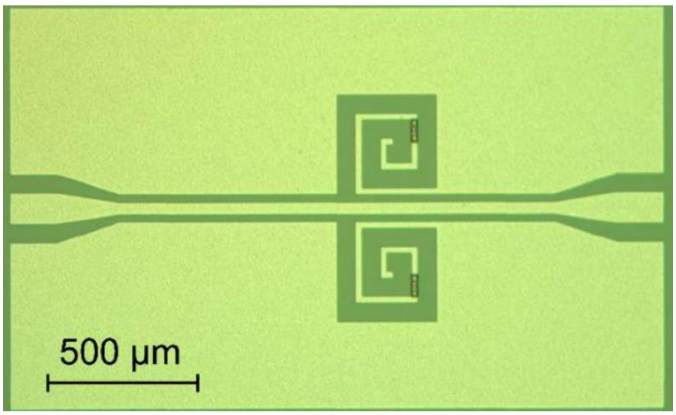

(a)

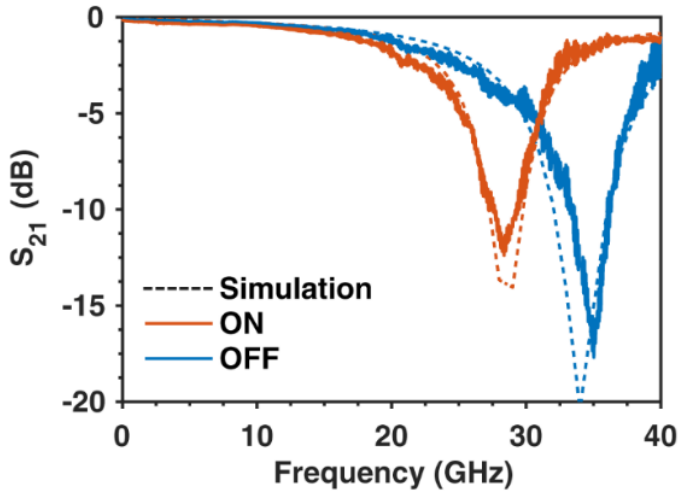

(b)

Figure 2-14. Tunable band stop filter: (a) optical image of the band stop filter; (b) measured S21 versus simulated S21 [17].

A Ku-band high-*Q* tunable resonator and tunable two-pole filter with VO_2 are realized [65]. The designed configuration and measurement results of the two-pole filter are shown in Figure 2-15. The tuning range is from 13.68 GHz to 14.7 GHz.

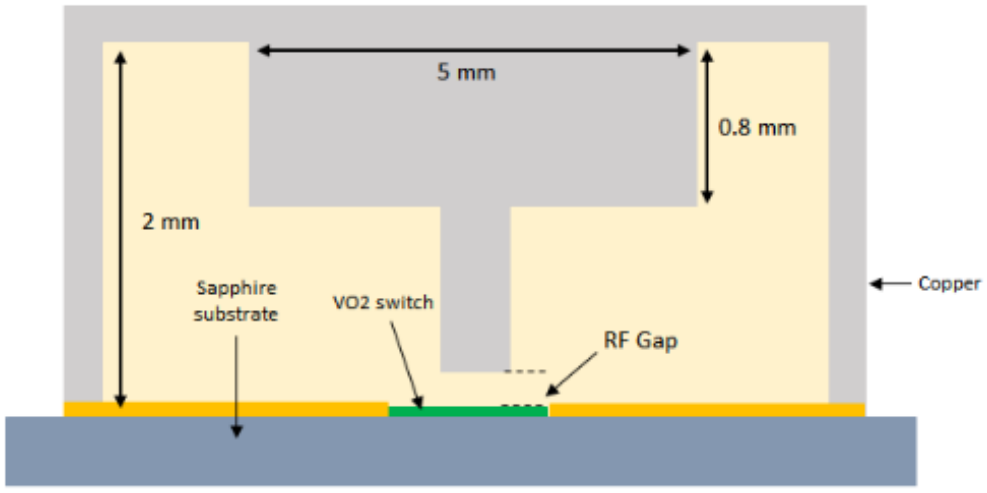

(a)

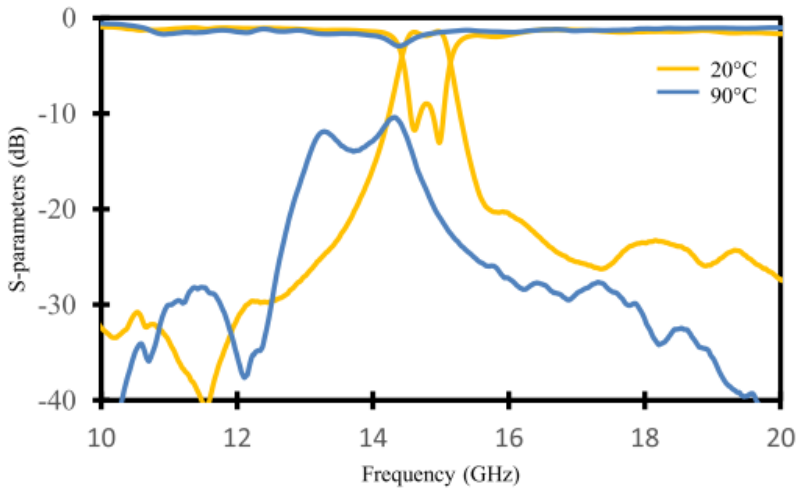

(b)

Figure 2-15. Tunable cavity filter with VO_2: (a) design configuration of a resonator; (b) measured results for a two pole filter [65].

GeTe-based tunable filters have also been investigated recently. An X-band reconfigurable bandpass filter was designed by Wang et al. [66], based on a GeTe RF switch and microstrip line resonators. Figure 2-16 shows the image of the reconfigurable tunable filter based on a GeTe switch and its measurement and simulation results. About 600 MHz of frequency tuning is realized with less than 3.2 dB insertion loss. An unloaded quality factor (Q_u) of 59-73 is realized

by this work, which is good compared to its peers. However, since it is a microstrip resonator-based filter, the Q_u is limited by the resonator itself and cannot be high-Q. Kodama and Coutu Jr. reported THz tunable split-ring resonators based on GeTe. The resonance frequency can be tuned from 0.8 THz to 2.2 THz.

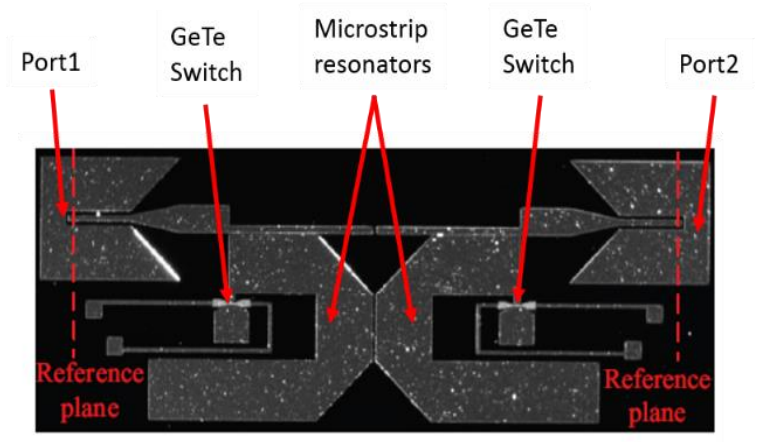

(a)

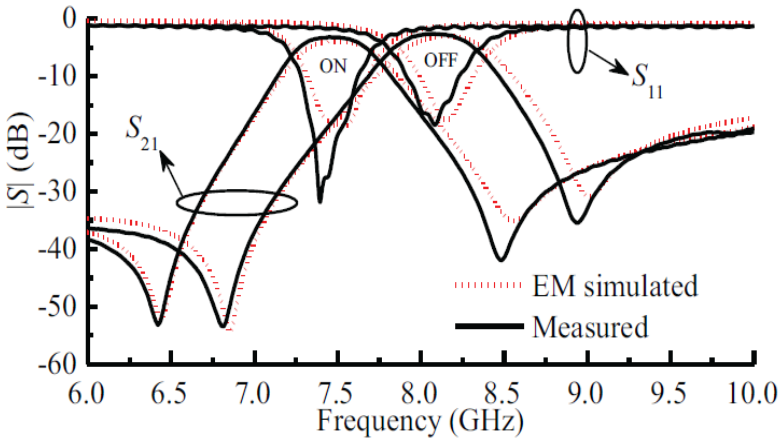

(b)

Figure 2-16. (a) Image of bandpass filter; (b) measurement and simulation results [66].

A tunable bandpass filter with GeTe was presented by Ghalem et al. in [67]. The device is a microstrip line filter integrated with GeTe at the end of the lines which uses short laser pulses to change the GeTe properties.

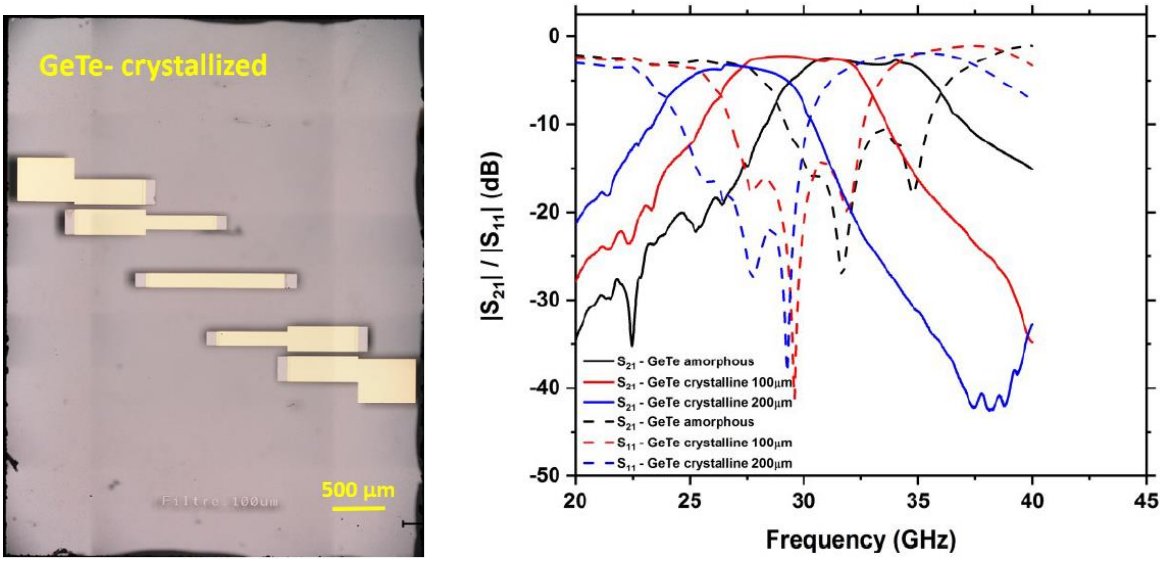

(a) (b)

Figure 2-17. Tunable microstrip line bandpass filter with GeTe: (a) image of fabricated filter; (b) measured results [67].

2.3.3 Other Reconfigurable Applications

Yanhan Zhu and colleagues designed a tunable dual-band terahertz bandpass filter based on VO_2, which realized ~32% of resonance frequency at around 0.5 THz [18]. A tunable MEMS resonator is realized by a VO_2-coated silicon dioxide bridges with a 20% change in resonant frequency [19]. Meanwhile, James and colleagues reported some tunable plasmonic antennas based on VO_2 [20].

2.3.4 Comparing MEMS and MIT/PCM Switches

RF MEMS switches have been of increasing interest to researchers over the past few decades due to their advantages of low loss, low power consumption, high isolation and high linearity [68]. However, the reliability and costs of RF MEMS switches continue to hinder the widespread use of the technology. In contrast, MIT/PCM-based RF switches show comparable performance to RF MEMS switches with promising ability to realize better reliability.

The cut-off frequency of an RF switch is given by $f_T = 1/ (2Ron•Coff)$, which is an important indicator of an RF switch's insertion loss and isolation performance. Figure 2-18 shows some RF switches fabricated using various techniques. Among these, MEMS-based switches exhibit the highest cut-off frequencies in the range of 10 THz to 70 THz, and VO_2-based RF switches have cut-off frequencies comparable to MEMS switches. A VO_2-based RF switch with a cut-off frequency of 40 THz and an ON-state resistance of 1 Ω was realized by Hillman et al. [11], while Madan et al. obtained a cut-off frequency of 26.5 THz for an RF switch based on VO_2 [69]. GeTe-based RF switches have relatively lower cut-off frequencies but offer low DC power consumption due to their latching capabilities. Cut-off frequencies of 3.7 THz, 4 THz, and 7.3 THz were obtained for GeTe switches in [6], [7] and [9], respectively, as listed in Table 2-2. A comparison of other operating performances among MEMS switches, VO_2 switches, and GeTe switches is given in Table 2-3.

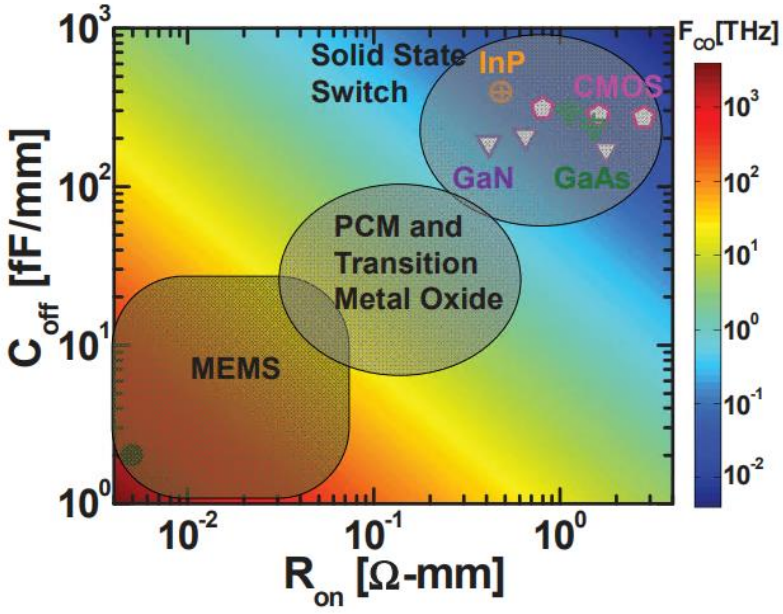

Figure 2-18. ON-state resistance and cut-off frequencies for RF switches using different techniques [69].

Table 2-3 Operating parameter comparison among MEMS, VO_2 and GeTe [69].

Parameters	MEMS	VO_2	GeTe
Insertion Loss	Low	Low	Low
Return Loss	Good	Good	Good
Reliability	Fair	Good	Fair
Switching Speed	in ms	in μs	in ns
Power Handling	High	Relatively low	Relatively High [70]
Steady-state Power Consumption	Series switch (1mW scale) Parallel switch (0mW)	DC voltage switch (<1mW [10]) Thermal actuate (10mW to 100mW scale [13])	0 mW

2.4 High-*Q* Tunable Filters

High-*Q* tunable filters are mainly realized with 3-D structure resonator configurations, since planner structures are usually relatively lossy in room temperature. Different tuning methods have been used in the past for realizing high-*Q* tunable filters, such as motor tuning, MEMS tuning, piezoelectric tuning and magnetic tuning.

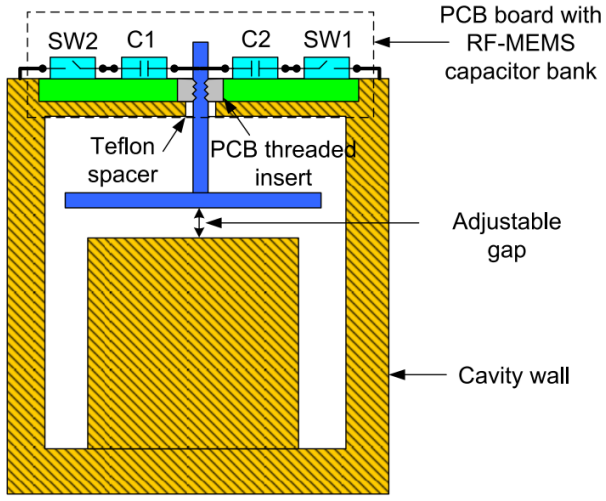

(a)

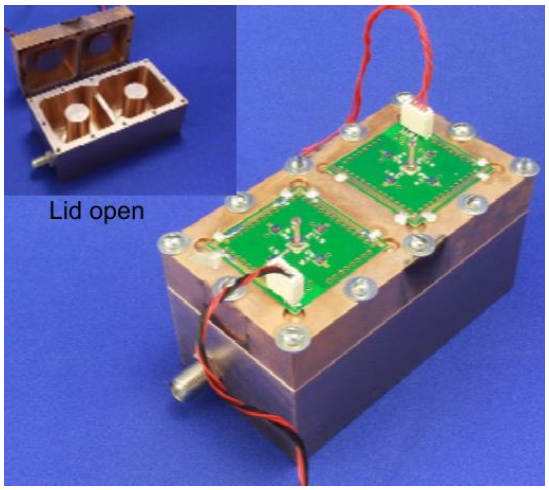

(b)

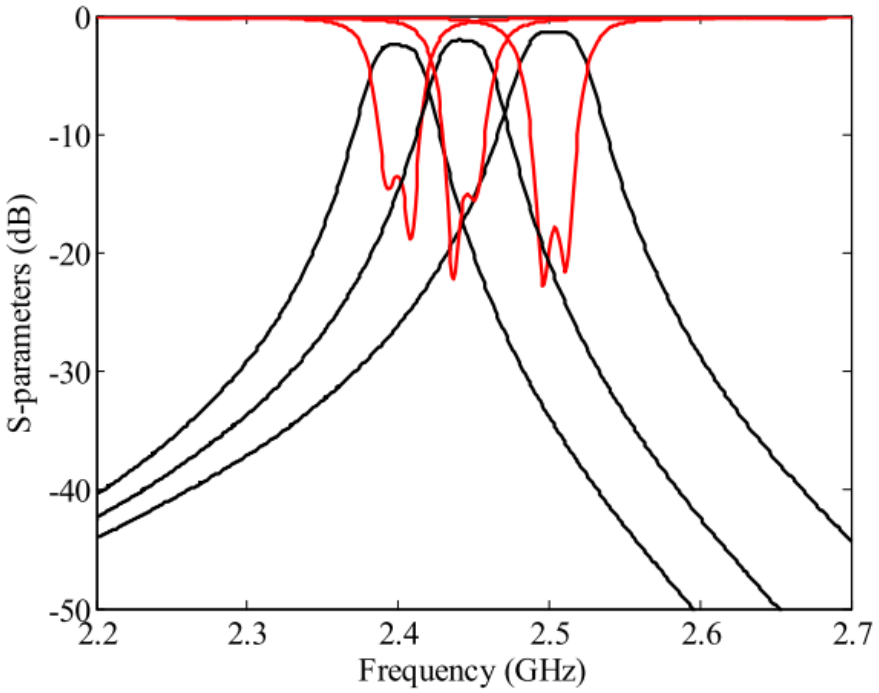

(c)

Figure 2-19. Tunable combline filter: (a) configuration of resonator; (b) picture of two-pole tunable filter; (c) measured results for two-pole tunable filter [71].

In [71], a combline tunable bandpass filter with center frequency of 2.5 GHz and bandwidth of 22 MHz is presented by S. Fouladi et al. As is shown in Figure 2-19, RF MEMS switches are used in conjunction with a lumped element capacitor to form a capacitor bank for tuning the combline filter. A quality factor ranging from 1300 to 374 over a tuning range of 110 MHz is realized [71].

In [72], an evanescent-mode tunable cavity filter is presented. The filter is manufactured using silicon-micromachining techniques with a microcorrugated diaphragm (MCD) tuner, as shown in Figure 2-20 and Figure 2-21. In the study, a tuning range from 20 GHz to 40 GHz with insertion loss between 3.1 and 1.1 dB is realized, exhibiting unloaded *Q* from 264 to 540.

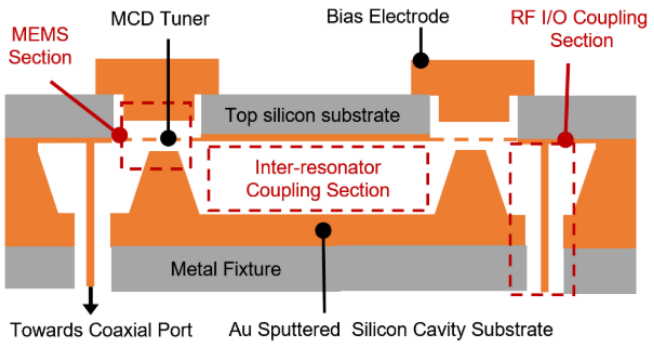

(a)

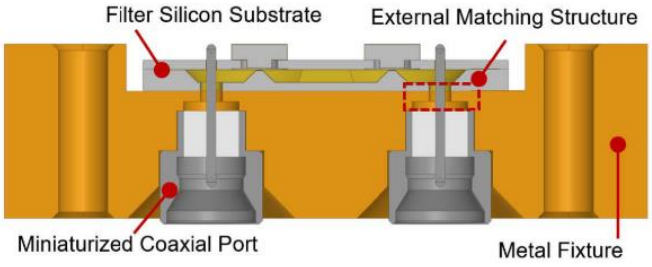

(b)

Figure 2-20. (a) Conceptual drawing of all-silicon evanescent-mode cavity filter with tunable center frequency; (b) cross-sectional view of packaged device [72].

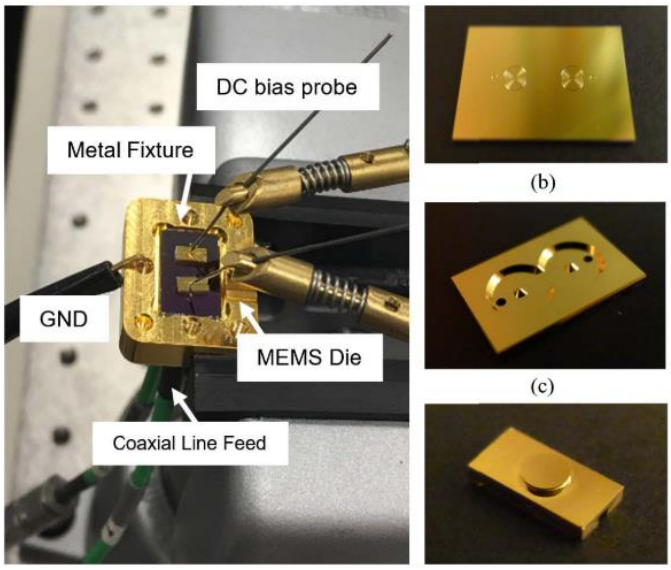

(a) (d)

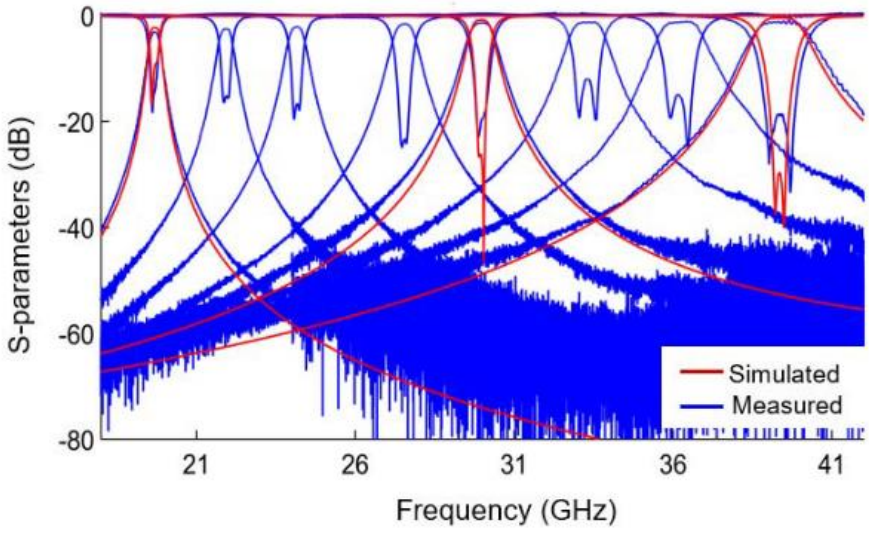

(e)

Figure 2-21. (a) RF characterization set-up of two-resonator all-silicon BPF; (b) front view of manufactured die of diaphragm; (c) front view of manufactured die of cavity; (d) side view of manufactured die of DC biasing electrode; (e) measured results [72].

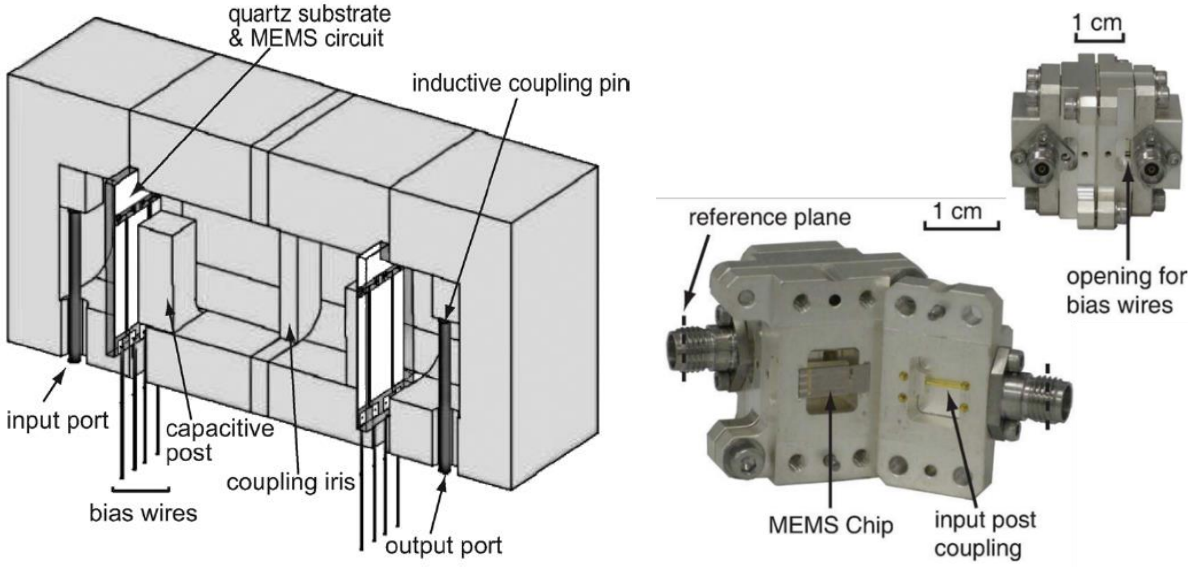

(a) (b)

Figure 2-22. (a) Half side of tunable two-pole evanescent-mode cavity filter; (b) fabricated picture of tunable evanescent-mode cavity filter with RF-MEMS cantilever-switch capacitance network chip [73].

In [73], a high-*Q* miniaturized tunable cavity filter is realized using planar capacitive RF MEMS switch networks. Figure 2-22 shows the configuration and fabricated image of the tunable filter, MEMS circuits are fabricated on quartz substrate and then mounted inside the metal cavity. Figure 2-23 illustrates the measurement results of the tunable filter. This work realized a frequency coverage of 4.07-5.58 GHz, with an unloaded *Q* of 300-500.

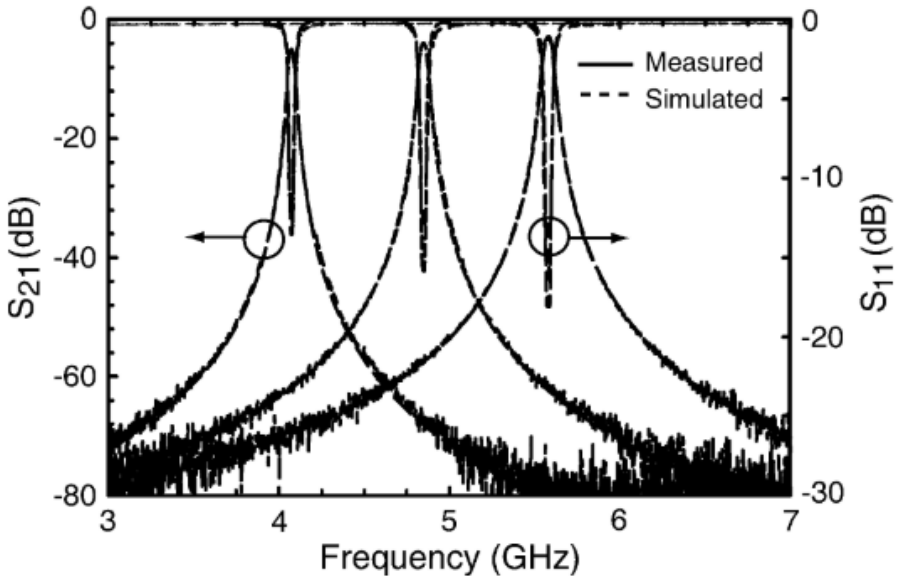

Figure 2-23. Measured and fitted S-parameters for three filter responses [73].

Chapter 3
MIT/PCM-based RF Switches and Reconfigurable RF Passive Devices

3.1 VO_2-based Series and Parallel RF Switches

3.1.1 Introduction

Over the past few decades, metal-insulator transition material has been widely used in optical and other engineering applications. The phenomenon of phase transitions in binary transition-metal oxides was first reported in [75] by Morin, who concluded that transition-metal oxides such as VO_2, V_2O_3, VO and Ti_2O_3 would exhibit increases in resistivity by several orders of magnitude when their temperature dropped below their transmission temperature [22]. VO_2 is one of the best-known metal-insulator transition materials due to its near-room-temperature transition temperature of approximately 68 ℃. The resistivity of VO_2 drops dramatically when it

is heated past its transition temperature, which has been found to be consistently repeatable in [76].

In recent years, VO_2 has gained increasing attention in RF and microwave applications, as it offers an appealing avenue for constructing high performance RF microwave switches and tunable devices [17][69][76][77]. VO_2-based switches with small insertion loss were realized in millimeter-wave frequency in [76], however, these series switches have very high dimensional constraints and require a complex and costly fabrication process, which prevents them from being widely accepted in field applications. Although the work presented in [69][77] proposed simpler fabrication processes for fabricating VO_2-based RF switches, the RF performance of the switches still has a large room for improvement.

This chapter proposes two heater-integrated VO_2-based RF switches fabricated with a simple four-mask copper-base process on an alumina substrate. The combined use of a copper conductive layer and the low-loss alumina substrate paves the way for low-cost, high-performance VO_2 RF switches.

3.1.2 VO_2 Deposition and Characterization

Figure 3-1 shows the RF sputtering system used for the VO_2 deposition in the Quantum Nano Centre (QNC) of University of Waterloo. The parameters for depositing the thin-film VO_2 with the reactive RF sputtering system are summarized in Table 3-1. The vanadium target used in the deposition has a diameter of 2 inches and a thickness of 0.25 inches.

Figure 3-2 depicts the XRD pattern for two thin-film VO_x with different O_2 ratios during reactive RF sputtering. When the O_2 ratio is 10%, the XRD pattern matches the VO_2 model well, but when the O_2 ratio is 12.5%, it matches the V_2O_5 model instead. The AFM scanning results are shown in Figure 3-3. As can be seen, the highest VO_2 hill in Fig. 3-3 (a) is 140 nm, while the highest V_2O_5 hill in Fig. 3-3 (b) is 206 nm. Furthermore, the VO_2 film is much smoother than the V_2O_5 film. Both tests were used to determine proper sputtering conditions and optimize film quality.

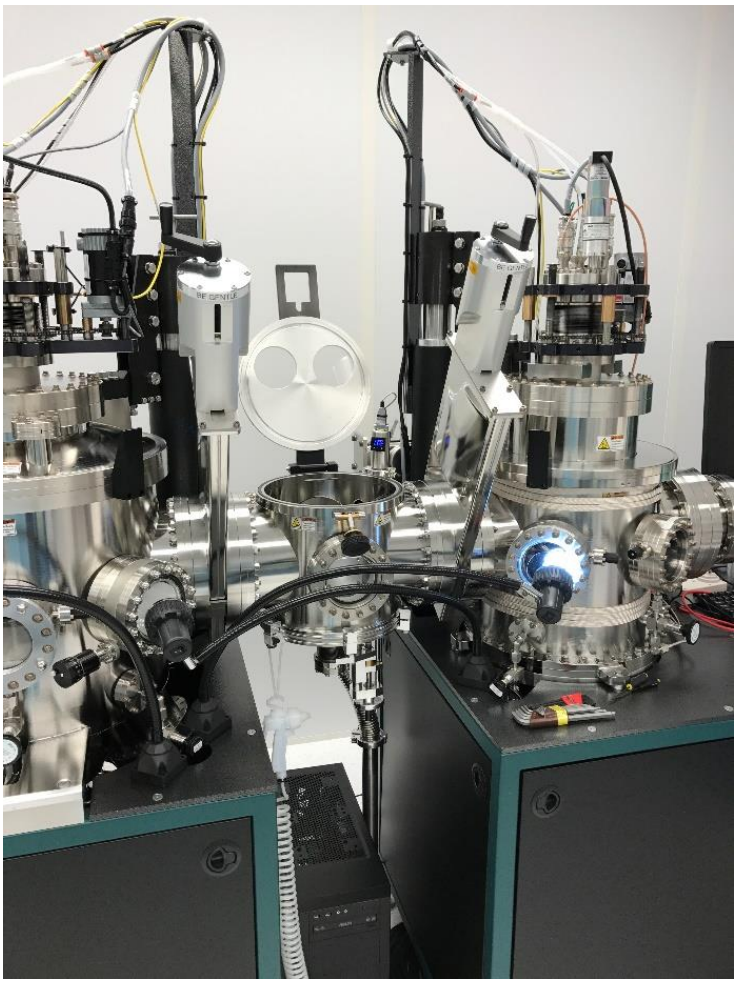

Figure 3-1. QNC lab AJA sputtering system for RF reactive sputter.

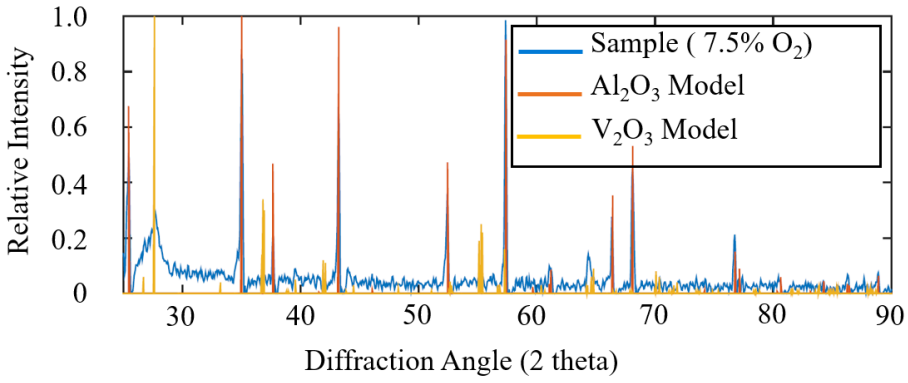

(a)

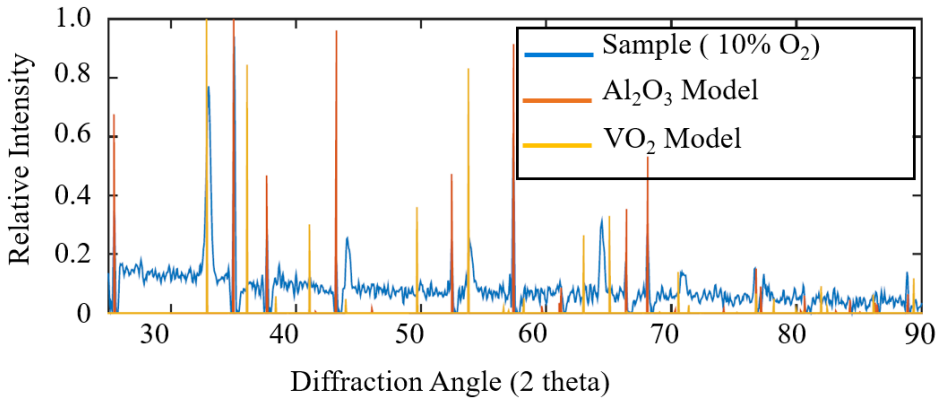

(b)

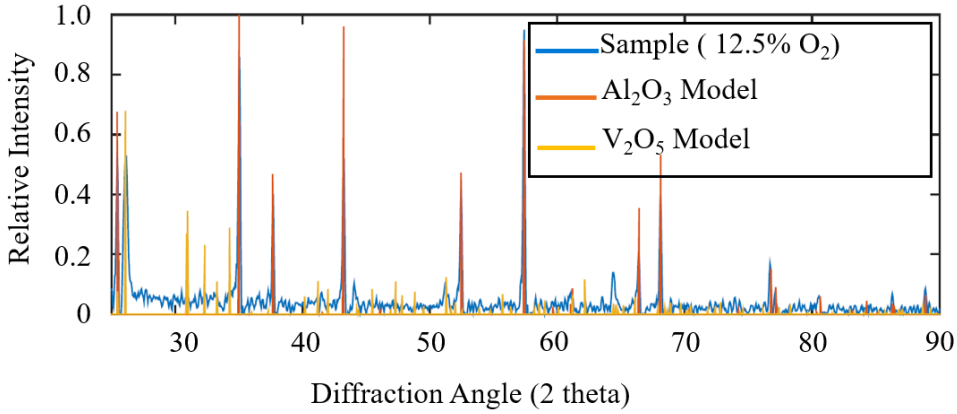

(c)

Figure 3-2. X-ray diffraction (XRD) pattern for thin-film VO_x: (a) thin-film V_2O_3; (b) thin-film VO_2; (c) thin-film V_2O_5 [74].

Table 3-1. VO_2 deposition parameters

Parameter	Value
RF power	200 Watts
Chamber base pressure	2 µTorr
Deposition pressure	3 mTorr
Substrate temperature	500 ºC
O_2 ratio	10.00%

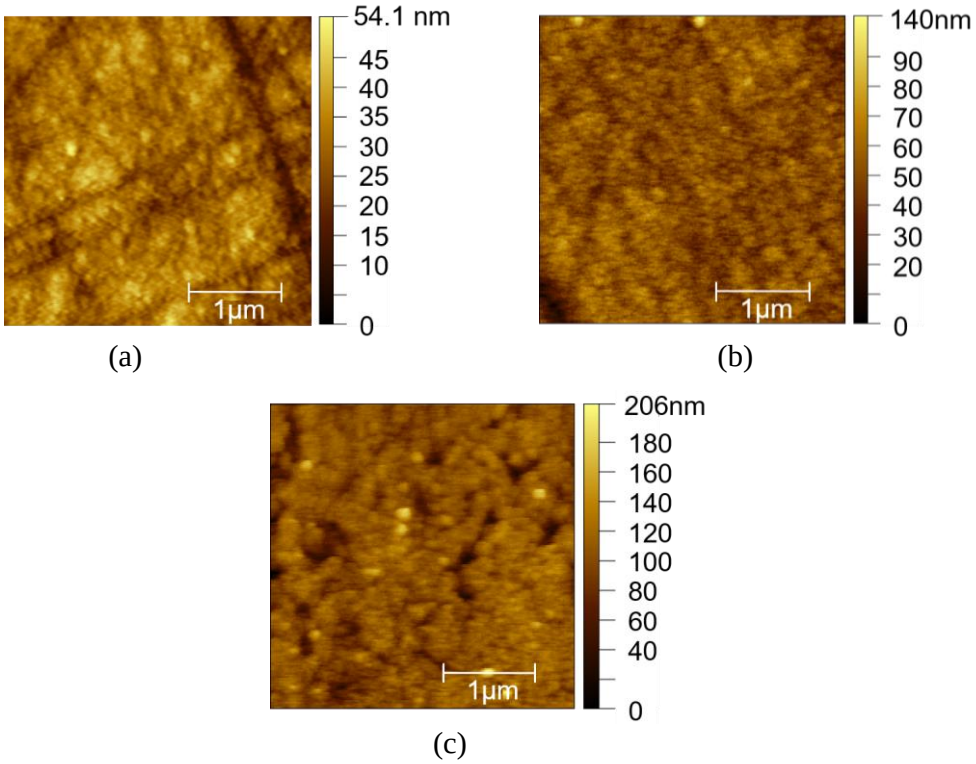

Figure 3-3. AFM scanning pictures: (a) thin-film V_2O_3; (b) thin-film VO_2; (c) thin-film V_2O_5.

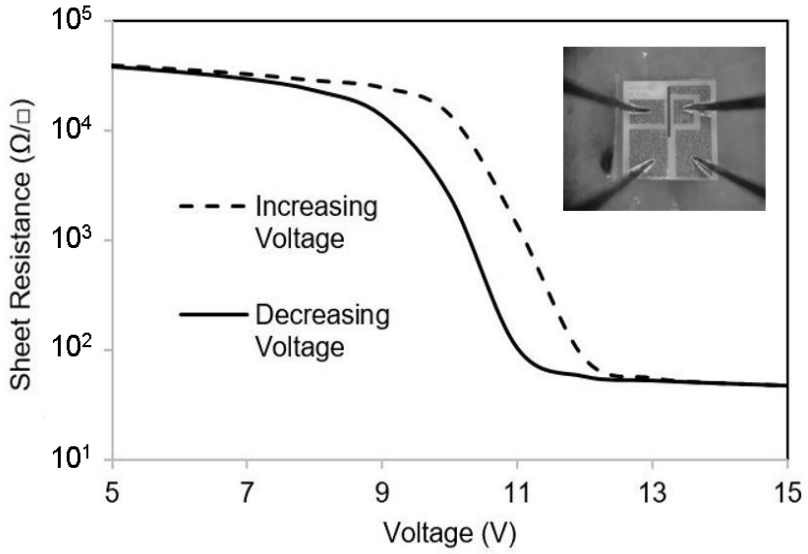

Figure 3-4. Sheet resistance of VO_2 thin-film versus voltage applied to micro-heater.

Figure 3-4 shows the hysteresis curve of the sheet resistance of the sputtered VO_2 film versus the voltage applied to the micro-heater. The sheet resistance ranges from 48 Ω/□ to 47 kΩ/□. The

measurement set-up is shown at the top right corner of Figure 3-4, in which one pair of DC probes is used to apply voltages for heater control, while the other pair is used to measure the VO_2 resistance.

3.1.3 Design and Fabrication

The basic geometries of the series and the parallel VO_2-based RF switches are presented in Figure 3-5. The 3D exploded illustration of the two designs is presented in Figure 3-6, showing all layers and their materials. The CPW line of both the series switch and the parallel switch is designed with a signal line width of 24 µm, a gap of 10 µm, and a length of 600 µm.

The micro-heater designed in the series switch has a width of 15 µm and a length of 200 µm, whereas the micro-heater in the parallel switch consists of two separate U-shape heater coils. The heater line for the parallel switch is carefully routed to avoid overlap with the signal CPW line, thereby helping to reduce the parasitic capacitance and improving the insertion loss performance for the switch. Figure 3-7 shows the copper-based VO_2 fabrication process used for realizing the two switch designs. As can be seen, a 500-nm SiO_2 layer is first deposited on an alumina (Al_2O_3) substrate as a thermal isolation layer with a plasma-enhanced chemical vapor deposition (PECVD) system. Then, a 60-nm chromium (Cr) layer is deposited with e-beam evaporation, followed by patterning for micro-heaters and bias pads.

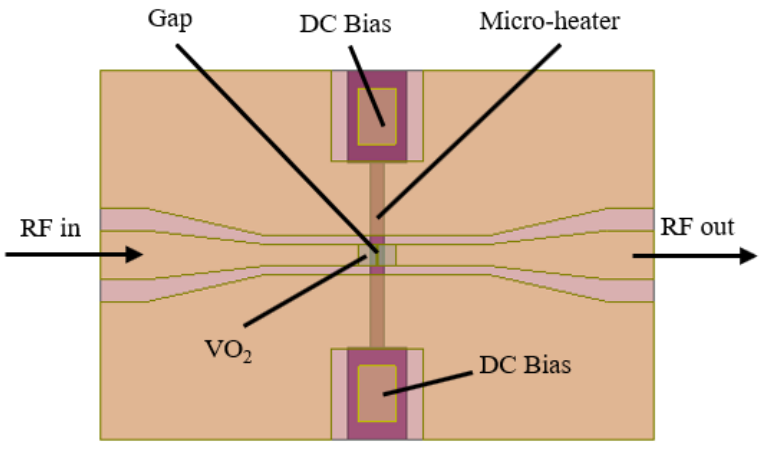

(a)

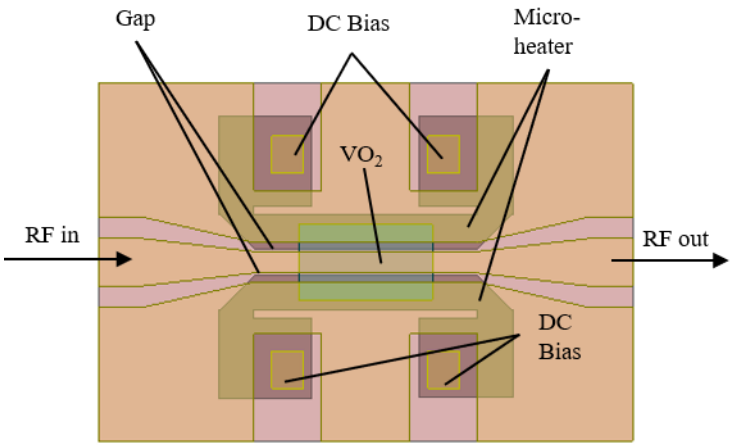

(b)

Figure 3-5. Design structure of VO_2-based switches: (a) series switch; (b) parallel switch.

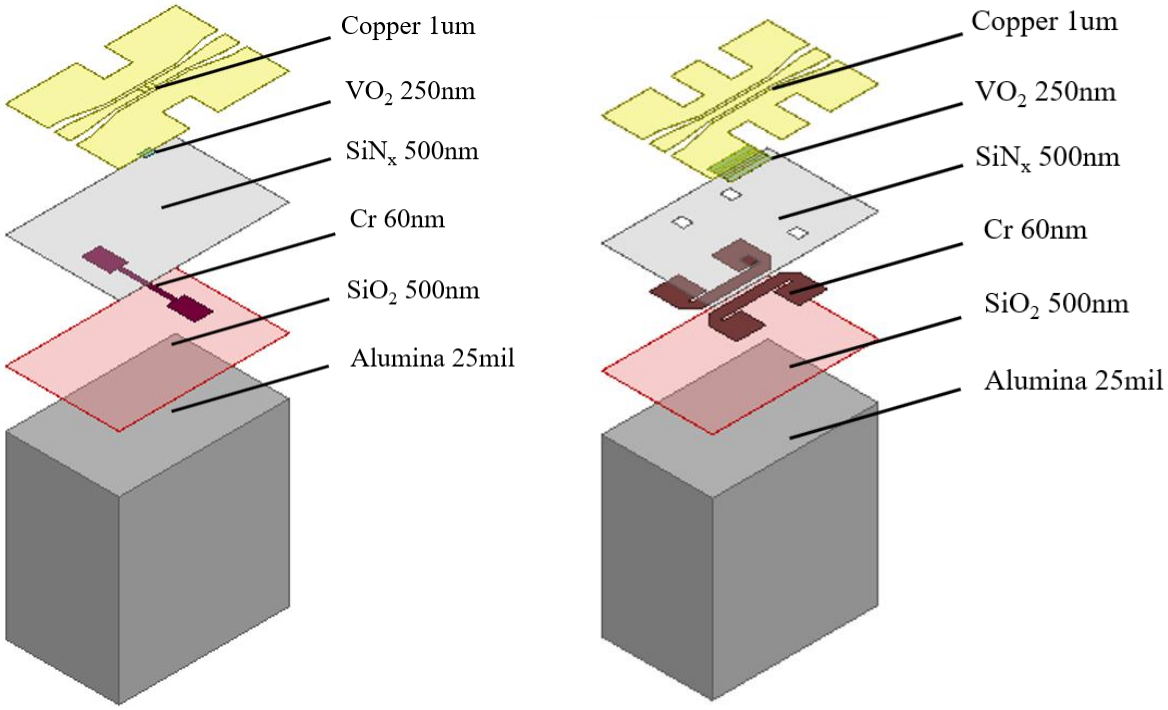

(a) (b)

Figure 3-6. 3D view of each layer of the designed VO_2-based switches: (a) series switch; (b) parallel switch.

The sheet resistance of the 60-nm Cr thin-film is measured to be 50 Ω/□. Next, a 500-nm SiN_x layer is deposited with PECVD as the barrier layer between the patterned Cr layer and the

upcoming VO_2 layer. A 250-nm VO_2 is then deposited with RF-reactive sputtering and patterned along with the underlying SiN_x layer to allow the required conductive contacts between the Cr resistive lines and the upcoming copper layer. Finally, a 1-μm copper layer is deposited with e-beam evaporation, patterned for the transmission line portions of the RF switches.

The parameters for depositing the thin-film VO_2 with the reactive RF sputtering system are summarized in Table 3-1. The Vanadium target used in the deposition has a diameter of 2 inches and a thickness of 0.25 inches. Photographs of the two fabricated switches are shown in Figure 3-8.

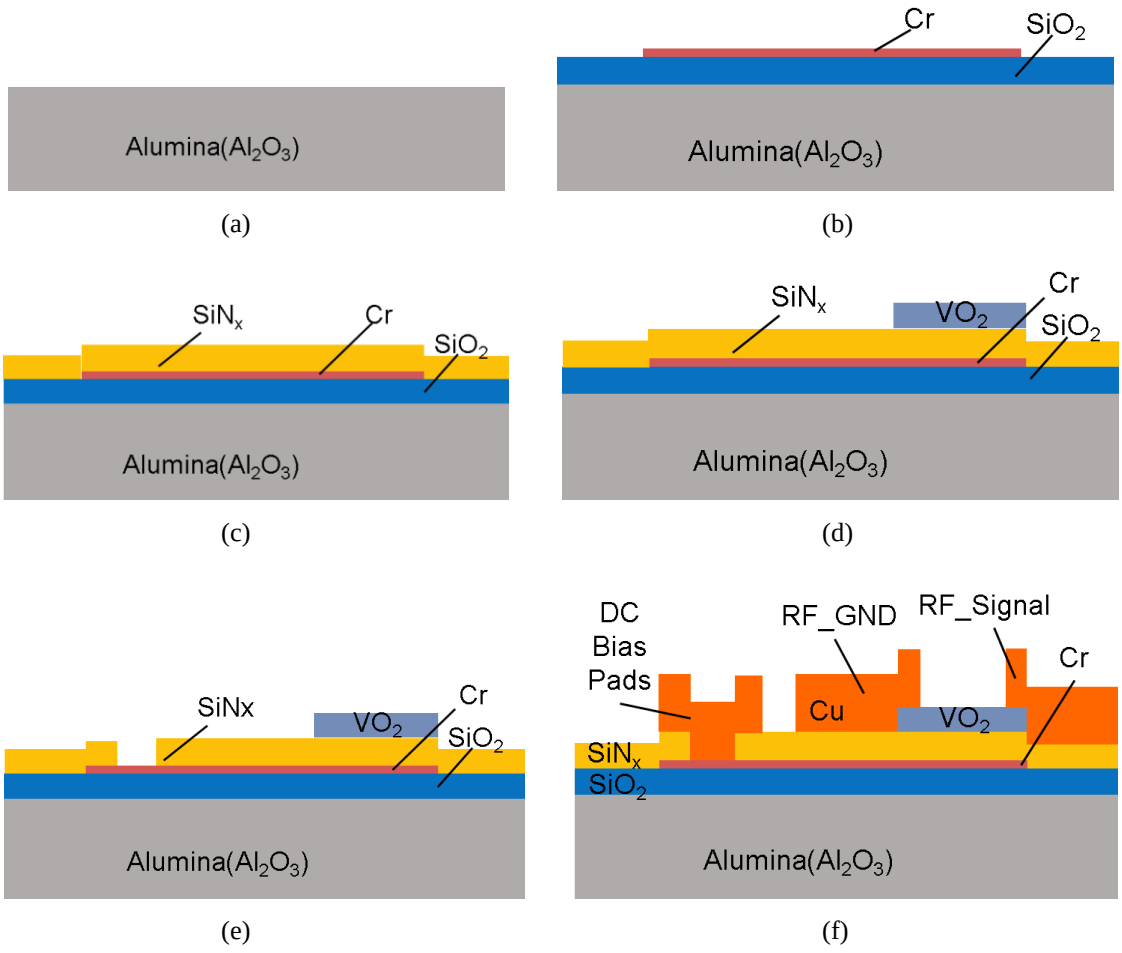

Figure 3-7. Copper-based insulator-on-alumina VO_2 fabrication process.

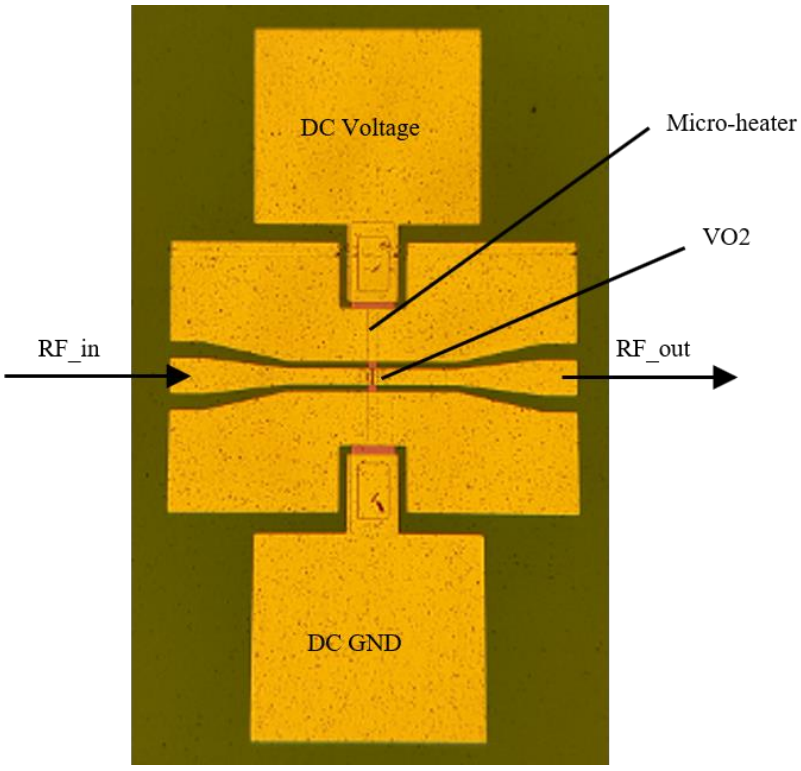

(a)

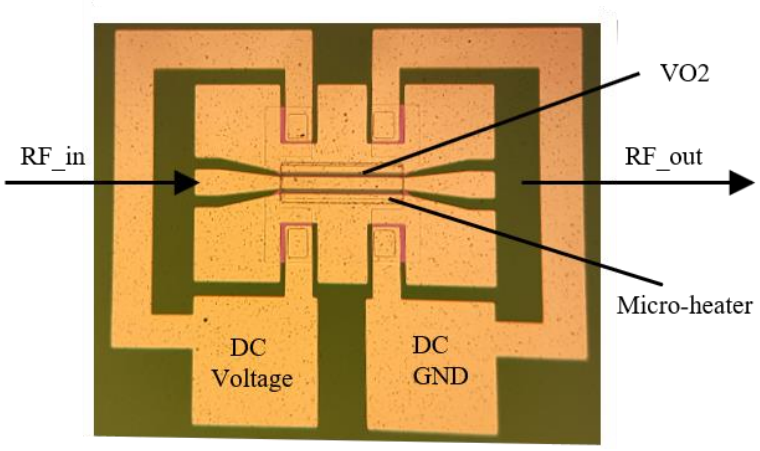

(b)

Figure 3-8. Fabricated VO_2-based switches: (a) series switch; (b) parallel switch.

3.1.4 Simulation and Measurement Results

The HFSS EM simulation results for the series switch and parallel switches are shown in Figure 3-9. Both simulations used VO_2 sheet resistance of 47 kΩ/□ for the high resistivity state, and 48 Ω/□ for the low resistivity state. The simulation results for the series switch show an insertion loss <1 dB from DC to 75 GHz when the switch is in the ON state, and an isolation of 30 dB from DC to 75 GHz when it is in the OFF state. For the parallel switch, the insertion loss from DC to 75 GHz is less than 1.4 dB in the ON state, while the isolation is larger than 25 dB in the OFF state.

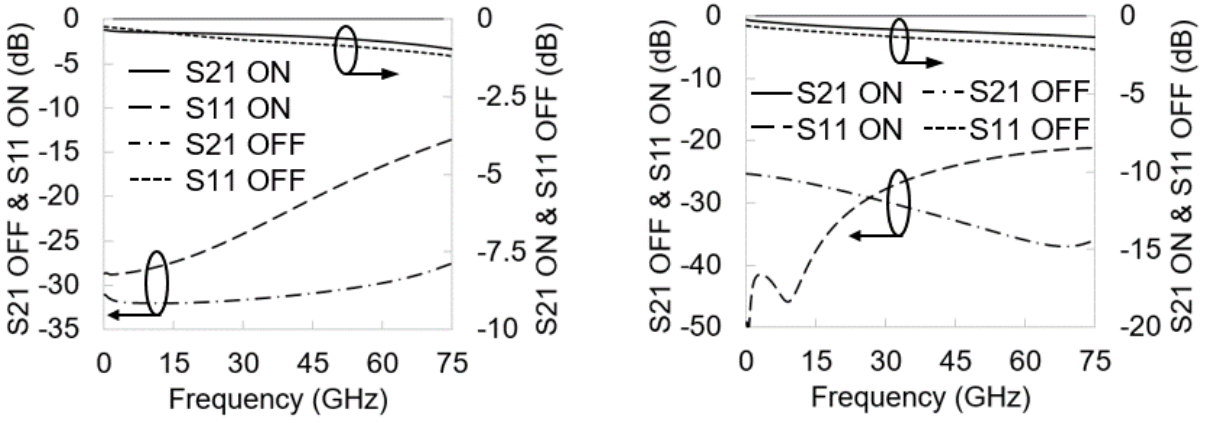

(a) (b)

Figure 3-9. EM simulation results: (a) series switch; (b) parallel switch.

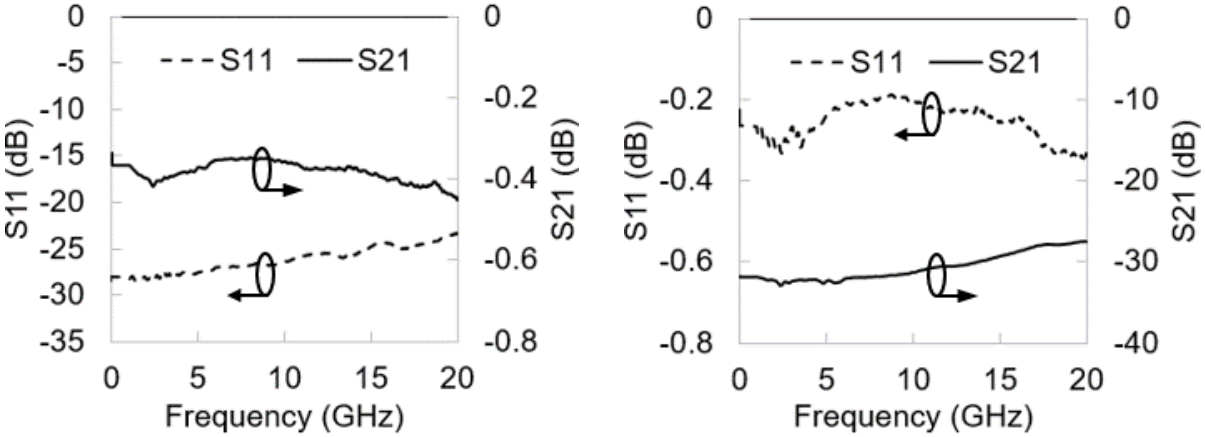

(a) (b)

Figure 3-10. Measurement results of series switch: (a) switch ON, (b) switch OFF.

Figure 3-10 shows the measurement results of the series switch from DC to 20 GHz. The insertion loss of the series switch is less than 0.46 dB in the ON state, and the isolation is from 28 dB to 32 dB in the OFF state. Figure 3-11 shows the measurement results of the parallel switch. An insertion loss of less than 0.4 dB was achieved from DC to 20 GHz, along with an isolation ranging from 25 to 28 dB from DC to 20 GHz. Based on these measurement results, the parallel switch demonstrates slightly better insertion loss, especially at low frequency, while the series switch demonstrates better isolation.

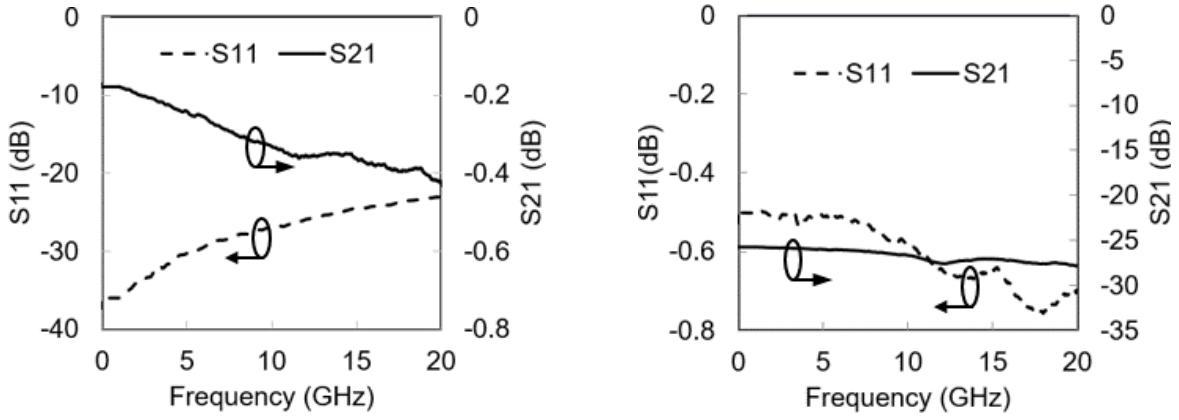

Figure 3-11. Measurement results of parallel switch: (a) switch ON; (b) switch OFF.

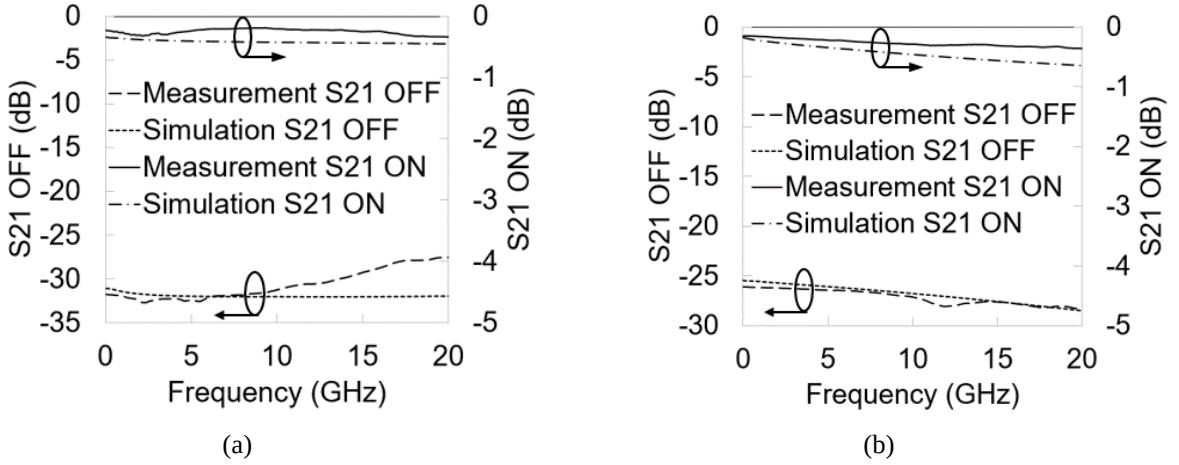

Figure 3-12. Measurement and simulation comparison for ON-state insertion loss (S21 ON) and OFF-state isolation (S21 OFF): (a) series switch; (b) parallel switch.

A comparison between measurement and simulation results is given in Figure 3-12. As shown in the figure, the measurement and simulation results match quite well for both series and parallel switches with ON-state insertion loss (S21 ON) and OFF-state isolation (S21 OFF).

3.1.5 Summary

In this section, two VO_2-based RF switches were fabricated with a simple copper-based fabrication process on an alumina substrate. The simulation results show the potential for these switches to operate up to 75 GHz. The RF measurement results from DC to 20 GHz match the simulation, demonstrating excellent RF performance. The proposed fabrication process allows monolithic integration of VO_2-based switches with a wide range of RF circuits.

3.2 VO_2-based Variable Attenuator

3.2.1 Introduction

A variable attenuator is a crucial device that can control signal level adaptively. It can also be employed to help in matching source and load impedances for active devices in order to achieve maximum power transfer or better matching. It is especially useful in various wireless communication applications such as radar systems and control gain for specific receiver input [79]. In addition to FET-based attenuators [80], PIN diodes are commonly employed in the design of variable attenuators [81]. However, the performance of semiconductor-based attenuators degrades considerably when operating at millimeter-wave frequencies. More recently, graphene was proposed in [82]-[83] to realize variable attenuators, but the measured insertion loss was relatively high.

For the first time, a thin-film VO_2 is employed here to realize a millimeter-wave variable attenuator. The thin-film VO_2 is monolithically integrated with a 0-dB coupler and bias heater circuit on a single chip. Although our focus is to demonstrate the feasibility of realizing a 30-GHz attenuator, VO_2 films are capable of operating at much higher frequencies, as shown in [13] and [18], [84]. The attenuator concept presented in this study can be employed to realize a small-

size variable attenuator with low insertion loss and broad attenuation range for a wide range of microwave and millimeter-wave applications.

3.2.2 Design and Fabrication

The schematic of the variable attenuator is shown in Figure 3-13. It consists of a 0-dB branch-line coupler integrated with three tunable resistors. Figure 3-14 shows a 3D structure of the variable attenuator. The 0-dB coupler, the VO_2 films, and the heater are all integrated monolithically on an alumina substrate. Conventional attenuators that use diodes as variable resistors require DC blocks and bias circuits for operation. In [81], the attenuator was designed to operate at 2 GHz. At millimeter-wave frequencies, the size of the bias circuit of the diode is comparable or even larger than the coupler itself. A thin-film VO_2 offers better linearity performance than do diodes and can serve as a tunable resistor at millimeter-wave frequencies.

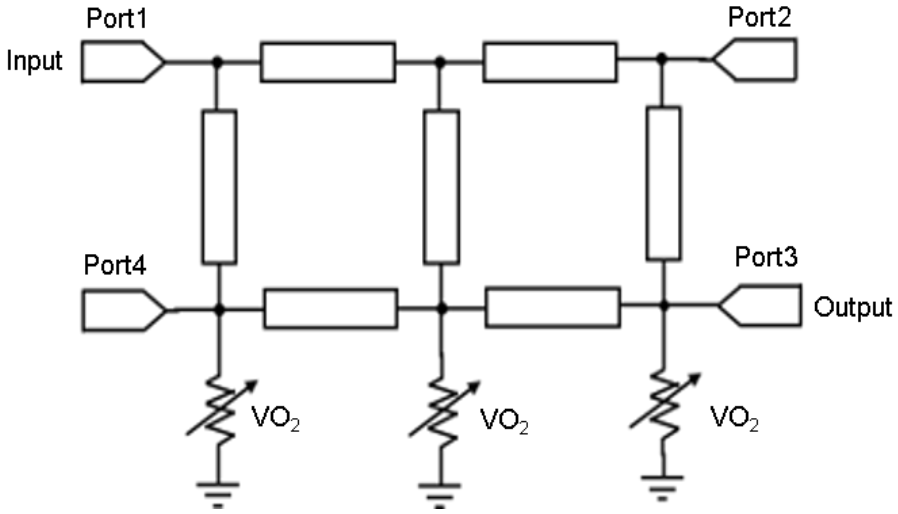

Figure 3-13. Schematic of variable attenuator.

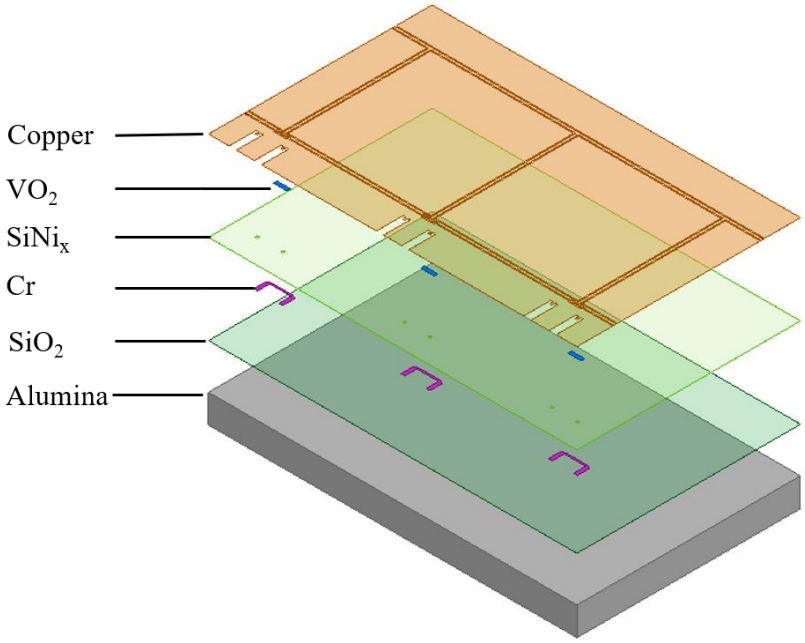

Figure 3-14. 3D view of each layer of variable attenuator structure.

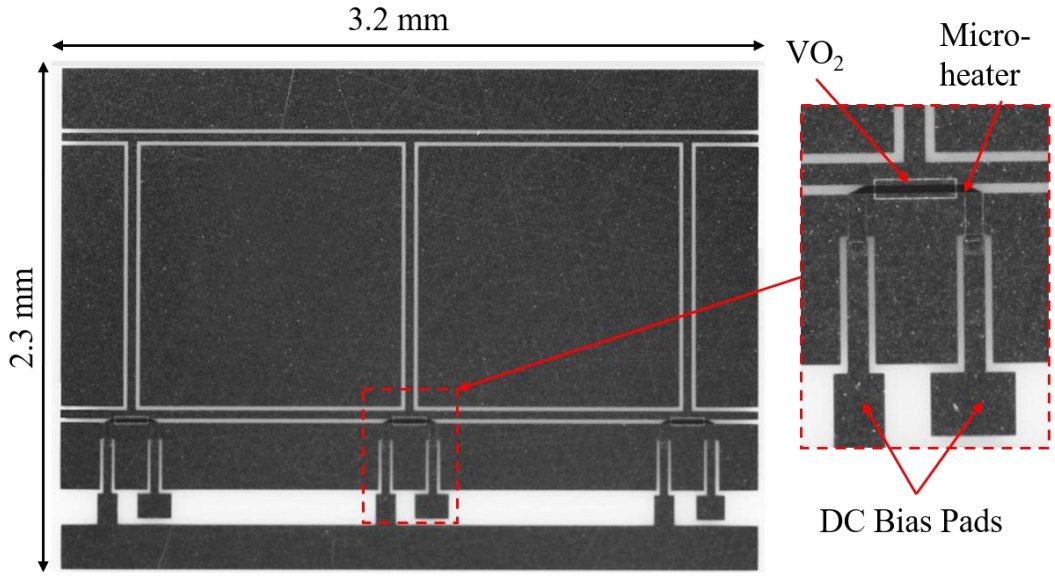

Figure 3-15. Image of fabricated variable attenuator showing dimensions for 30 GHz variable attenuator [85].

The variable attenuators are fabricated with the same fabrication process discussed in section 3.1.3. Figure 3-15 shows an image of the fabricated variable attenuator. The overall size is 3.2 mm × 2.3 mm for the 30 GHz variable attenuator and 8.4 mm × 6 mm for the 10 GHz attenuator. Micro-heaters are inserted under the gap of the signal line and the ground of the coplanar waveguide (CPW) line so that there is no overlap between the micro-heater and the signal line. This can significantly reduce the parasitic capacitance from the signal line to ground, which will then lower the insertion loss of the attenuator.

3.2.3 Simulation and Measurement Results

The sheet resistance of the thin-film VO_2 is determined by the thickness and the quality of the film in the fabrication process. Hence, a characterization of the VO_2 sheet resistance is performed with a simple structure, as shown in Figure 3-16 (a). The measurement is done with four DC probes. The top two pads are connected to the VO_2 film for measuring the sheet resistance, while the bottom two pads are for DC bias. Figure 3-16 (b) shows the sheet resistance of the sputtered thin-film VO_2 versus the voltage applied to the micro-heater. When the applied voltage is from 8 V to 14 V, a change of sheet resistance is observed from 48 Ω/□ to 47 kΩ/□. A difference of three orders of magnitude is realized for the change of sheet resistance.

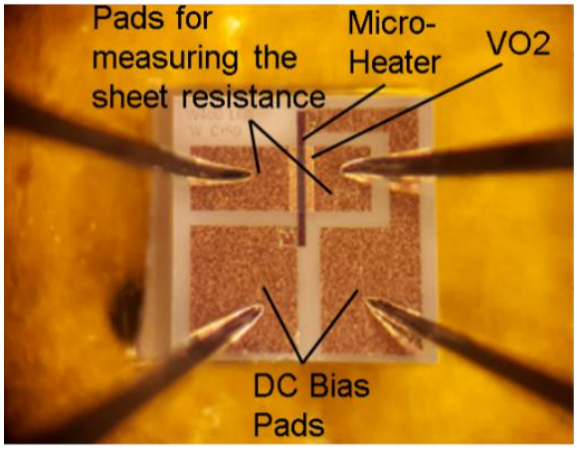

(a)

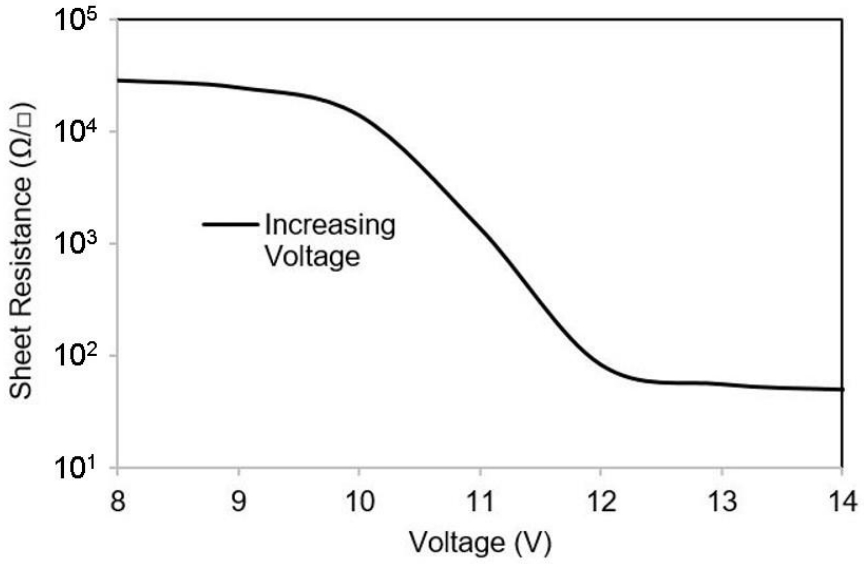

(b)

Figure 3-16. Graph depicting (a) test structure and (b) sheet resistance (in logarithmic scale) of the VO_2 thin-film versus voltage applied to the micro-heater.

The simulation results of the 10 GHz variable attenuator are shown in Figure 3-17 (a) and (b). An attenuation of 2.5 dB to 23 dB is obtained as the sheet resistance of the thin-film VO_2 is varied from 48 Ω/□ to 47 kΩ/□. The measured results given are shown in Figure 3-18 (a) and (b). The measurement is done while Port 2 and Port 4 of the 0-dB coupler are terminated with 50 Ω loads. The device exhibits a variable attenuation range of 9 dB with a return loss of 10 dB from 9.5 to 11.5 GHz.

The simulation results for the 30 GHz variable attenuator are shown in Figure 3-19 (a) and (b). An attenuation of 3.1 dB to 17 dB is obtained as the sheet resistance of the thin-film VO_2 is varied from 48 Ω/□ to 47 kΩ/□. The measured results are given in Figure 3-20 (a) and (b). The measurement is done while Port 2 and Port 4 of the 0-dB coupler are terminated with 50 Ω loads. The device exhibits a variable attenuation range of 13 dB with a return loss of 15 dB from 27 to 33 GHz.

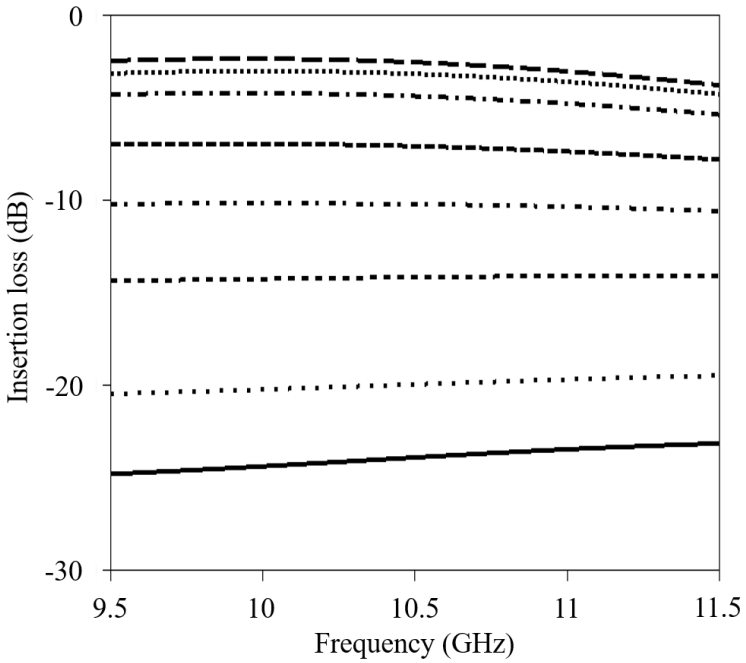

(a)

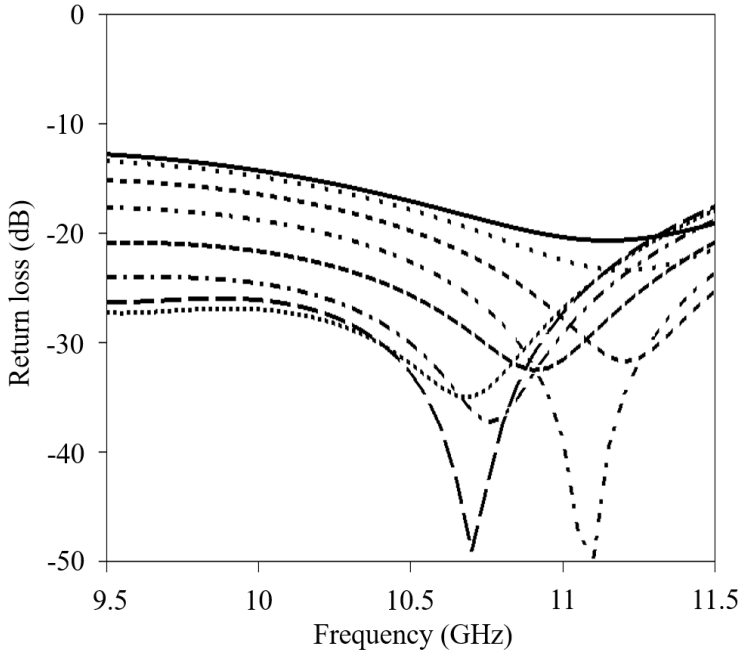

(b)

Figure 3-17. EM simulation results for 10 GHz variable attenuator: (a) insertion loss; (b) return loss.

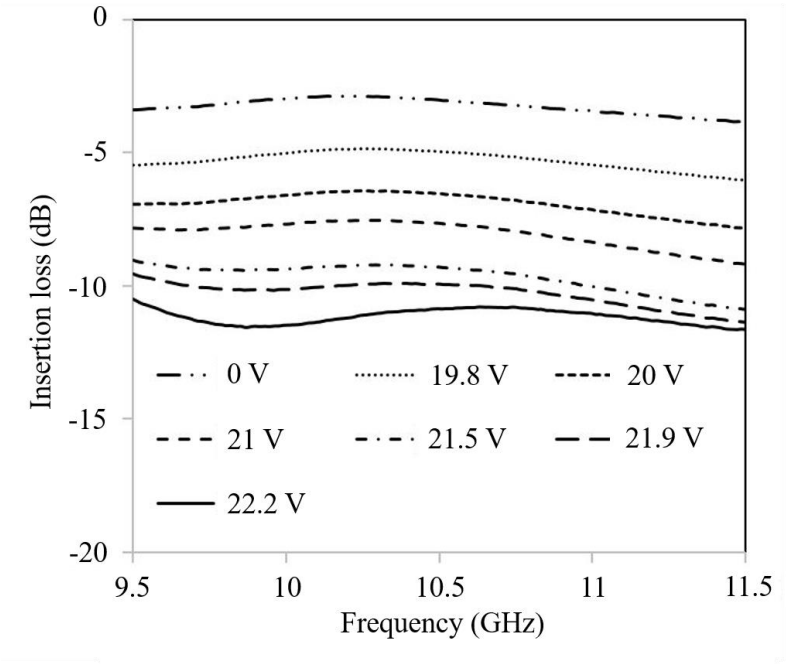

(a)

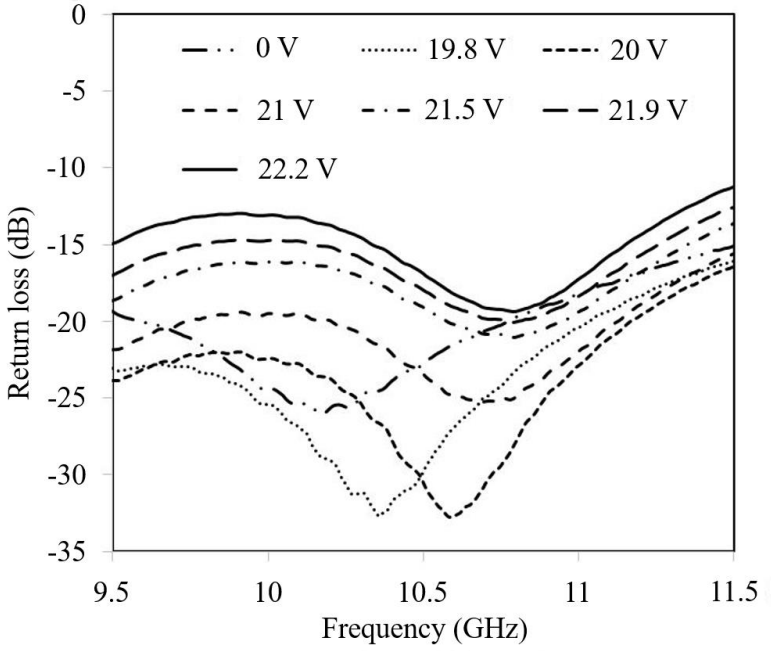

(b)

Figure 3-18. Measurement results for 10 GHz variable attenuator: (a) insertion loss; (b) return loss.

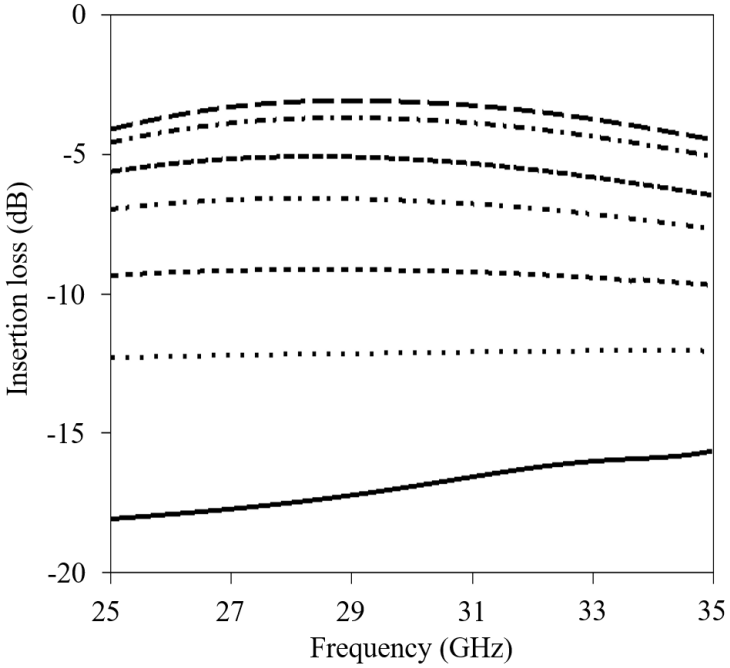

(a)

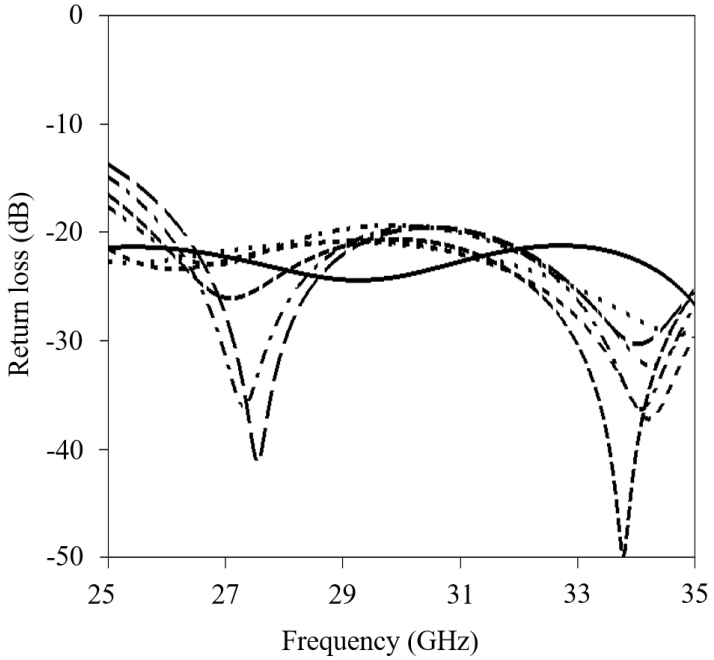

(b)

Figure 3-19. EM simulation results for 30 GHz variable attenuator: (a) insertion loss; (b) return loss.

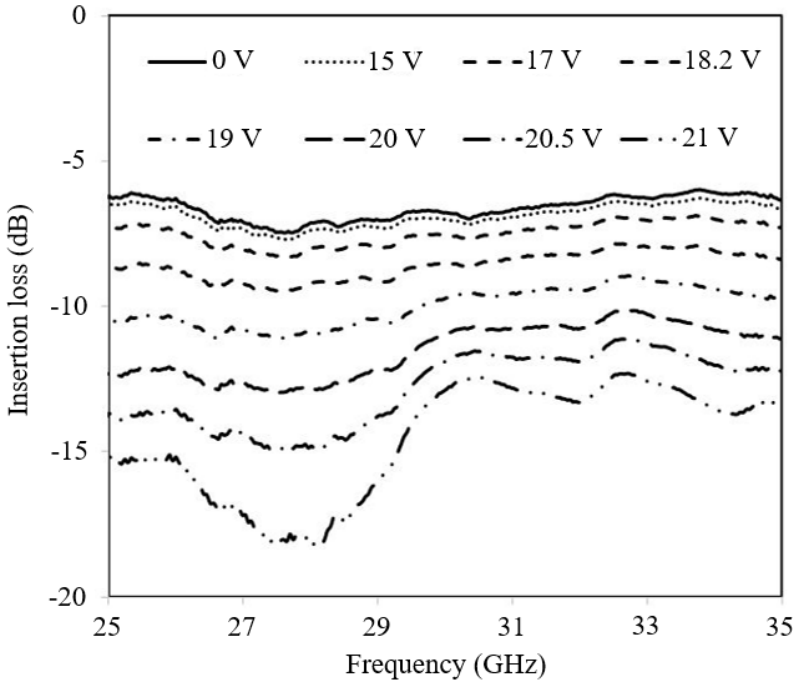

(a)

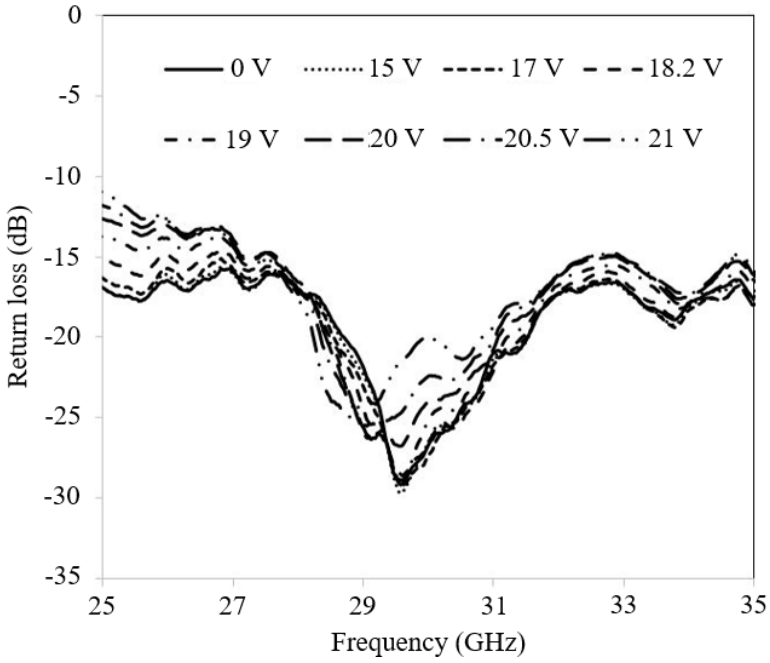

(b)

Figure 3-20. Measurement results for 30 GHz variable attenuator: (a) insertion loss; (b) return loss.

It should be mentioned that heater size in the test structure in Figure 3-16 (a) differs from that used in the attenuator given in Figure 3-15. However, both the test structure and the attenuator are fabricated in the same wafer. In the measurement, we used the same bias voltage for all resistors, which in turn varied the resistors by the same amount. Better return loss performance can be achieved by using non-synchronous tuning, where the resistors are biased differently. The measured insertion loss is slightly larger than that obtained by simulation due to radiation loss, since the device was tested without cavity housing. The performance can be further improved through increased optimization of the attenuator fabrication process and better quality VO_2 film.

3.2.4 Summary

In this section, 10 GHz and 30 GHz variable attenuators were designed, fabricated, and measured. A monolithic fabrication process for the VO_2-based attenuator on a single chip was described in detail. Micro-heaters using Cr were fabricated on the same chip for thermally actuating the thin-film VO_2. This variable attenuator promises to be useful in a wide range of millimeter wave applications.

3.3 GeTe-based RF Switches

3.3.1 Design and Fabrication

The basic geometries of the series GeTe-based RF switches are presented in Figure 3-22. The 3D exploded illustration of the designs is presented in Figure 3-22 (a), showing all layers and their materials. Figure 3-2 depicts an image of the fabricated switch. The CPW line of the switch is designed with a signal line width of 24 µm, a gap of 10 µm, and a length of 600 µm. The micro-heater is designed with a length of 200 µm and a width of 4 µm and 15 µm. An outline of the fabrication process is given in Figure 3-23.

In this process, a 2.5-inch by 2.5-inch alumina substrate with a thickness of 25 mil is used. A 100-nm thin-film tungsten (W) layer is first deposited and patterned for the micro-heater. The 100-nm W layer is deposited with DC sputtering and patterned with RIE. Next, a 60-nm SiN_x

layer is deposited by PECVD to form a barrier layer between the patterned W layer and the upcoming GeTe and Au layers. A 150-nm thin-film GeTe is then deposited with DC sputtering and patterned with lift-off, after which a 350-nm gold layer is deposited with e-beam evaporation and patterned with lift-off. Following the gold layer, a 50-nm SiO_2 passivation layer is deposited with DC sputtering and patterned with lift-off.

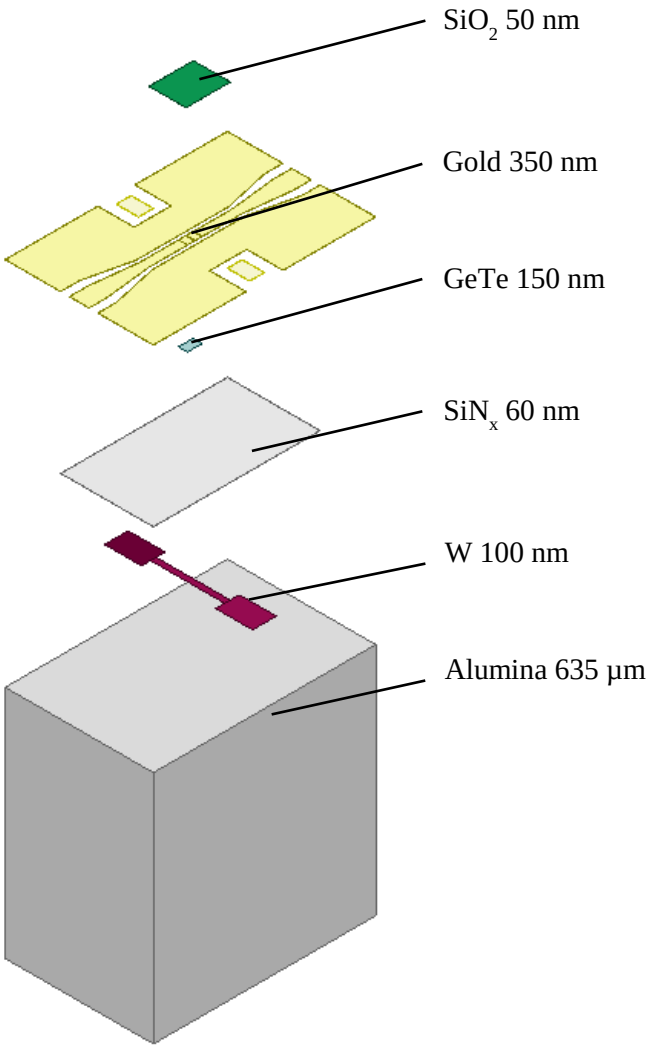

Figure 3-21. 3D view for each layer of designed GeTe-based series switch.

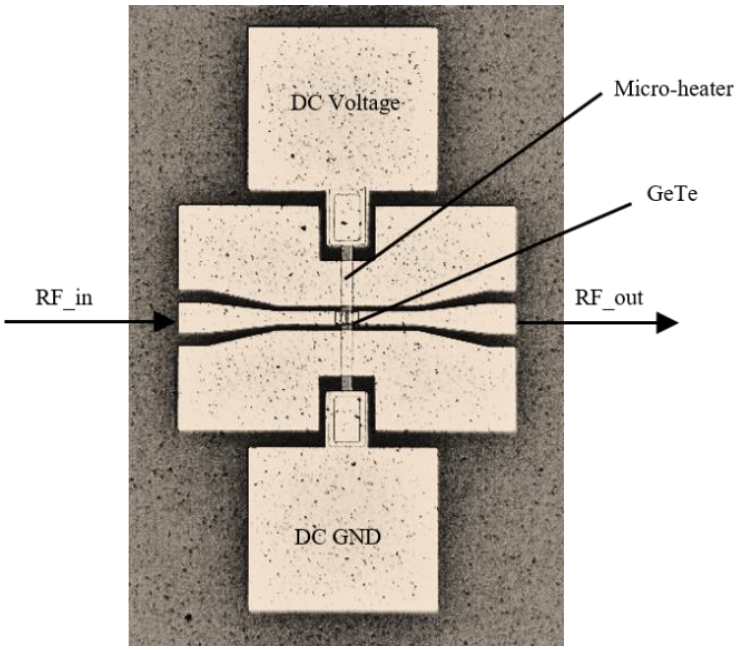

Figure 3-22. Image of fabricated GeTe series switch.

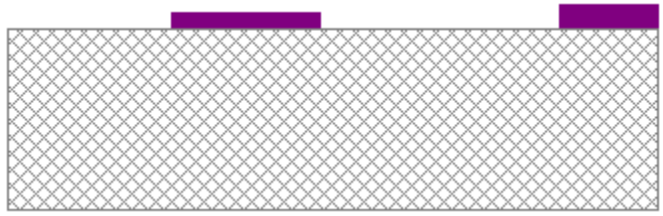

(a)

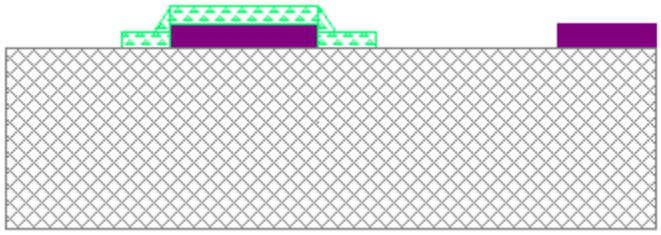

(b)

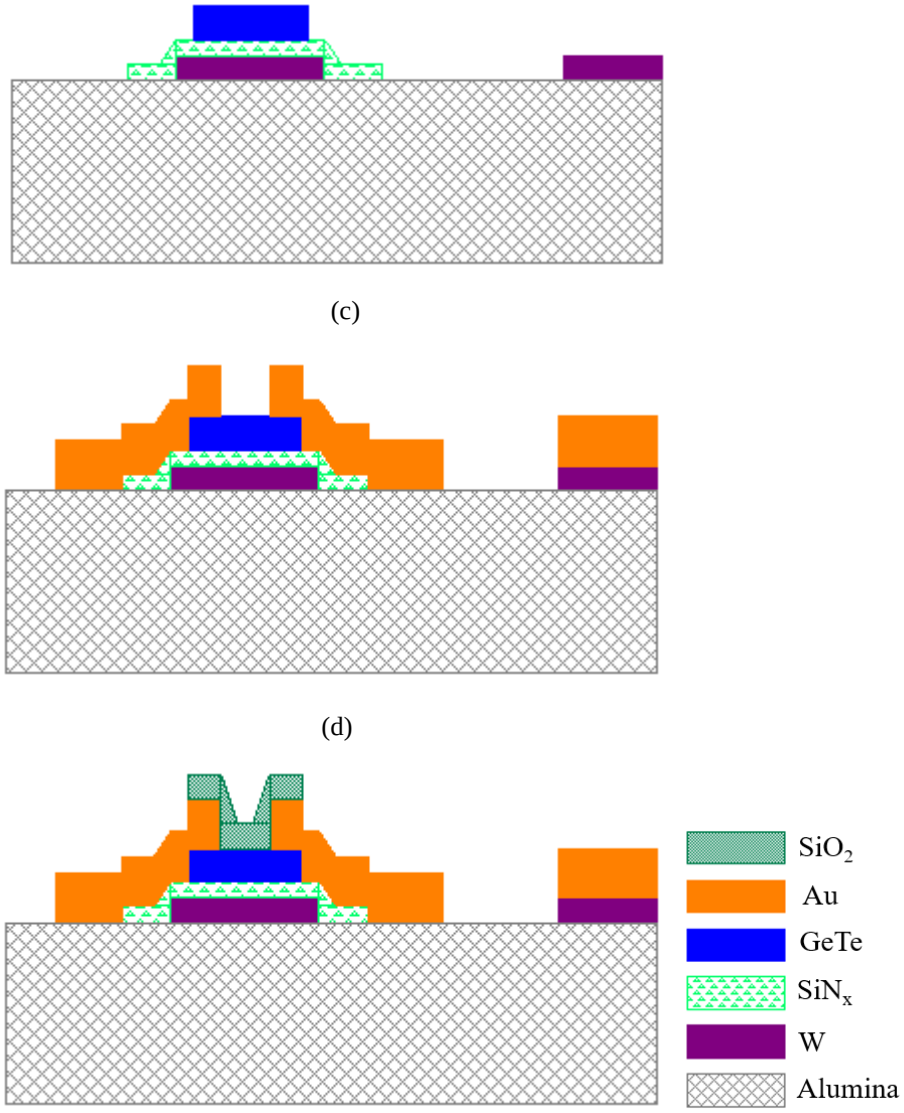

Figure 3-23. Fabrication process for GeTe-based series switch.

3.3.2 Simulation and Measurement Results

GeTe-based series switches with the above-mentioned fabrication process are design and fabricated. Since the SiN_x layer between the heater and the GeTe layer is only 100 nm, the switch performance is significantly influenced by the width of the heater. The simulated and measured results for two series switches with a heater width of 4 μm and 15 μm are compared.

Electromagnetic (EM) simulations of the switches are performed using ANSYS Electronics desktop. Figure 3-24 illustrates the simulated S parameters for the series switch with a heater width (W_heater) of 4 μm. The isolation is larger than 21 dB with a return loss smaller than 0.12 dB for the OFFstate from DC to 25 GHz. The insertion loss is smaller than 0.2 dB when the return loss is from DC to 30 GHz.

The simulation results for the W_heater of 15 μm is illustrated in Figure 3-25. The isolation is larger than 12 dB with a return loss smaller than 0.5 dB for the OFF state from DC to 25 GHz. The insertion loss is smaller than 0.55 dB when the return loss > 14 dB from DC to 25 GHz.

The RF performance of the switches is measured with two-port on-wafer measurements using a vector network analyzer up to 25 GHz. The measured S parameter for the series switch with a W_heater of 4 μm is illustrated in Figure 3-26. At the OFF state, the switch shows an isolation of > 26 dB, while the return loss is < 0.45 dB from DC to 25 GHz. At the ON state, an insertion loss of < 0.9 dB and a return loss of > 15 dB from DC to 25 GHz are realized.

Figure 3-27 illustrates the measured S parameter for the series switch with a W_heater of 15 μm. In the OFF state, the switch shows an isolation of > 12 dB, while the return loss is < 1 dB from DC to 25 GHz. In the ON state, an insertion loss of < 1.9 dB and a return loss of > 8 dB from DC to 25 GHz are realized.

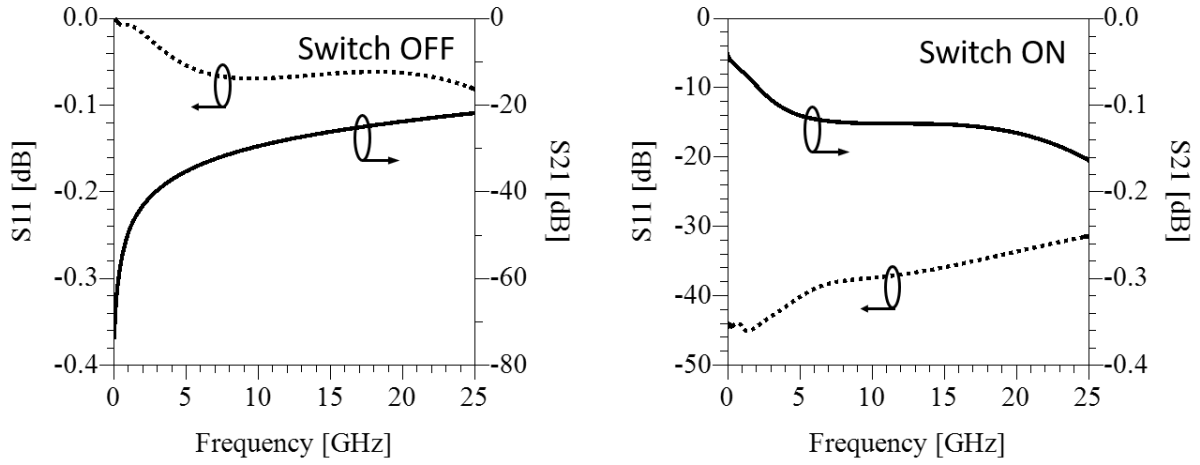

(a) (b)

Figure 3-24. Simulation results for W_heater = 4 μm: (a) switch OFF; (b) switch ON.

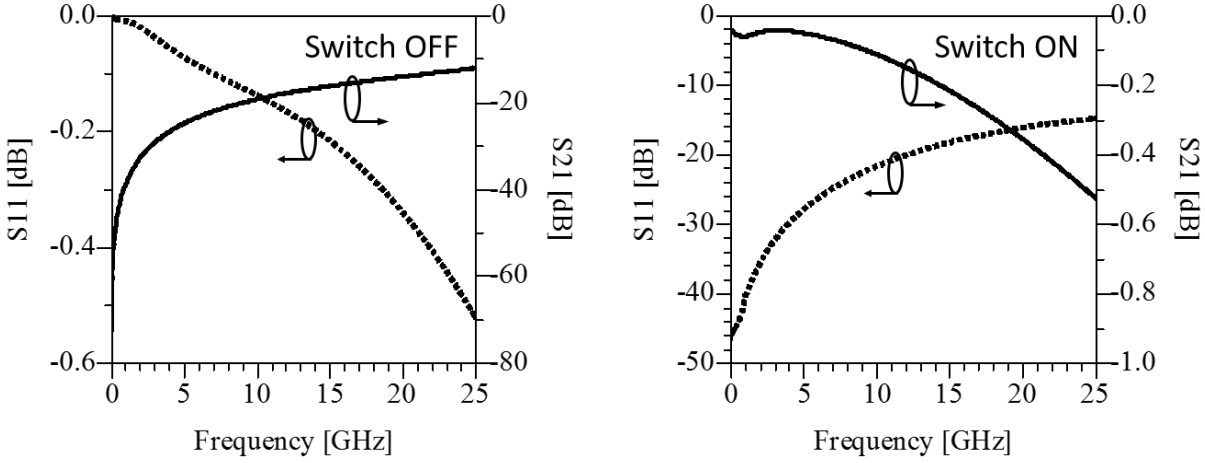

(a) (b)

Figure 3-25. Simulation results for W_heater=15 µm: (a) switch OFF; (b) switch ON.

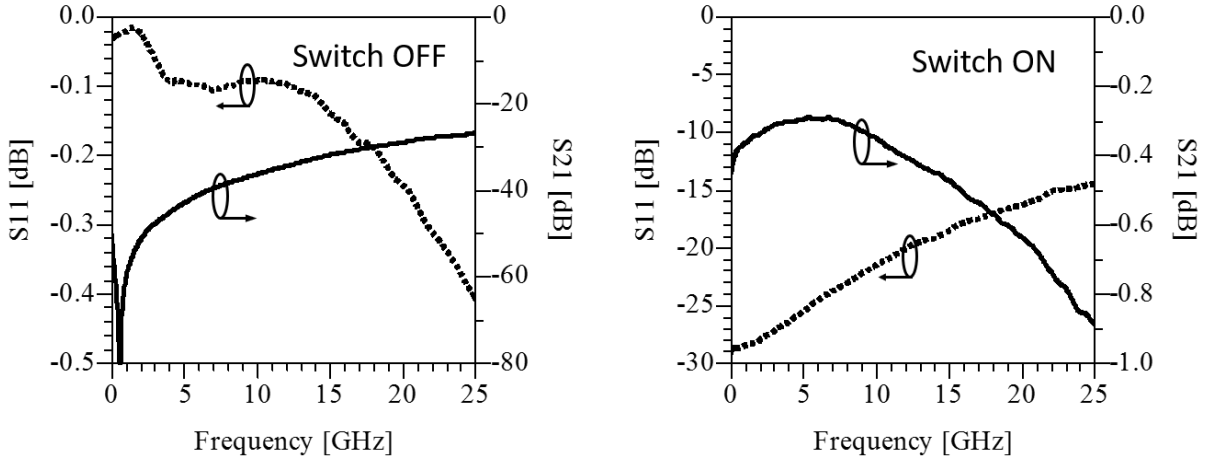

(a) (b)

Figure 3-26. Measurement results for W_heater=4 µm: (a) switch OFF; (b) switch ON.

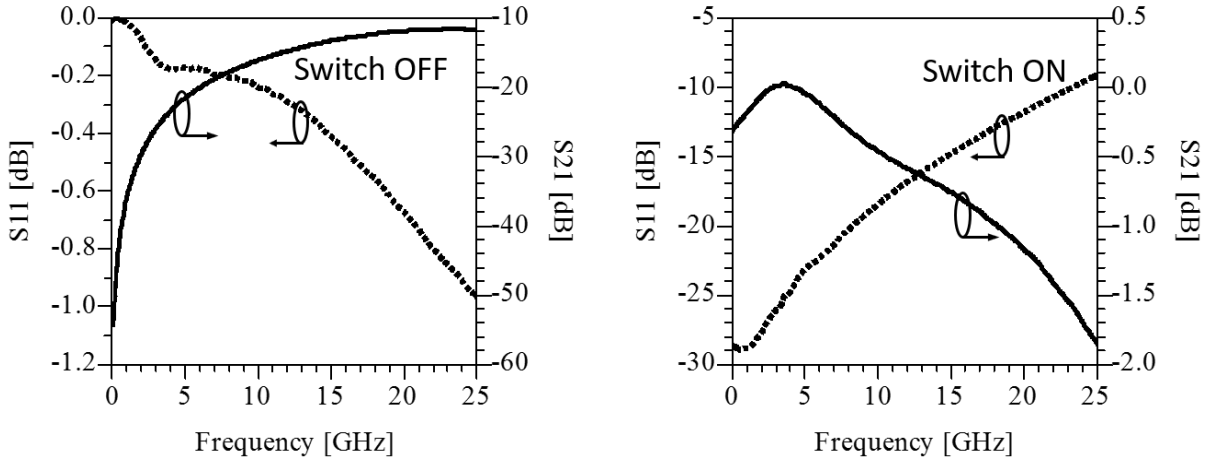

(a) (b)

Figure 3-27. Measurement results for W_heater=15 μm: (a) switch OFF; (b) switch ON.

3.3.3 Summary

Microfabrication processes for GeTe-based RF switches were developed and two series switches with different heater width were designed, fabricated, and measured. The performance of the two switches show that with this process, the heater width for the RF switch is very important for realizing low insertion loss and good isolation.

3.4 GeTe-based 4-Bit Capacitor Bank

3.4.1 Introduction

Switched capacitor banks are key components in reconfigurable RF devices such as tunable filters [71] and impedance tuners [84]. The semiconductor capacitor banks in [87] and the MEMS switch-based capacitor banks in [88] are commercialized capacitor banks with performances suitable for lower frequency applications. A MEMS-based switch capacitor bank was recently published in [89] with an operational frequency range of 3-10 GHz. However, the capacitance range achieved was only 0.15-1.2 pF and was realized using a standard CMOS process, which is difficult to integrate monolithically with high-*Q* passive circuits.

The integration of commercial capacitor banks with tunable filters or impedance tuners usually requires the use of flip-chip technology or wire-bonding. This in turn adds additional losses and reduces the self-resonance frequency of the capacitor bank. The advantage of using Phase Change Material (PCM) technology is that its fabrication process is compatible with thin-film technology, making it easy to monolithically integrate the PCM capacitor bank with passive planar circuits for the realization of tunable filters and impedance tuners.

Metal-insulator-transition (MIT) material such as vanadium oxide (VO_2) and PCM such as germanium telluride (GeTe) have recently been researched for RF applications. VO_2-based series and parallel RF switches are presented in [74][76]. GeTe-based RF switches are reported with an excellent figure-of-merit in [90]-[92], while a GeTe-based RF switch integrated with a planar tunable filter has been reported in [90]. The MIT and PCM technologies have the potential to be used in monolithic realizations of a wide range of reconfigurable devices.

In the present study, a capacitor bank utilizing a GeTe-based RF switch is presented for the first time with a very compact size and demonstrating a large capacitance range from 0.48 pF to 4.53 pF. The capacitor bank is realized with a 6-layer micro-fabrication process based on a glass substrate with low thermal conductivity. The capacitor bank is formed by integrating four PCM switches with metal-insulator-metal (MIM) capacitors integrated on a single chip.

3.4.2 Design and Fabrication

The schematic of the proposed 4-bit capacitor bank is illustrated in Figure 3-28, showing GeTe-based RF switches (S_1 to S_4) connected in series with capacitors (C_1 to C_4). The capacitance values are chosen to be 0.25 pF, 0.5 pF, 1 pF and 2 pF at 5 GHz, and the parasitic capacitor is presented as C_p in the figure. C_p represents the minimum capacitance value, or State 1, of the possible 16 states of the capacitor bank, with all switches OFF.

The 3D EM simulation model of the 4-bit capacitor bank is shown in Figure 3-30, illustrating the four MIM capacitors and the four GeTe-based RF series-switches. The capacitors are built using gold for the top and bottom metal layers, and SiO_2 for the insulator layer. The switches are realized with phase-changing material GeTe and a Cr-W-Cr sandwiched micro-heater. The GeTe

switches have a width of 40 μm and a gap of 2 μm, while the micro-heaters have a width of 15 μm and a length of 60 μm. A barrier layer of SiN_x is used between the heater and the GeTe layer, due to its relatively high thermal conductivity.

An outline of the fabrication process is given in Figure 3-29. A 3-inch glass substrate is used in this fabrication process due to the much better thermal isolation it can offer in comparison with silicon or alumina wafers. In this process, a Cr-W-Cr sandwiched layer was first deposited and patterned for the micro-heater. The top and bottom Cr layers are both 30-nm deposited with e-beam evaporation; the bottom Cr is used as an adhesion layer, while the top Cr layer is used for protecting the W when etching the SiN_x layer. The 120-nm W layer was deposited with DC sputtering, and the Cr-W-Cr layer is patterned with RIE. Next, a 100-nm SiN_x layer is deposited by PECVD as the barrier layer between the patterned Cr-W-Cr layer and the upcoming GeTe and Au-1 layer. A 140-nm thin-film GeTe is then deposited with DC sputtering and patterned with lift-off, after which a 300-nm gold layer (Au-1) is deposited with e-beam evaporation and patterned with lift-off. A 220-nm SiO_2 layer is deposited next, with DC sputtering and patterned with lift-off. Lastly, a 500-nm gold layer is deposited with e-beam evaporation and patterned with lift-off.

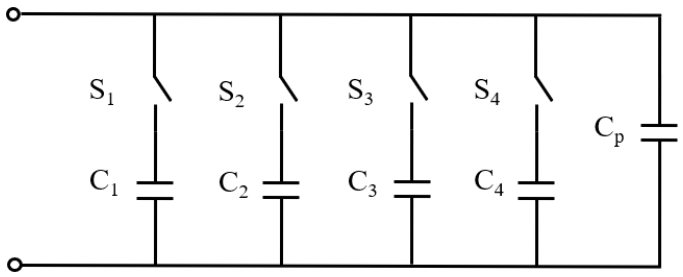

Figure 3-28. Schematic of 4-bit capacitor bank.

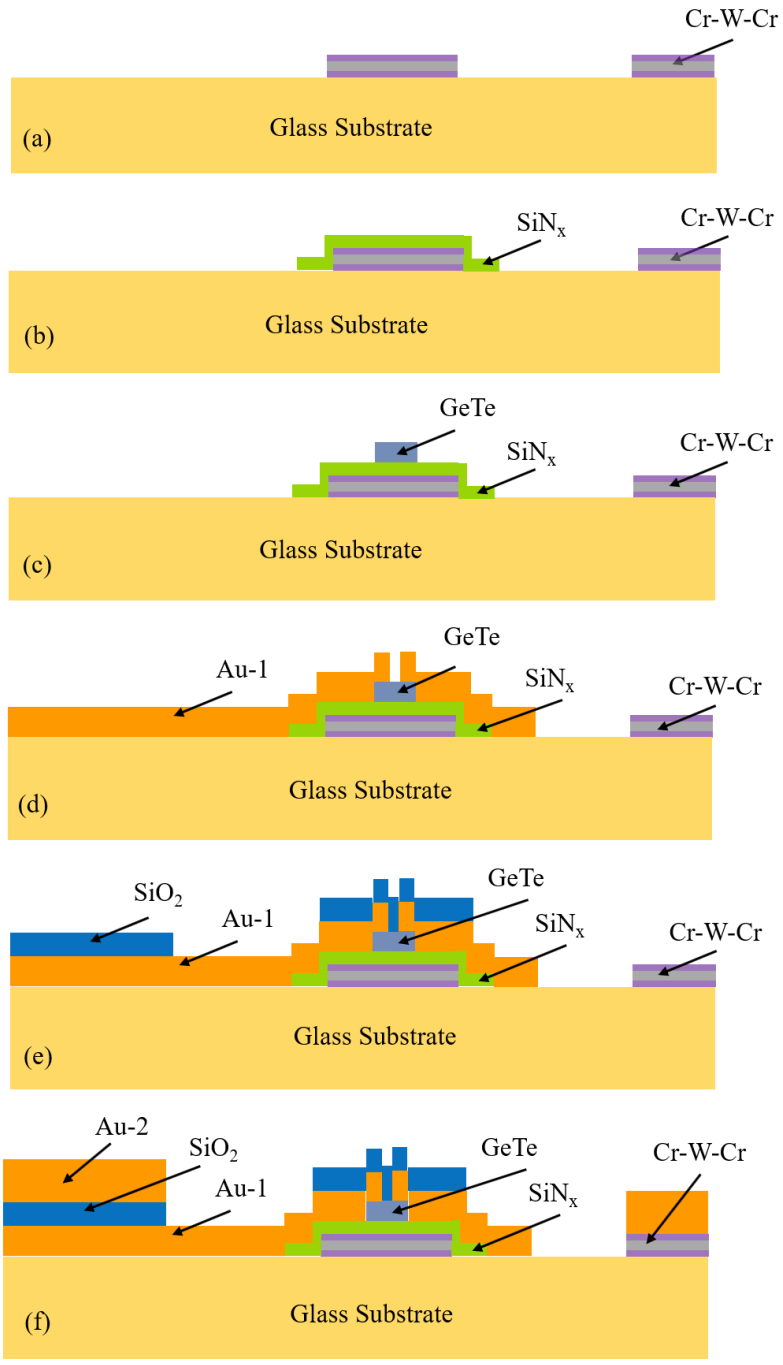

Figure 3-29. Fabrication process for Ge-Te-based switched capacitor bank [93].

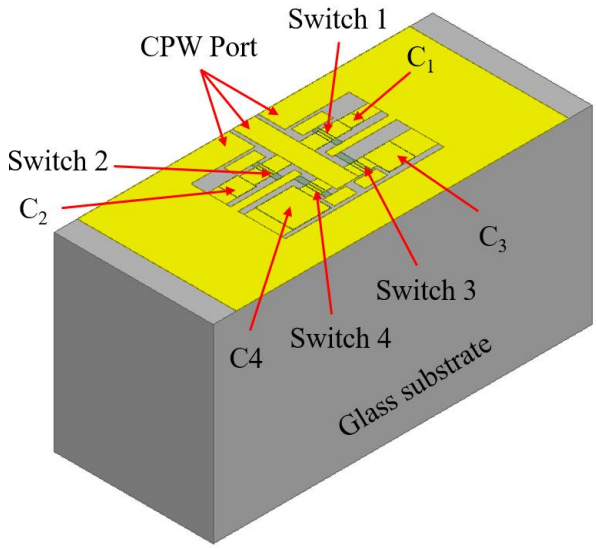

Figure 3-30. Simulation model for 4-bit capacitor bank.

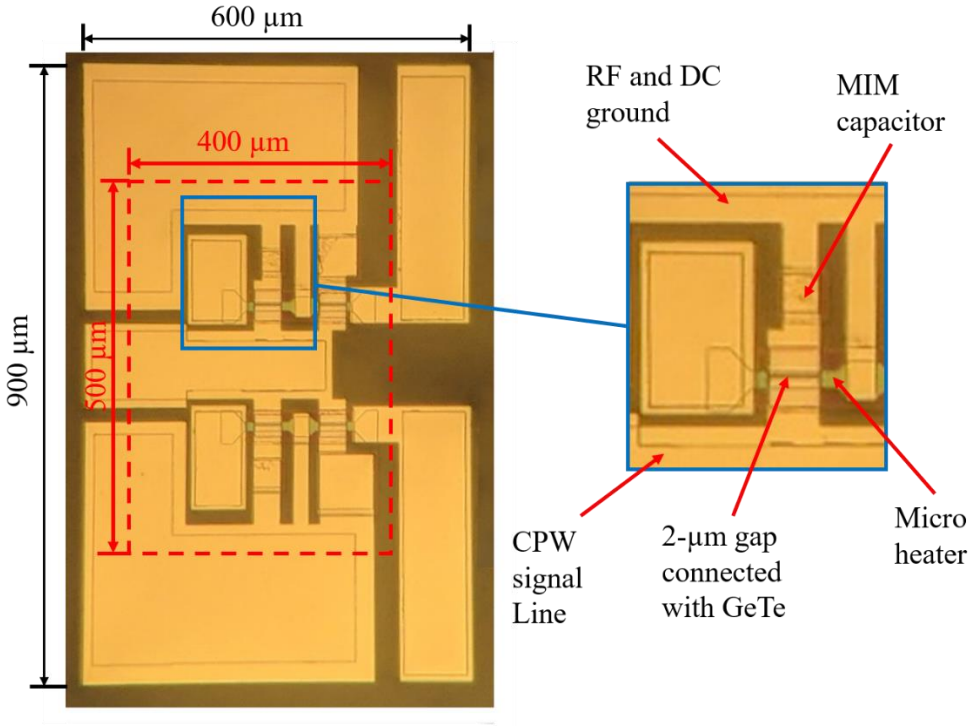

Fig. 3-31. Image of fabricated 4-bit capacitor bank.

The parameters for depositing the thin-film W and GeTe with DC sputtering system are summarized in Table 3-2. Both W and GeTe sputtering targets have a diameter of 2 inches and a

thickness of 0.25 inches. Photographs of the 4-bit capacitor bank are shown in Fig. 3-31. The total size of the capacitor bank is 0.9 mm × 0.6 mm, including the CPW port and DC pad for measurement. In real applications, when the capacitor bank is integrated monolithically with other circuits on the same substrate, the size of the capacitor bank can be potentially reduced to 0.5 mm × 0.4 mm.

Table 3-2. Summary of W and GeTe deposition parameters

Material	Parameter	Value
W	DC Power	80 Watts
	Chamber Base Pressure	2 μTorr
	Deposition Pressure	3 mTorr
	Substrate Temperature	500° C
	Deposition Rate	16 nm/min
GeTe	DC Power	60 Watts
	Chamber Base Pressure	2 μTorr
	Deposition Pressure	2.5 mTorr
	Substrate Temperature	Room Temperature
	Deposition Rate	28 nm/min

3.4.3 Simulation and Measurement Results

The 4-bit capacitor bank is simulated using HFSS for the 3D model shown in Figure 3-30. Figure 3-32 illustrates the EM simulation results for the 16 states. The results show a 0.1 pF parasitic capacitance at state 1 when all the GeTe switches are OFF. At 1 GHz, the capacitor tuning range is from 0.1 pF to 3.1 pF, while at 6 GHz, the tuning range is from 0.1 pF to 4.4 pF. The simulation results for all states show no self-resonance up to 9 GHz.

Figure 3-33 shows the circuit model of the presented 4-bit capacitor bank. Each of the MIM capacitors can be modeled with a capacitance C_n, a parallel resistance R_{pn}, a series inductance L_{sn}, and a series resistance R_{sn}. The values of these elements are extracted from the EM simulation results of the individual MIM capacitors. The PCM switches are simply modeled as

resistors in the ON state. L_p and C_p are the parasitic inductance and capacitance of the circuit, respectively, mainly due to the CPW port, connection lines, and micro-heater. The series resistances R_{sn} of the capacitors were found to be 2.39 Ω, 1.93 Ω, 1.33 Ω and 1.04 Ω, respectively. These are the dominant parameters that affect the *Q* value of the capacitor bank. It should be noted, however, that a much better *Q* can be achieved with the use of larger dimensions for the MIM capacitors and a thicker SiO_2 layer. Thus, one has to compromise between the overall chip size and the achievable *Q* value.

Figure 3-34 illustrates the measurement results of the 4-bit capacitor bank, indicating a capacitor tuning range of 0.45 pF to 2.84 pF at 1 GHz, and 0.48 pF to 4.53 pF at 6 GHz. Hence, it almost has a capacitor ratio of 10:1 at 6 GHz, which is a very large tuning range. Figure 3-35 shows states 1, 8 and 16 of the 4-bit capacitor bank on the Smith chart. As can be seen from the chart, the capacitor bank does not exhibit self-resonance up to 8 GHz, which makes it suitable for reconfigurable/tunable RF passive device applications over a frequency band of 1 GHz to 6 GHz.

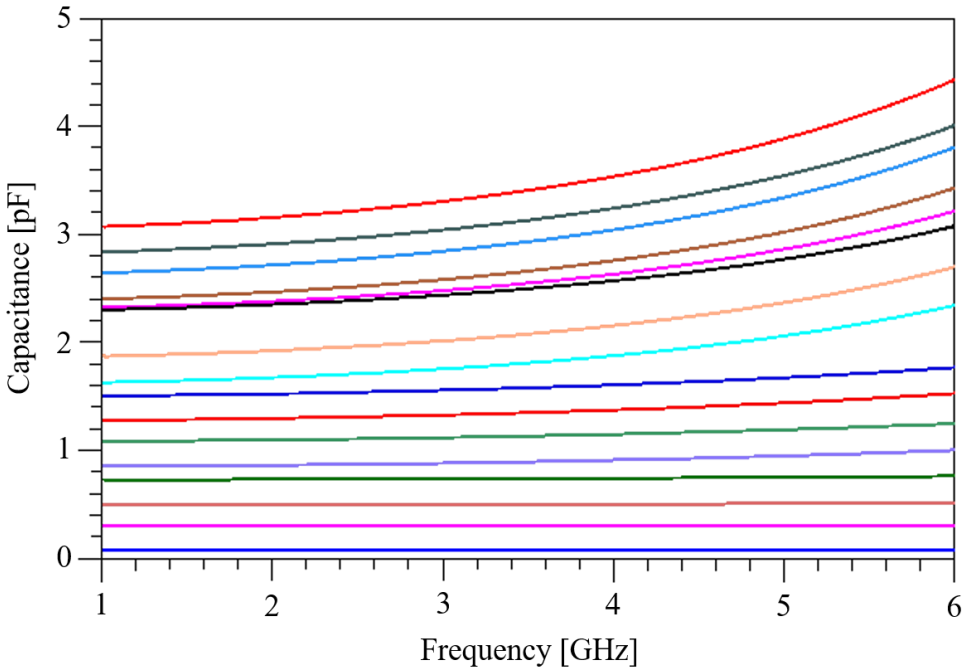

Figure 3-32. Simulation results for 4-bit capacitor bank.

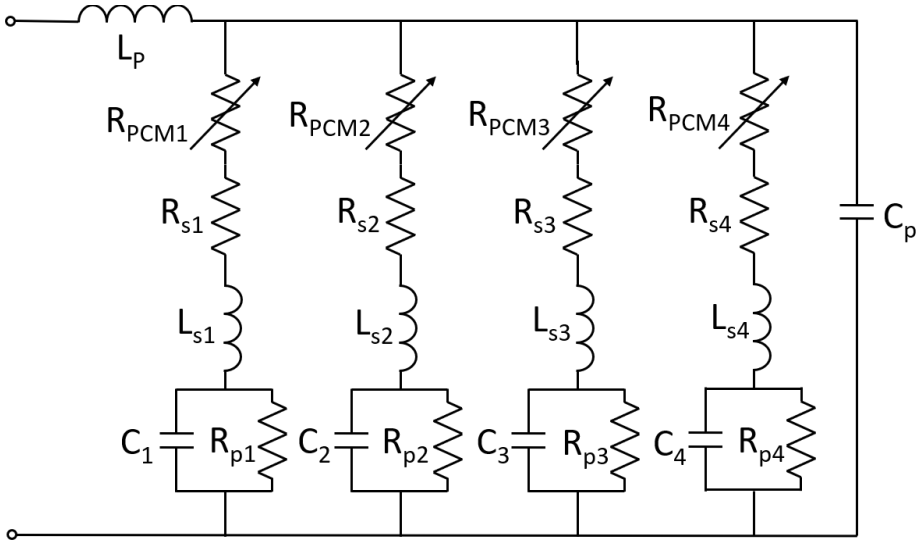

Figure 3-33. Circuit model for 4-bit capacitor bank.

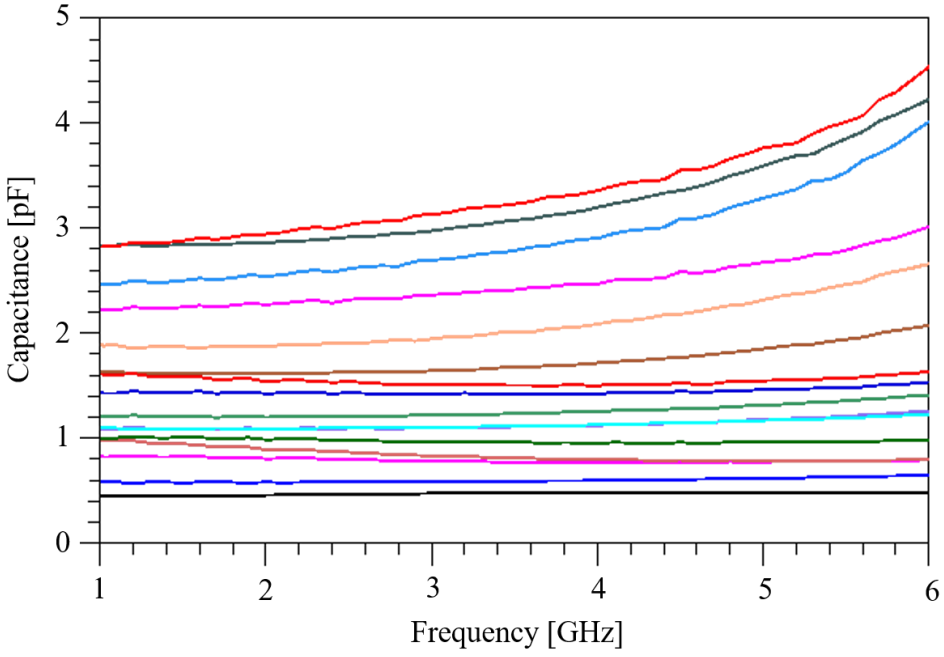

Figure 3-34. Measurement results for 4-bit capacitor bank.

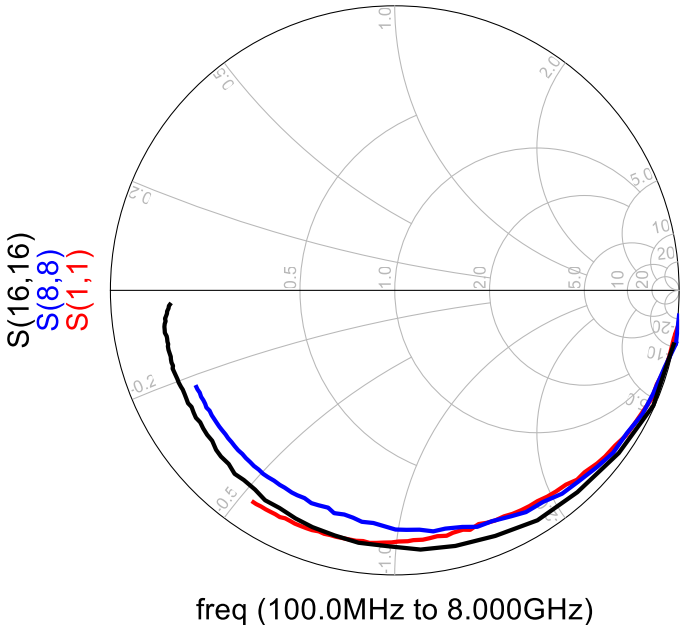

Figure 3-35. Measurement results plotted on a Smith chart.

3.4.4 Summary

In this section, a 4-bit GeTe-based capacitor bank was designed, fabricated and measured. As well, a monolithic fabrication process for the GeTe-based capacitor bank on glass substrate was presented in detail. Gold-based MIM capacitors were fabricated and integrated with GeTe-based RF switches, and Cr-W-Cr sandwiched structures were utilized for realizing good adhesion and a low sheet resistance resistor layer for micro-heaters. The presented capacitor bank is highly compact in size, offering a wide tuning range and the convenience of monolithic integration with other RF components.

Chapter 4
Wideband Dielectric Substrate-based Cavity Filter

4.1 Introduction

Filters are essential components in wireless communication and radar systems. Three-dimensional (3D) filters such as VO_2 waveguide [94] – [95], dielectric resonators [96] – [97], substrate integrated waveguides [98] and combline structures [99] are widely used in these systems due to their high quality (*Q*) factor. The use of dielectric resonators (DR) can significantly reduce filter size while achieving high *Q* values and excellent thermal stability, even with cavity enclosures made of aluminum [100]. Traditionally, dielectric resonators are mounted inside a cavity metal enclosure, either sitting on a support made of low dielectric constant such as Teflon [100] – [101] or directly on the cavity walls [102] – [103]. However, these types of filter

structures are limited to fractional bandwidth designs of less than 5%, and assembly and integration is considered a major production cost factor.

An alternative approach was developed in [104] that uses a single piece of high-K ceramic substrate, which promises to produce low profile designs and reduce the cost of assembly and integration. However, the structure proposed in [104] is applicable to narrow bandwidth applications. This is attributed to the nature of the dielectric resonator mode used in [104], which is a variation of TEH modes. More recently, miniature dielectric resonator filter designs with the capability of realizing relatively wide bandwidth (3.2%) have been proposed in [105] – [106]. However, such structures require extensive machining of the dielectric resonators. Not only does this add to the cost and design complexity, but the spurious mode is close to the passband. A dual-mode compact dielectric resonator filter is reported in [107], which realized a fractional bandwidth of 10.5%. However, only a two-pole filter is reported with a single cavity, no results were reported in [107] that demonstrate the feasibility of achieving large inter-resonator coupling values that are needed to realize wideband highorder filters.

In view of the typical filter requirements for sub-6 GHz 5G systems, there is a need for filters which are wideband (around 10%), low loss, compact in size, and have a thin profile.

This study proposes a dielectric substrate (DS)-based filter, constructed using two metal covers and a metal frame holding two thin high dielectric constant substrates (ε_r = 41.5). The frame is assembled with the two metal covers to form the filter, as shown in Figure 4-1.

The main features of the proposed filter structure are as follows:

(1) The structure makes it possible to realize relatively high-*Q* wideband dielectric filters.
(2) The structure is easy to assemble due to the unique design of attaching the DS to the metal frame. The dielectric substrates are implemented by dicing a larger size substrate, which can also help to reduce cost, particularly when dealing with filters in large orders.
(3) The filter is compact in size and has a relatively thin profile, which makes it amenable to ease of integration with antennas.
(4) Since the thickness of the DS is suitable for microfabrication, it offers the potential of ease of realizing tunable dielectric filters with tuning elements directly deposited on the DSs.

4.2 Proposed Compact DS-loaded Cavity Resonator

The 3D view of the proposed structure for the DS-loaded cavity resonator is shown in Figure 4-1. The cavity consists of a metal frame, two DSs, and two covers. The two metal covers and the frame, after mounting the DSs, are bolted together using screws. Figure 4-2 shows the dielectric substrates used in this study, the original DSs as ordered are shown in (a) and the diced DSs are shown in (b).

The electric field (E-field) of the resonator obtained with eigenmode simulation is shown in Figure 4-3. In Figure 4-3 (b), the E-field is relatively large between the two dielectric substrates, which makes it possible to insert a probe in between that helps to realize a relatively large input/output coupling.

For conventional DR-loaded cavity mode resonators [96], it is not easy to realize strong input and output coupling. This is attributable to the fact that for conventional DR-loaded cavities operating in the fundamental TEH mode, the electric field is concentrated inside the DR at its center, not on the resonator top and bottom surfaces. This, in turn, makes it challenging to achieve strong input/output couplings.

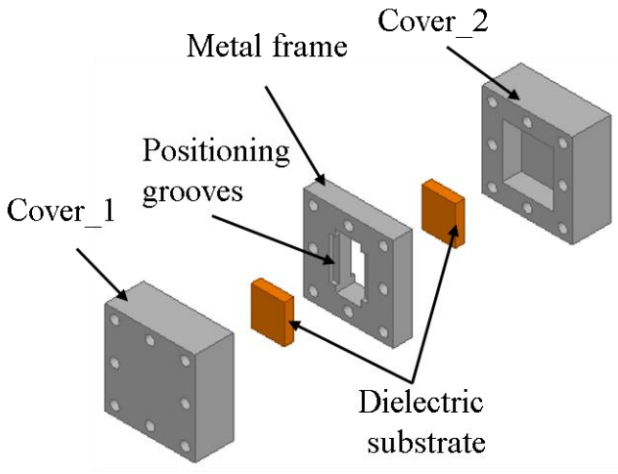

Figure 4-1 3D diagram of proposed DR-loaded cavity resonator.

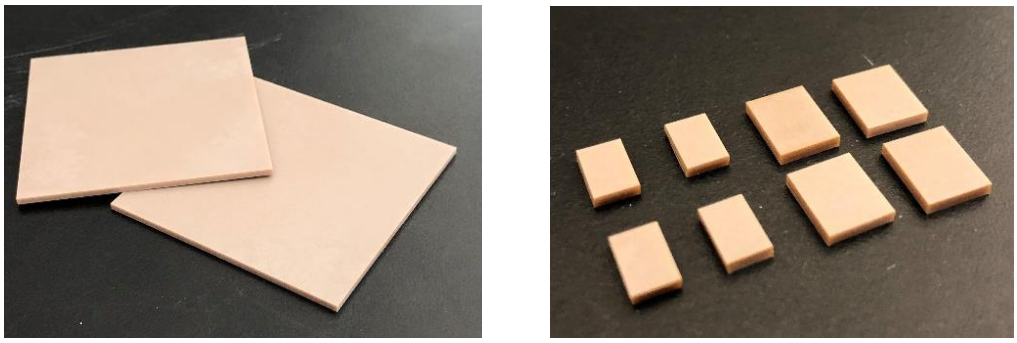

(a) (b)

Figure 4-2 Image of the dielectric substrate. (a) DSs not diced; (b) DSs diced.

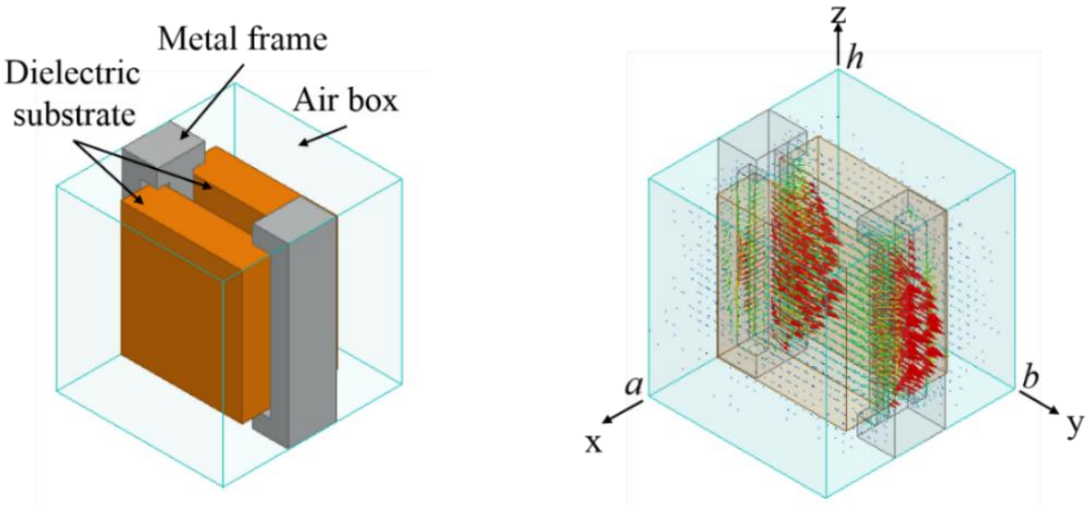

(a) (b)

Figure 4-3 Diagram (a) and electrical field of the used resonance mode (b) of the proposed DR loaded cavity resonator.

4.2.1 Comparing Proposed Structure with Other DS-loaded Cavity Resonator Structures

Figure 4-4 shows different configurations of DS-loaded cavity resonators, with all the cavities the same size. In (a), a DS with a thickness of 3 mm is floating in the middle of the cavity. It should be mentioned that in the actual design, the DS would be supported by a dielectric material with low dielectric constant, such as Teflon. In (b), two thinner DSs, each with a thickness of 1.5

mm, are separated at a distance of 1.6 mm. The DSs in this figure are also floating in the middle of the cavity. In (c), the same DS as in (a) is used, with the DS touching the bottom of the cavity. In (d), two thin DSs identical to those shown in (b) are used, with the DSs touching the bottom of the cavity. The DSs in (e) and (f) are the same as those in (c) and (d), respectively, with the DSs touching both the top and bottom surfaces. The proposed cavity structure with the two DSs attached to the metal frame is shown in proposed design (g). All the cavity structures shown in Fig. 3 have the same cavity dimensions of 9 mm × 8.5 mm × 8.5 mm. A thickness of 3 mm is used when there is a single DS and a thickness of 1.5 mm is used when there are two DSs.

Table 4-1 shows the eigenmode simulation results of the seven resonator configurations. All simulation models in Figure 4-4 use DS with a dielectric constant of 41.5 and a loss tangent of 0.00012 at 5 GHz. The input group delay is simulated with the input port, as shown in Figure 4-5. The input probe has a diameter of 1.3 mm and a length of 6 mm. The distance between the probe and the DSs (0.18 mm) is kept the same for the cavity resonators.

From the comparison given in Table 4-1, we can see that configurations (e), (f) and our proposed design (g) offer the lowest fundamental mode frequencies among the seven designs (i.e., they have the potential to provide a miniature filter design). The input group delay for configuration (e) is 5.01ns, which is 4.4 times larger than that of the proposed structure (g). The high value of the input group delay for (e) translates to a lower input coupling value, indicating that much wider bandwidths can be realized by design (g). Note that resonators (e) and (f) have a *Q* value that is almost 50% that of our proposed design (g).

Since the main objective is to design a miniature wideband filter, proposed design (g) seems to be the optimum configuration among the seven cavity configurations illustrated in Fig. 3. As we will show later, the use of the proposed resonator (g) also makes it possible to realize large inter-resonator coupling values.

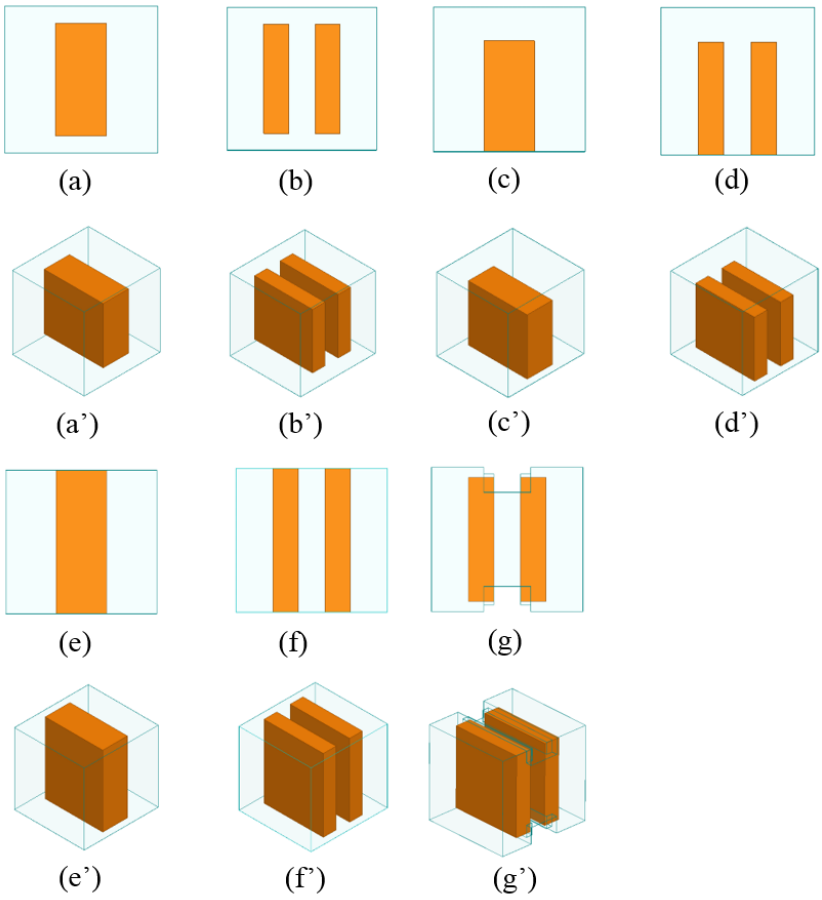

Figure 4-4 Several structures for DS-loaded cavity resonators. (a)-(g) is a side view of the resonators and (a')-(g') is the 3D view of the resonators.

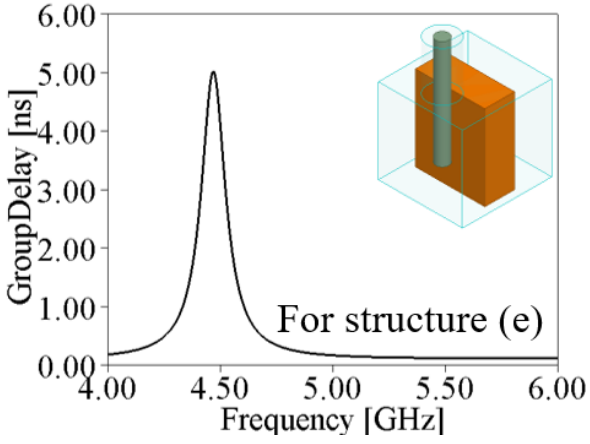

(a)

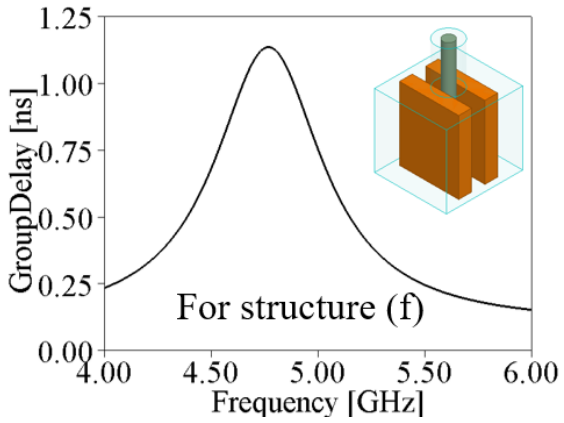

(b)

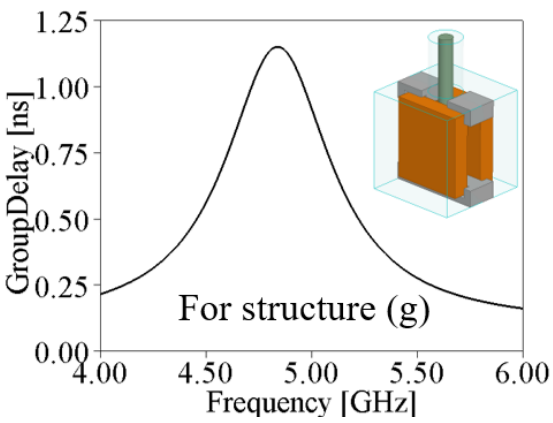

(c)

Figure 4-5 Input group delay of structure (e), (f), and (g) in Figure 4-4 with one port EM simulation.

Table 4-1 EM simulation results of different structures

Structures	Mode 1 f_0 (GHz)	Mode 2 f_0 (GHz)	Spurious free window (GHz)	Quality factor	Input group delay for Mode 1 (ns)	Ease of assembly
(a)	7.68	8.57	0.89	4870	8.68	Easy
(b)	8.82	9.33	0.51	4850	5.33	Easy
(c)	6.47	7.17	0.70	3000	2.87	Easy
(d)	7.35	7.83	0.48	3070	6.37	Easy
(e)	4.51	6.10	1.61	900	5.01	Not easy
(f)	5.14	6.93	1.79	870	1.14	Not easy
Proposed (g)	4.99	7.62	2.63	1880	1.15	Easy

Note: 1. Input groups are simulated with the same input port as shown in Figure 4-5. The input probe is 1.3 mm in diameter and 6 mm in length.
2. The distance between the probe and the DRs is 0.18mm. For (a), (b), (c) and (d), the location of the strongest electrical field is not at the center. The probe is placed at the location of the strongest electrical field, but not at the center, which can give maximum coupling.
3. For the electrical field shape of TEH mode, please see page 574 of reference [15].

4.2.2 Choosing DS Thickness

Figure 4-6 shows the impact of resonator thickness on resonant frequency, *Q* and spurious free window, if the thickness of the DS increases from 1 mm to 2 mm. Figure 4-6 (a), (b) and (c) show, respectively, that the resonance frequency drops from 5.55 GHz to 4.72 GHz, the *Q* drops from 2020 to 1820, and the spurious-free range decreases from 2.96 GHz to 2.4 GHz. Thus, when considering obtaining both a higher *Q* and larger spurious free range, a thinner DS is preferable. While not having a very high resonant frequency, a DS thickness of 1.5 mm was selected for our designs.

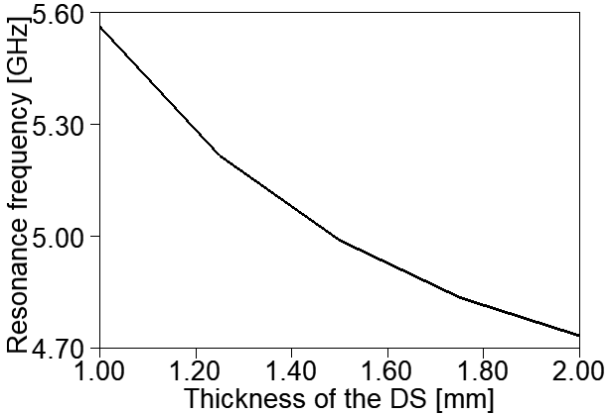

(a)

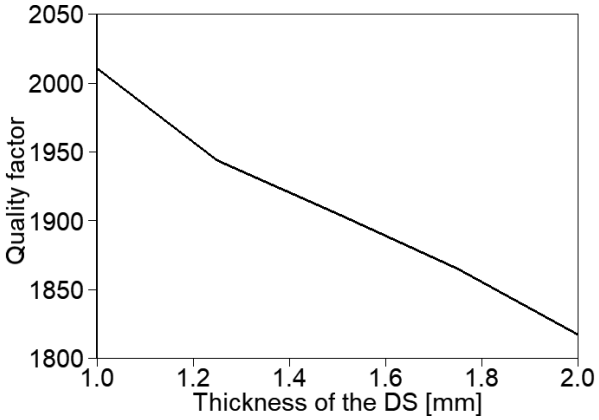

(b)

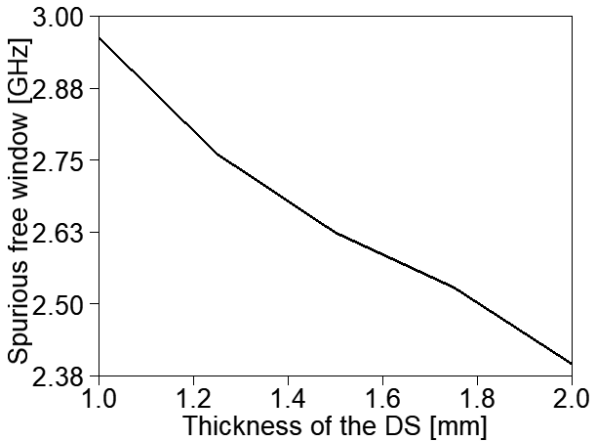

(c)

Figure 4-6 Change of parameters versus different thicknesses of DS: (a) change of resonance frequency; (b) change of *Q*; (c) change of spurious free window.

4.2.3 Inter-resonator Coupling

For the proposed DS-loaded cavity resonator, there are two different coupling approaches that are capable of realizing strong inter-resonator couplings. Figure 4-7 shows the electrical field of the first coupling type when the adjacent resonators are next to each other along the z direction (same axis as shown in Figure 4-3 (b)). We can see that the first mode in Figure 4-7 (a) is forming a magnetic wall between the resonators, while the second mode in Figure 4-7 (b) is forming an electrical wall between the resonators. The inter-resonator coupling M is thus [1]:

$$M = \frac{f_0}{BW}\frac{f_e^2 - f_m^2}{f_e^2 + f_m^2} \quad (1)$$

where f_0 is the center frequency of the filter, f_e is the resonance frequency of the resonance mode with an electrical wall between the two resonators, and f_m is the resonance frequency of the resonance mode with a magnetic wall between the two resonators.

Figure 4-8 shows the electrical field of the second coupling type when the adjacent resonators are next to each other along the x direction (same axis as shown in Figure 4-3 (b)). Both couplings are needed when realizing folded filter structures, as described earlier. Folding the filter makes it easy to realize transmission zeros.

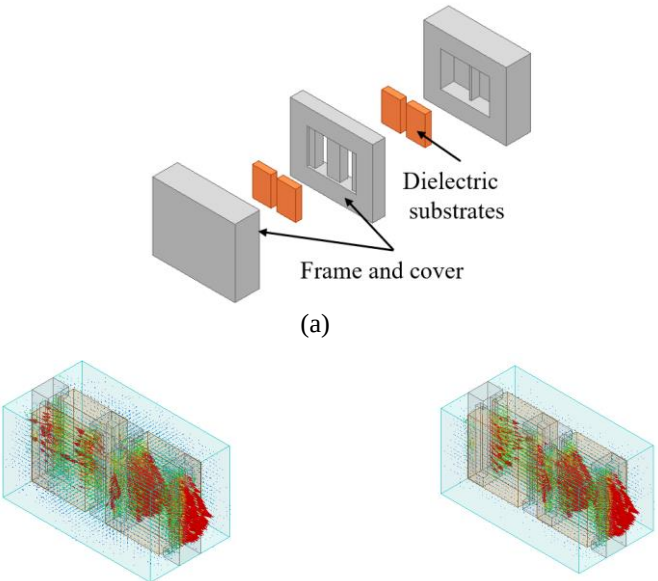

(a)

(a) (b)

Figure 4-7 Electrical field of the coupled resonator in vertical coupling, (a) 3D view of the arrangement of the coupling resonators; (b) first mode; (c) second mode.

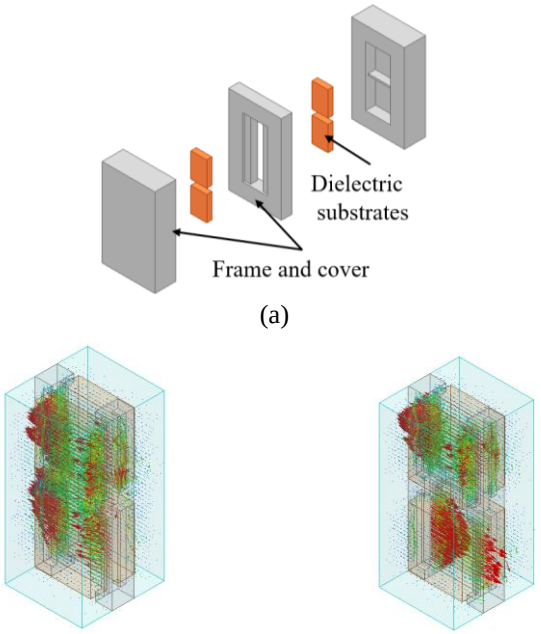

(a)

(b) (c)

Figure 4-8 Electrical field of coupled resonator in vertical coupling: (a) 3D view of coupling resonator arrangement; (b) first mode; (c) second mode.

4.2.4 Advantages of Assembly for the Proposed Structure

Figure 4-9 shows the metal frame of a single resonator with the DSs assembled. The size of the DSs are designed to be slightly smaller so that they will not entirely fill the positioning grooves. The gap shown in Figure 4-9 is designed to be 0.2 mm. A slight shift of the DSs due to misalignment during assembly will not cause a significant shift of the resonant frequency.

Figure 4-10 shows the frequency shift versus misalignment of the DSs in both the y and z directions. This indicates that, with the positioning groove, the resonance frequency shift is small enough to be compensated by tuning. It should be mentioned that such levels of frequency shift due to assembly misalignment are also observed when dealing with conventional dielectric resonator filters.

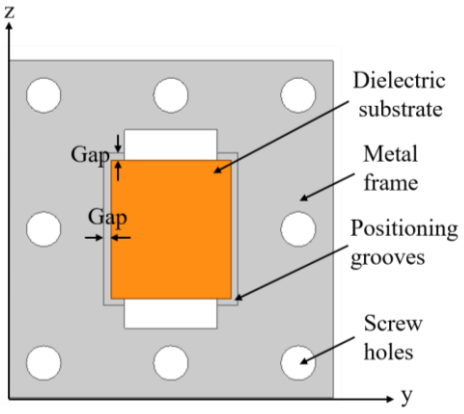

Figure 4-9 Side view of the metal frame when the DS is mounted.

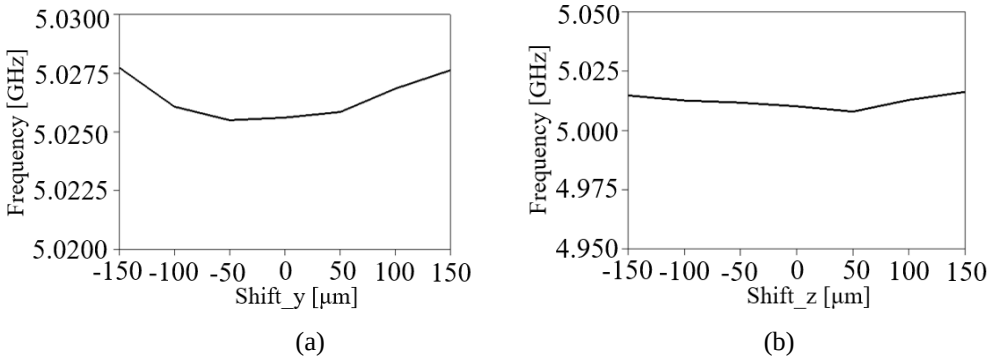

(a) (b)

Figure 4-10 Eigenmode simulation for resonance frequency: (a) resonance frequency versus DS misalignment along y axis (Shift_y); (b) resonance frequency versus DS misalignment along z axis (Shift_z).

4.3 Two-pole Filter with Vertical Coupling

The 3D diagram for the disassembled two-pole filter is shown in Figure 4-11. The filter has two covers, four diced DSs, and one metal frame for holding the DSs. Figure 4-12 shows the fabricated pictures of the two-pole filter). The size of the filter is 24 mm × 17 mm × 14.8 mm excluding the input and output connectors. The DSs are diced from a two-inch square dielectric substrate with thickness of 1.5 mm using a conventional dicing saw as shown in Figure 4-2.

The EM simulation model for the two-pole filter is shown in Figure 4-13. We assign the boundary condition of the air-box to be copper. Figure 4-14 shows the measured results versus EM simulation results Measurement results show the center frequency of the filter is 5.3 GHz with insertion loss of 0.22 dB and bandwidth of 190 MHz at 25 dB return loss. This give a quality factor of 445 for the two-pole filter.

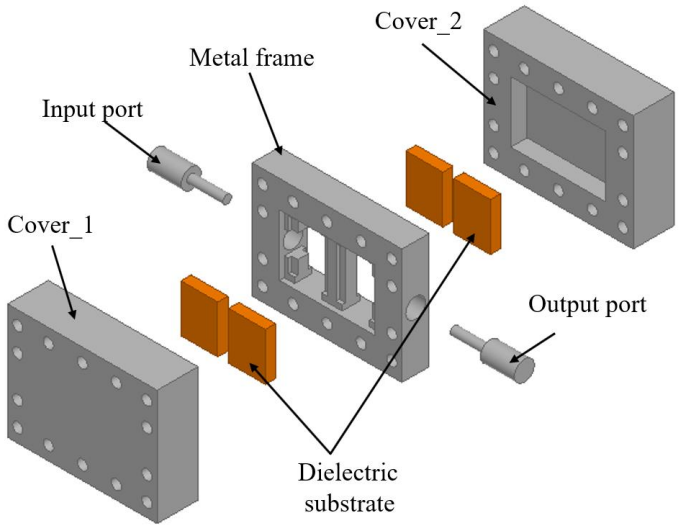

Figure 4-11 3D diagram of the two-pole filter.

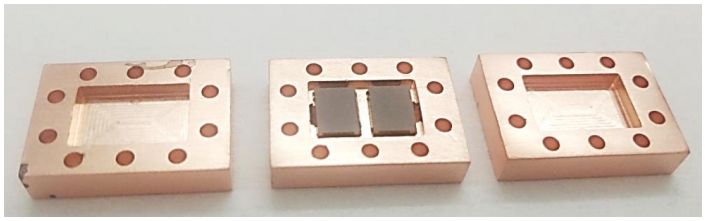

(a)

(b)

Figure 4-12 Picture of the fabricated two-pole filter, (a) disassembled filter; (b) assembled filter.

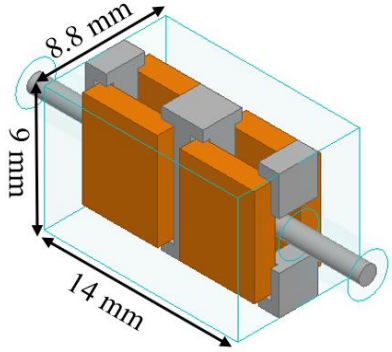

Figure 4-13 EM simulation model for the two-pole filter.

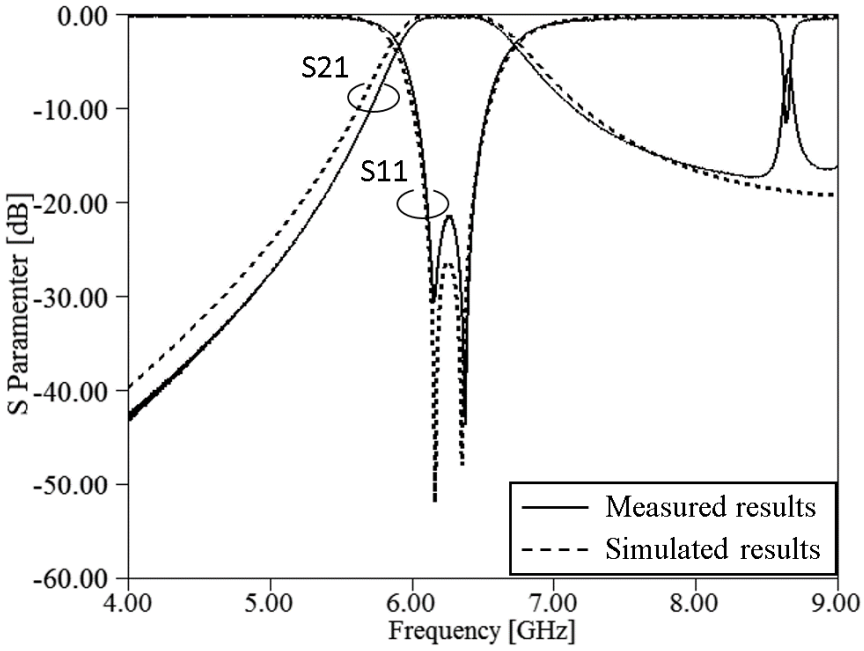

Figure 4-14 Simulation and measurement results of two-pole filter with larger span.

4.4 Five-pole Filter with Parallel Coupling

A 3D diagram of a five-pole filter is shown in Figure 4-15. The filter consists of two covers, ten diced DSs, and one metal frame for holding the DSs. Coupling irises are designed on the covers for controlling the inter-resonator couplings. Although all DSs have the same width, the heights are slightly changed to account for iris loading.

Figure 4-16 shows the fabricated pictures of the five-pole filter. The size of the filter is 53 mm × 17 mm × 14 mm, excluding the input and output ports.

The EM simulation model for the five-pole filter is illustrated in Figure 4-17, while Figure 4-18 depicts the EM simulation results and measurement results for the filter. The measurement results indicate that the center frequency of the filter is 5 GHz, with an insertion loss of 0.6 dB and a bandwidth of 480 MHz at a 20-dB return loss. This give a *Q*-factor of 449 for the five-pole filter.

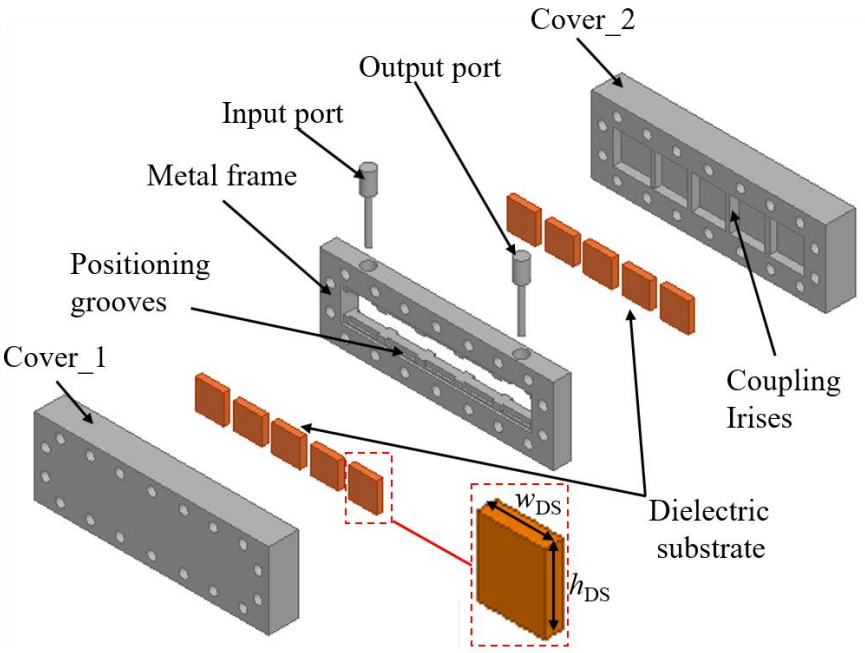

Figure 4-15 3D diagram of five-pole filter.

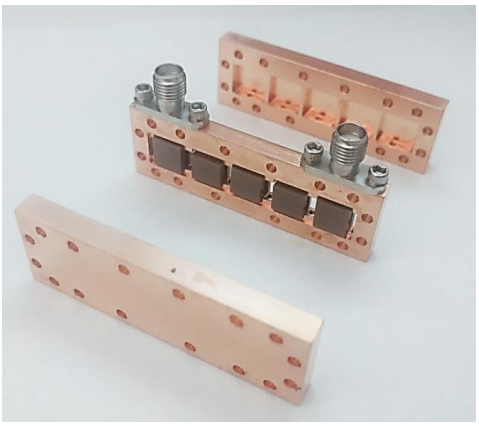

(a)

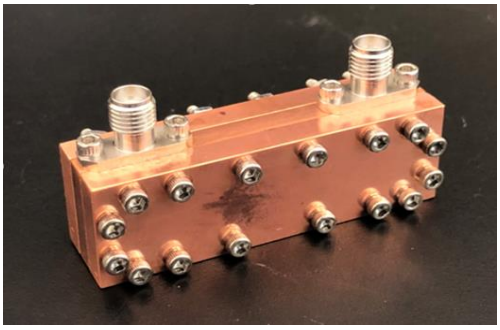

(b)

Figure 4-16 Picture of fabricated five-pole filter: (a) disassembled filter and (b) assembled filter (total size 17 mm × 14 mm × 53 mm).

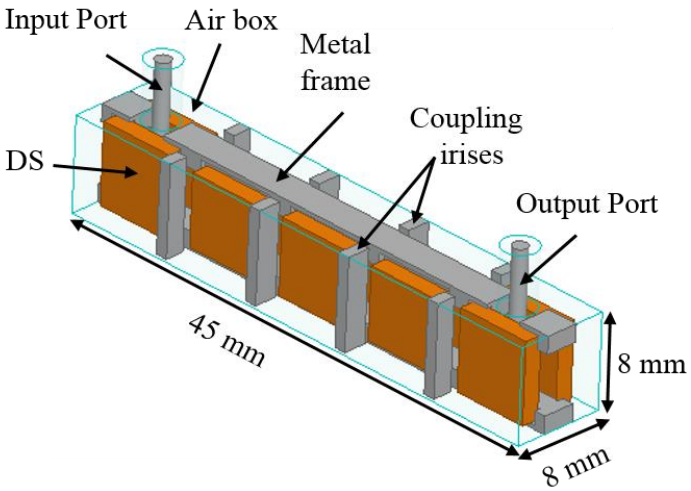

Figure 4-17 EM simulation model for five-pole filter.

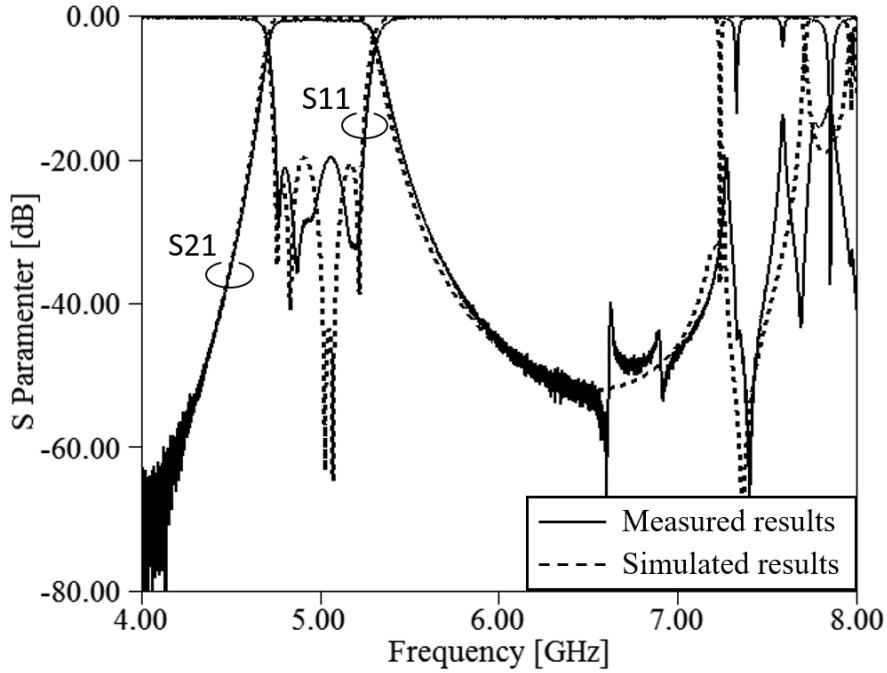

Figure 4-18 Simulation and measurement results of five-pole filter with larger span.

4.5 Four-pole Filter with Transmission Zeros

A 3D diagram of a four-pole filter is shown in Figure 4-19. The filter uses eight diced DSs and two Teflon blocks with copper rods to provide negative coupling. Coupling irises are designed on both the cover and the metal frame for controlling inter-resonator coupling. The rods for realizing negative coupling are first inserted into the Teflon blocks and then placed in the grooves on the covers.

Figure 4-20 shows the pictures of the fabricated four-pole filter disassembled in (a) and assembled in (b). The size of the filter is 26 mm × 28 mm × 15 mm, excluding the input and output connectors.

The EM simulation model for the four-pole filter is shown in Figure 4-21, while Figure 4-22 illustrates the EM simulation and measurement results for the filter. The measurement results show that the center frequency of the filter is 5 GHz, with an insertion loss of 0.63 dB and a

bandwidth of 450MHz at a 20-dB return loss. The extracted *Q* for the measured results is 310 for this prototype filter unit.

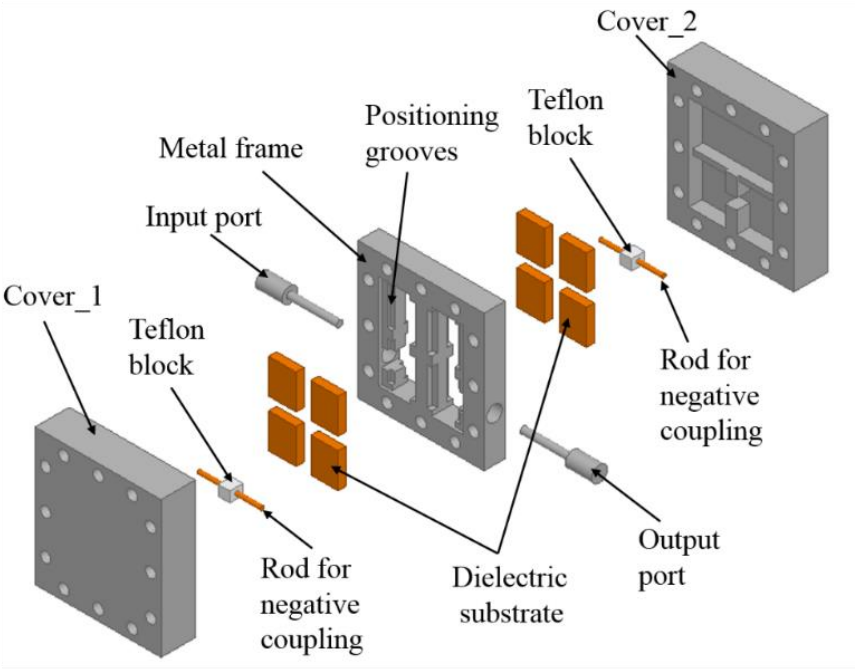

Figure 4-19 3D diagram of four-pole filter.

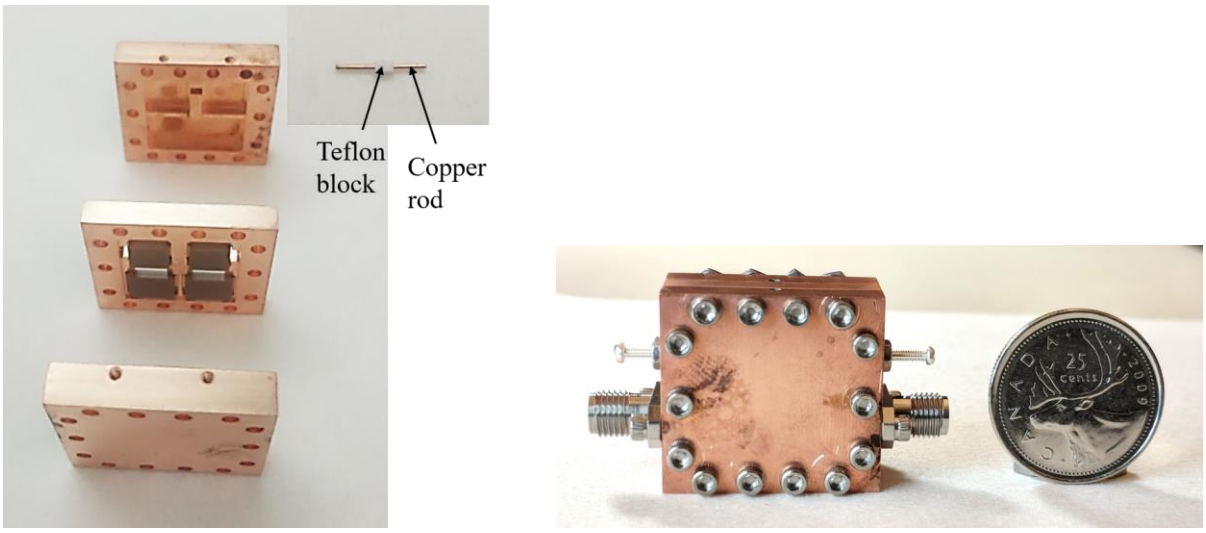

(a) (b)

Figure 4-20 Picture of the fabricated four-pole filter, (a) disassembled filter; (b) assembled filter.

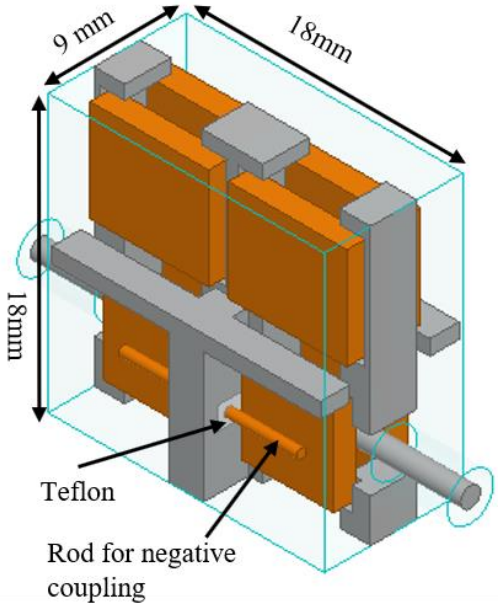

Figure 4-21 EM simulation model for four-pole filter.

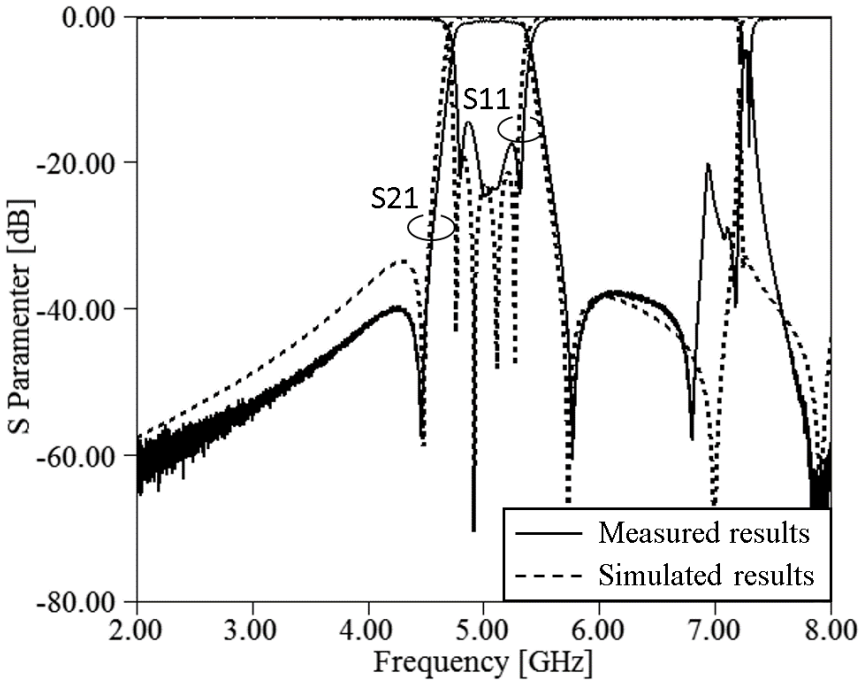

Figure 4-22 Simulation and measurement results of four-pole filter.

4.6 *Q* Improvement with Teflon Holding Structure

4.6.1 Possible Factors that Decreased the *Q* Factor

Silver paste is used in all the above-tested filters to assemble the DSs to the metal frame, which introduces loss to the filter. From Figure 4-3, we can see that the E-field at the interface of the DSs and the metal frame is at the maximum of the resonator. This makes the loss due to the silver paste more significant. We conducted an HFSS simulation, taking the thickness of the silver paste layer between the DSs and the metal frame into consideration. The HFSS model is shown in Figure 4-23. The silver pastes we use are from SPI supplies and have specified conductivity, which may vary from about 400,000 S/m to 3,000,000 S/m [108].

Figure 4-24 shows the simulation results of *Q* with different thicknesses of the silver paste layer. In the simulation, we chose four conductivities between the lowest and highest. From the simulation results, it can be seen that the *Q* of the resonator is above 1000, with the conductivity of the paste higher than 1,500,000 S/m over a paste thickness range of 15 μm to 30 μm. However, when the conductivity of the paste is lower than 750,000 S/m, the simulated *Q* is below 1000 over a paste thickness range of 15 μm to 30 μm. It can also be seen that as the thickness of the paste increases, the *Q* decreases. Approximately 10% of the *Q* decrease is shown in the simulated results when the thickness of the paste increases from 15 μm to 30 μm. Since it is difficult to control the amount of adhesive during assembly, an alternative mounting structure is proposed.

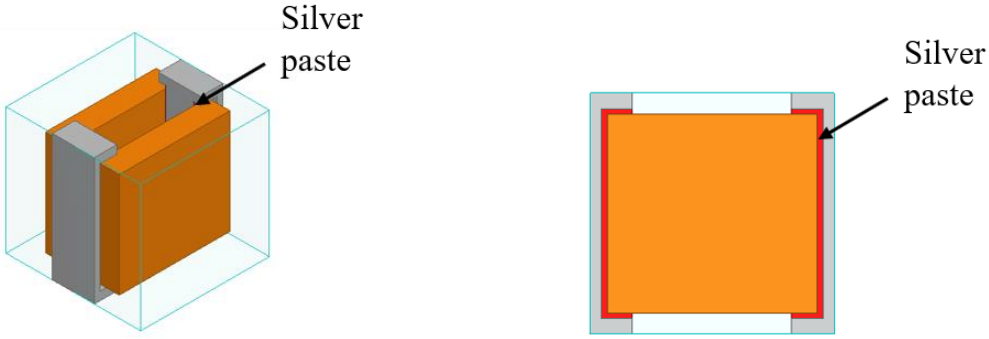

(a) (b)

Figure 4-23 EM simulation model with silver paste, (a) 3D view; (b) front view.

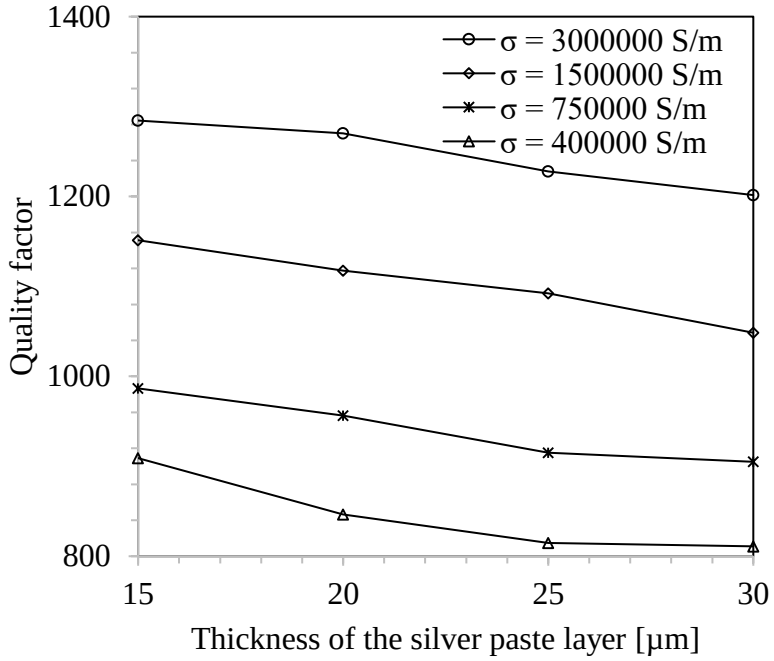

Figure 4-24. *Q* versus thickness of silver paste layer with EM simulation.

4.6.2 Teflon Holding Structure for Resonator and a Three-pole Filter

A Teflon holding structure is designed for improving the *Q* by avoiding the use of paste for mounting the DSs on the middle frame. Figure 4-25 is the simulation model of a resonator with the new assembly structure. Figure 4-26 shows the image of the fabricated resonator. As can be seen, the DSs are mounted on the middle frame with Teflon holder pieces designed with grooves to hold the DSs. These are attached to the metal frame with Teflon screws.

Figure 4-27 illustrates the simulated return loss for the resonator with the Teflon holding structure in Figure 4-25. The extracted unloaded *Q* from the simulation for the resonator is 2300. Figure 4-28 shows that the measured results for the extracted unloaded *Q* is 1760. This indicates that a significant *Q* improvement is achieved by using the Teflon holding structure for the proposed resonator. It should be mentioned that deviation from theoretical results in the unloaded *Q* value could be attributed to the dielectric loss tangent of 0.00012 which is assumed in the

simulation. Such loss tangent was based on supplier data and has not been verified experimentally.

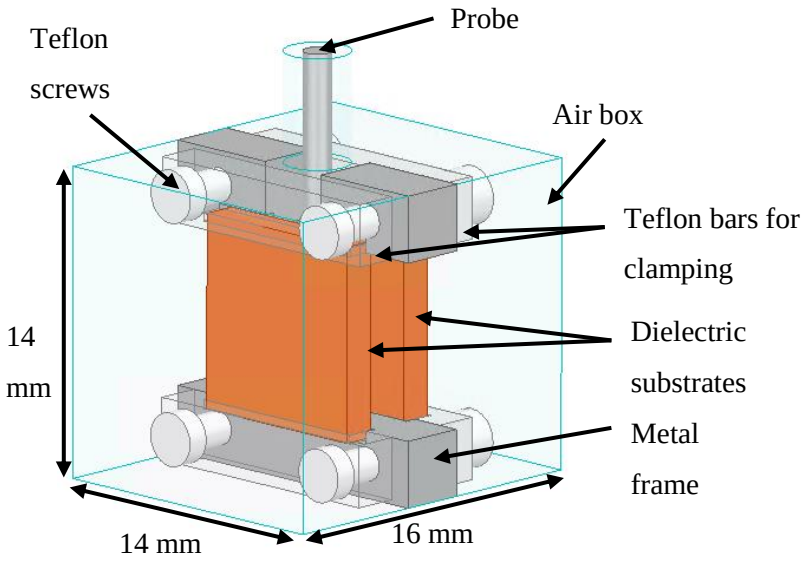

Figure 4-25. EM simulation model for a resonator.

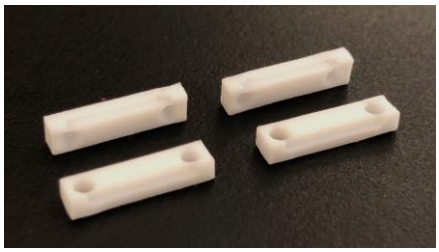

(a)

(b)

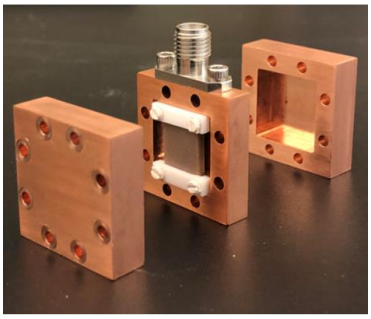

(c)

Figure 4-26. Image of the resonator with the Teflon support. (a)the Teflon support; (b) DS mounted on middle frame with Teflon holding structure and Teflon screw; (c) disassembled resonator.

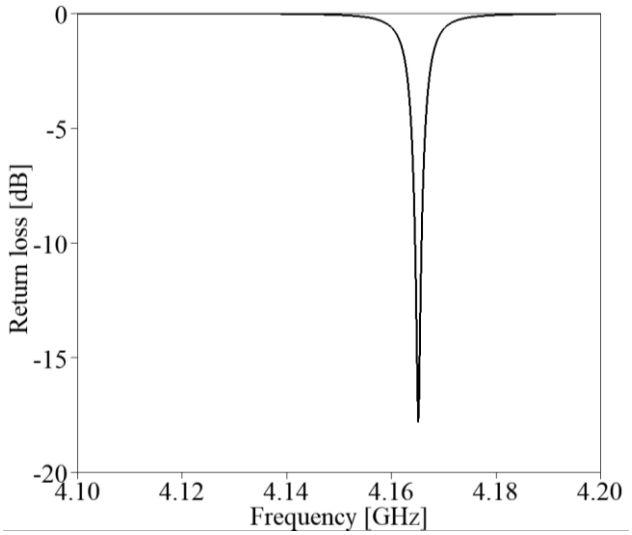

Figure 4-27 Simulated return loss for the resonator.

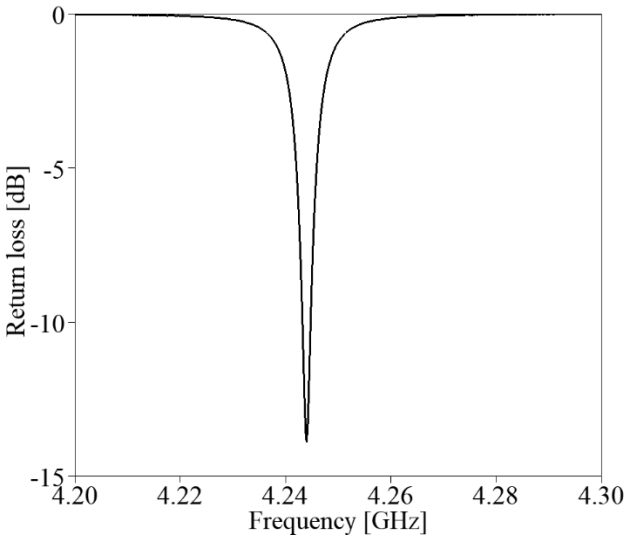

Figure 4-28 Measured results for the resonator: (with Teflon holding structures.

A three-pole filter with a Teflon holding structure is designed and fabricated. The DSs used for this design have the dimension of 8.4 mm × 6.8 mm × 1.5 mm. These resonators are slightly larger than those used for designing the 5 GHz filters in Figure 4-15 and Figure 4-19.

Figure 5-28 (a) illustrates the EM simulation model for the three-pole filter, while Figure 4-29 (b) shows the fabricated filter. The filter contains six DSs, which are assembled using Teflon holders and screws. The two covers and the middle frame are then bolted together.

Figure 4-30 illustrates the EM simulation and measurement results of the three-pole filter with Teflon holding structure. The measurement results show that the filter exhibits an insertion loss of 0.14 dB and a bandwidth of 560 MHz at 20 dB return loss. The extracted loaded *Q* of this filter is 810. For comparison purposes, Figure 4-31 illustrates the measured results for a three-pole filter with DSs assembled using silver paste. The center frequency is 3.9 GHz, the insertion loss is 0.39 dB, and the *Q* is 230. As can be clearly seen, the *Q* has been significantly improved with the use of a Teflon support rather than silver paste.

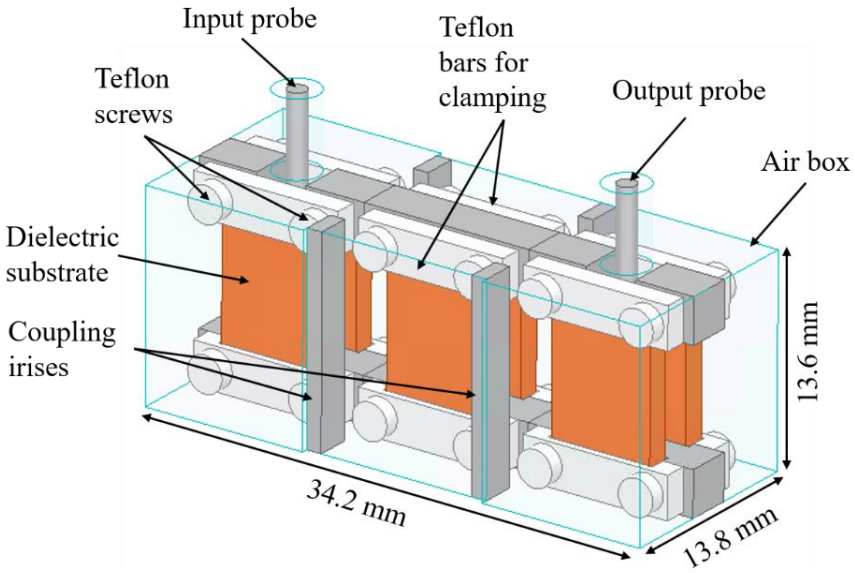

(a)

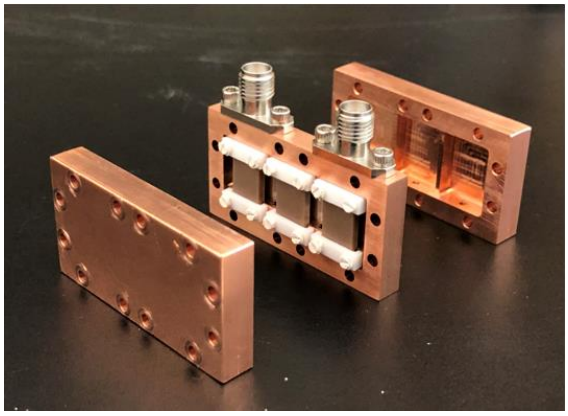

(b)

Figure 4-29 Three-pole filter: (a) EM simulation Model, (b) fabricated filter.

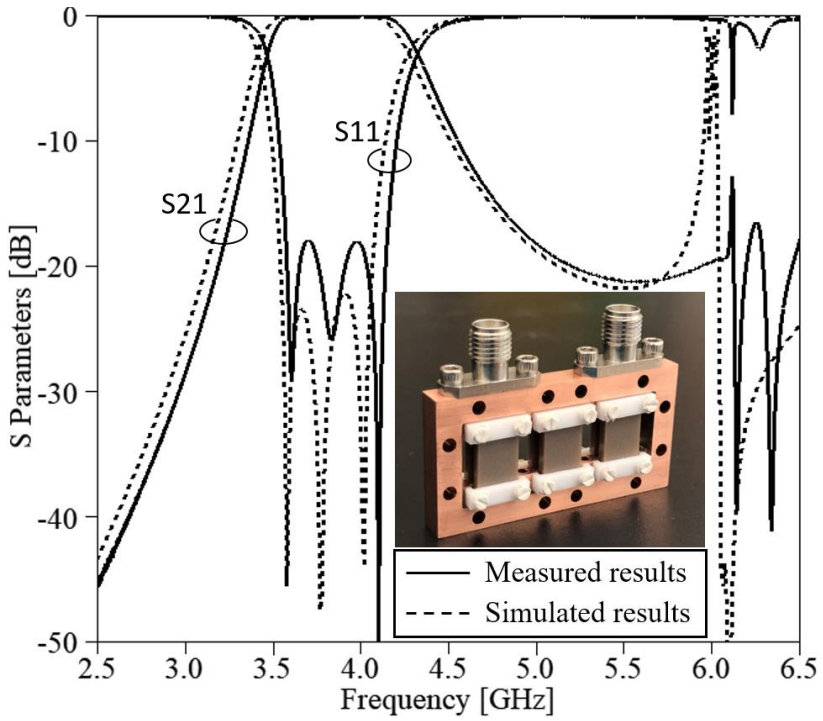

Figure 4-30 Simulation and measurement results of the three-pole filter with Teflon holding structure.

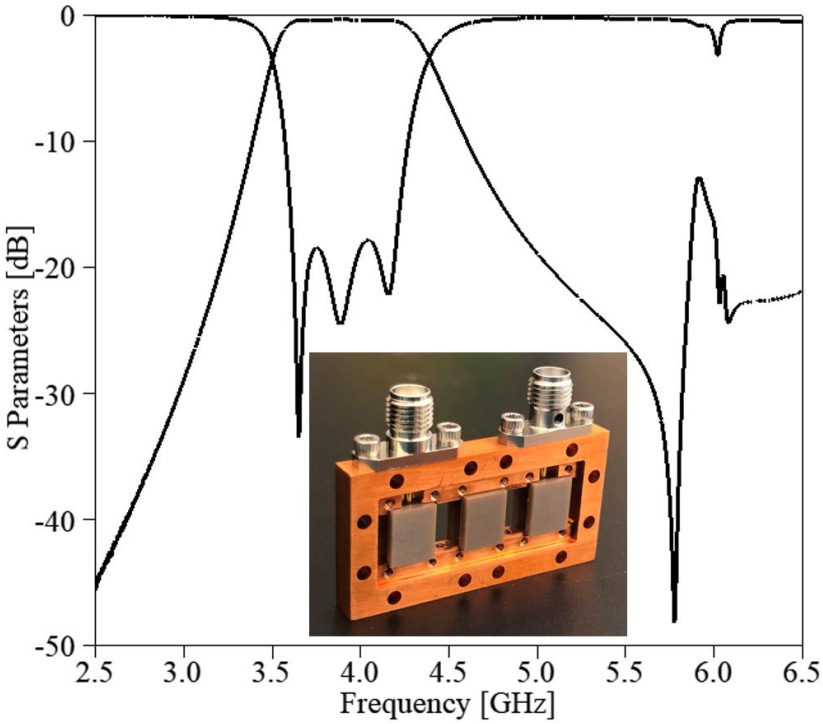

Figure 4-31 Measurement results of the three-pole filter with silver paste.

4.7 Discussion

Table 4-2 shows a comparison of our proposed filters with some compact DR/DS-loaded filters reported in the literature. Reference [96], [102], and [103] use cylinder dielectric-loaded resonators with TM mode. Although these resonators are compact in size, they can only realize small fractional bandwidth. Reference [105] employs triple-mode to realize compact filter with a machined cylinder dielectric resonator, resulting in a relatively higher fractional bandwidth of 3.2%. However, it requires extensive machining of the dielectric resonators, which adds to cost. In [109], DR TM mode is used to realize a larger fractional bandwidth of 4.95%. However, the dielectric material used in the filter has a complex shape and requires additive manufacturing technology (stereolithography). Furthermore, all the above-mentioned references utilize bulky high-K dielectric material, which is hard to realize in low-profile filters.

In [104], the researchers employed a dielectric substrate, but it uses the TEH mode of dielectric resonator mode and is only feasible for narrow bandwidth applications. Also, the size is quite large compared to the proposed design.

Our proposed filter structure employs dielectric substrates that are thin, giving the advantage of realizing low profile filters. The fractional bandwidth of larger than 10% can be easily realized. Also, these dielectric substrates can be easily diced from a larger size substrate using conventional dicing saws or water jet machining.

Table 4-2 VO_2-based RF switches

Ref.	f_0 (GHz)	Filter Order	DR/DS type	FBW (%)	IL (dB)
[96]	2.6	4	Cylinder	1.92	0.35
[102]	4.2	3	Cylinder	1.5	1.3
[103]	1.598	4	cylinder	1.25	0.85
[106]	2.5	6	Machined cylinder	3.2	0.17
[104]	4	4	DS	1.0	0.4
[109]	4.05	4	3D printed cylinder	4.94	0.3
This work	5.0	5	DS	9.6	0.62
This work	5.0	4	DS	9.0	0.63
This work	3.9	3	DS	13	0.14

4.8 Summary

This chapter has presented a novel configuration of dielectric substrate-based cavity filter. The proposed filter structure offers ease of assembly while capable of realizing large bandwidth and exhibits a relatively thin profile. Five-, four- and three-pole prototype DS-loaded filters using the proposed structure were designed, fabricated, and measured. The fractional bandwidth of the five-pole filter is 9.6%, with a spurious located at roughly 1.5 f_0. The three-pole filter realized a fractional bandwidth of 13%. A Teflon-based mounting structure is proposed to improve the *Q*-factor of these types of filter structures. The measurement results of the prototype filter unit presented show a loaded *Q* of 810. The simulation results promise an unloaded *Q*-factor above 1800 at 4 GHz, making it useful in sub-6 GHz miniature, low-cost, wideband applications.

Chapter 5

VO_2-based Tunable Filters

5.1 Introduction

Tunable filters are required in multiband systems and in applications where there are demands to continuously change the filter center frequency to adapt to communication traffic conditions and changes in system environment. One of the main needs of tunable filters is maintaining low insertion loss over the tuning range. The key to achieving this goal is using high-*Q* resonators, such as three-dimensional (3D) structure resonators (e.g., metallic post-resonators [71], dielectric resonators [110] or cavity resonators [111]). For tunable filters, not only should the resonators have high unloaded *Q*, but the tuning elements should also have low loss.

Various tuning techniques have been employed to realize tunable filters, including mechanical tuning, piezoelectric tuning, magnetic tuning, and MEMS tuning. Mechanical tuning is usually bulky and slow, while magnetic tuning requires high power consumption. In typical MEMS switch based-tuning, the MEMS switches are integrated with lumped element capacitors to vary

the capacitive loading on the combline resonator and hence change its resonance frequency [110]. However, such lumped element capacitors are known to degrade the unloaded *Q* of the resonator. Fouladi et al. reported a combline tunable bandpass filter with a center frequency of 2.5 GHz, a bandwidth of 22 MHz, and a quality factor ranging from 1300 to 374 over 110 MHz of tuning range [71]. Park et al. designed a high-*Q* tunable evanescent-mode cavity filter with RF MEMS switch networks featuring a tuning range of 4.07-5.58 GHz. The unloaded *Q* of this filter is 300-500 over the tuning range [111]. A high-*Q* tunable waveguide filter with RF MEMS switched capacitors was realized by Stefanini et al., with an unloaded *Q* factor of 620 to 250 and tuning from 5.2 GHz to 4.4 GHz [112]. Note that all of the above tunable filters employ high-*Q* resonators, and that the bottleneck to realizing a high-*Q* value in these filters is the tuning element.

5.2 Tunable Combline Filters

5.2.1 Design and Simulation Results of Tunable Combline Filters

A tunable structure based on RF switches is proposed to realize multi-state tunable filters. The configuration of the design is shown in Figure 5-1. The tuning structures consist of multiple strip lines integrated with RF switches. This allows the metal strip lines inside the cavity to be either connected or not connected to the ground, which changes the field distribution inside the cavity. As a result, the resonators would see a significant shift in resonant frequencies, while their high-*Q* performance is preserved. This approach can be further expanded by including more strip lines and corresponding switches to achieve a larger number of tuning states.

A two-pole tunable combline filter employing the proposed tuning structure is shown in Figure 5-2. The tunable filter consists of: a) a combline filter, and b) a tuning circuit fabricated on Rogers 5880 PCB integrated with RF switches.

The combline filter consists of two parts: the cover with the resonator posts attached, as shown in Figure 5-2 (a), and the housing in which the tuning structures and SMA probes are installed, as

shown in Figure 5-2 (b). The filter is assembled by flipping the housing over and screwing it to the cover with the resonator posts, thus forming the completed filter structure, as shown in Figure 5-1.

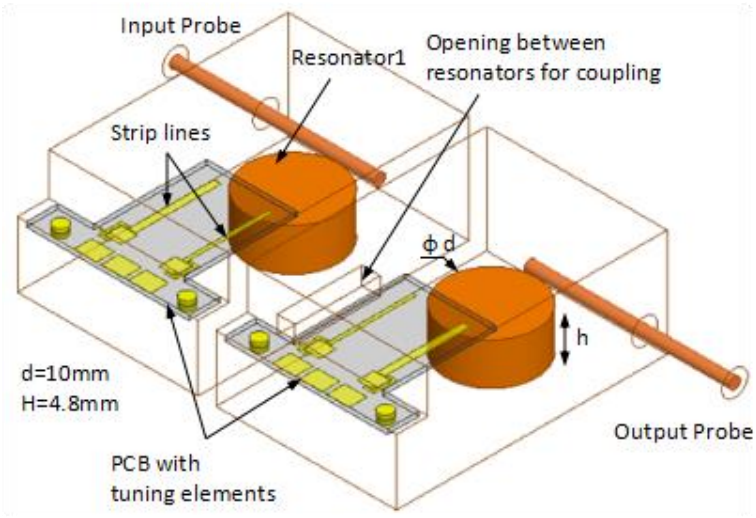

Figure 5-1 Proposed structure for tunable combline filter.

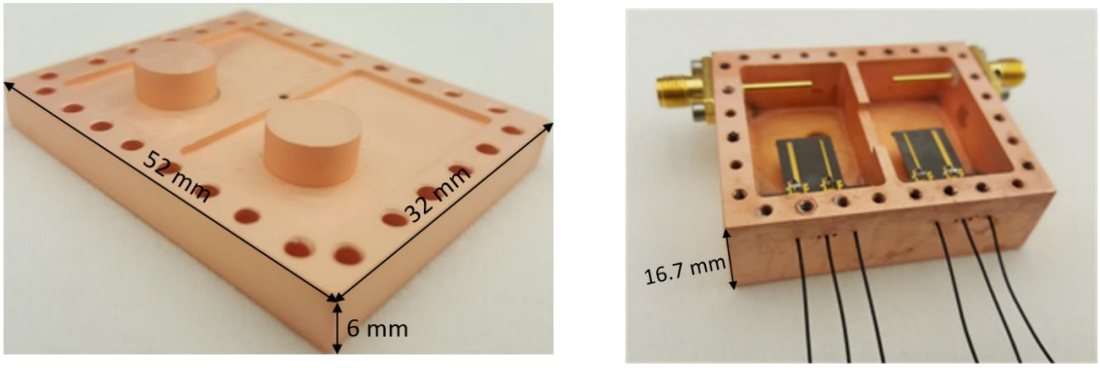

(a) (b)

Figure 5-2 Image of tunable combline filter.

The combline resonators operate in the TEM mode, which has strong electric fields towards the top edge of the resonator, as can be seen in Figure 5-3. Therefore, the opening between resonators for the coupling located at the bottom of the resonator posts depicted in Figure 5-1 would see minimal coupling changes as the resonators are tuned. The HFSS EM simulations show an unloaded *Q* higher than 2500 for all tuning states when a wire bond is used to emulate the switches in the ON-state and a *Q* larger than 1000 when using a RF switch with a switch

resistance of 1.5 Ohm. Details of 2-bit and 4-bit tuning circuits are shown in Figure 5-4. The long strip lines (denoted by Sline 1, 2, 3, and 4) can be connected to ground (ON-state) or disconnected (OFF-state, floating) through either wire bond (for testing purposes) or the use of RF switch connections. As a result, each of the strip lines in the tuning circuit represents two tuning states. A four-strip (4-bit) tuning structure can obtain sixteen discrete states. Ultimately, a close to continuous tuning can be possibly achieved with a sufficiently large number of tuning strip lines.

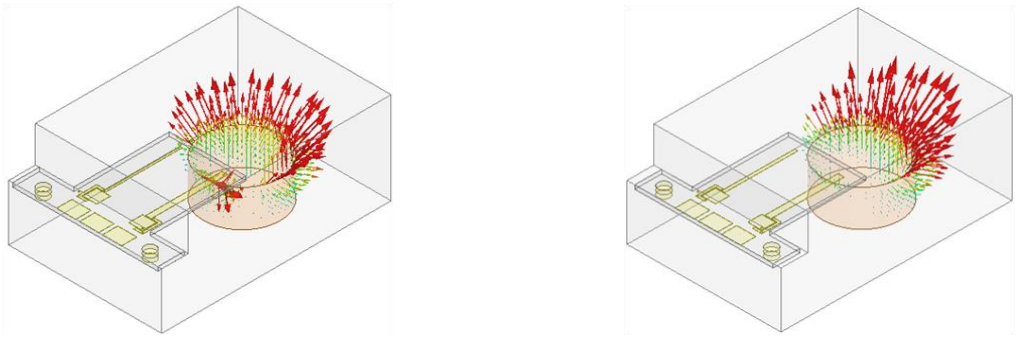

(a) (b)

Figure 5-3. Electrical field of resonator for different states: (a) state 1 with both strip lines not connected to the ground, (b) state 3 with both strip lines connected to the ground with wire bond.

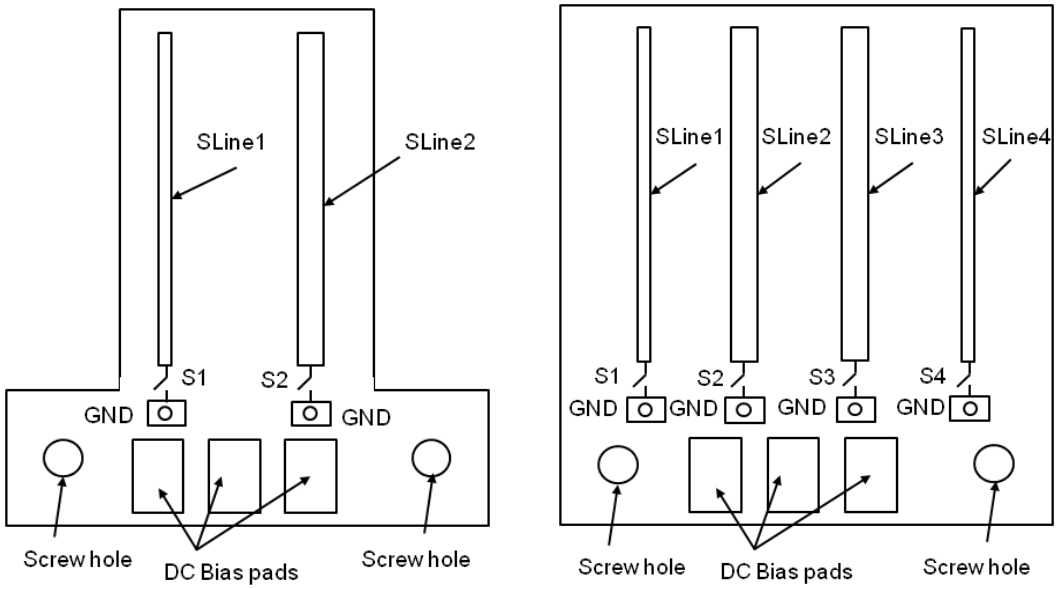

(a) (b)

Figure 5-4 Tuning structure configuration: (a) 2-bit tuning structure (b) 4-bit tuning structure.

A picture of the fabricated PCB for the 4-bit tuning structure is shown in Figure 5-5. Omron MEMS switches are used to connect/disconnect the strip lines to ground. The Omron switches used are SPDT switches, making it possible to control four strip lines with two Omron switches.

Figure 5-6 shows the EM simulation results of a 2-bit structure with wire bond connections emulating ideal MEMS switches. For the three states shown in Figure 5-6, the center frequencies are 7 GHz, 7.14 GHz and 7.23 GHz, respectively, achieving a tuning range of 230 MHz. The corresponding bandwidths recorded at a 10-dB return loss are 97 MHz, 96 MHz and 90 MHz, respectively.

Figure 5-7 shows the EM simulation results of the tunable filter employing a 4-bit tuning structure. The s2p data of the MEMS switches is included in the simulation. For the six states shown in Figure 5-7, the center frequencies are 6.71 GHz, 6.79 GHz, 6.87 GHz, 7.07 GHz, 7.13 GHz and 7.24 GHz, respectively, resulting in a tuning range of 530 MHz. The corresponding bandwidths for each state are 86 MHz, 92 MHz, 96 MHz, 120 MHz, 119 MHz and 118 MHz, respectively. Roger 5880 substrate with a dielectric constant of 2.2 and a loss tangent of 0.0009 is used in order to minimize the adverse effect of the substrate on the loaded *Q* factor.

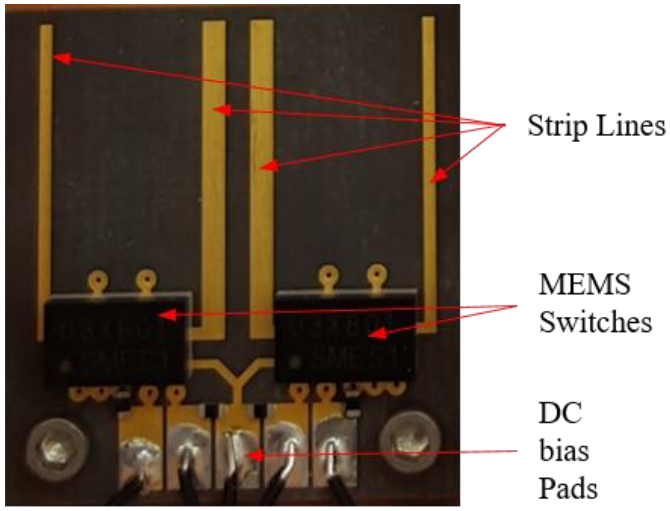

Figure 5-5 PCB of 4-bit tuning structure with Omron MEMS switches, 18mm x 18mm in size.

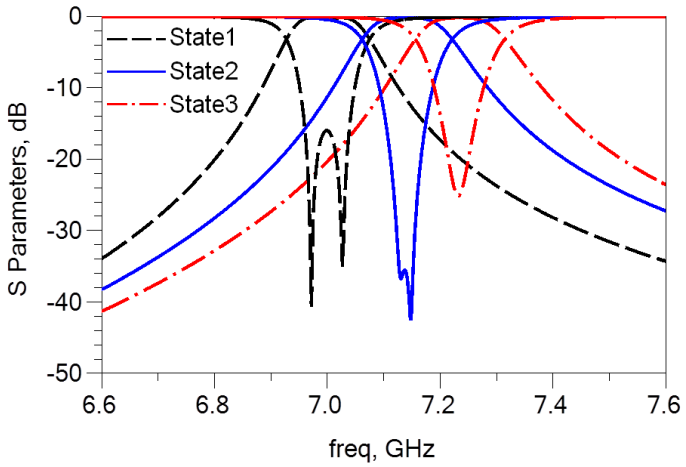

Figure 5-6 Simulation results for 2-bit tuning structure with wire bond connection.

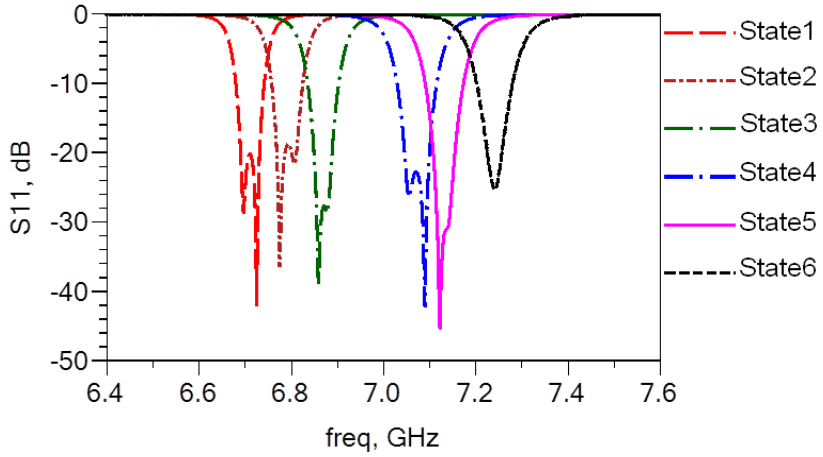

(a)

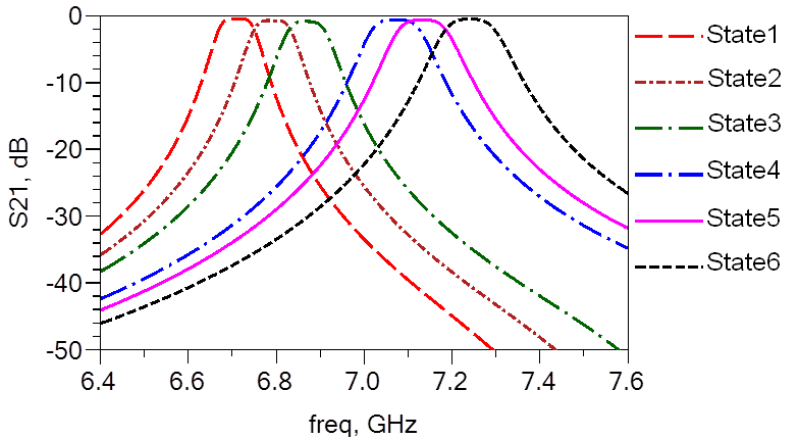

(b)

Figure 5-7 EM simulation results for 4-bit tuning structure with MEMS switches.

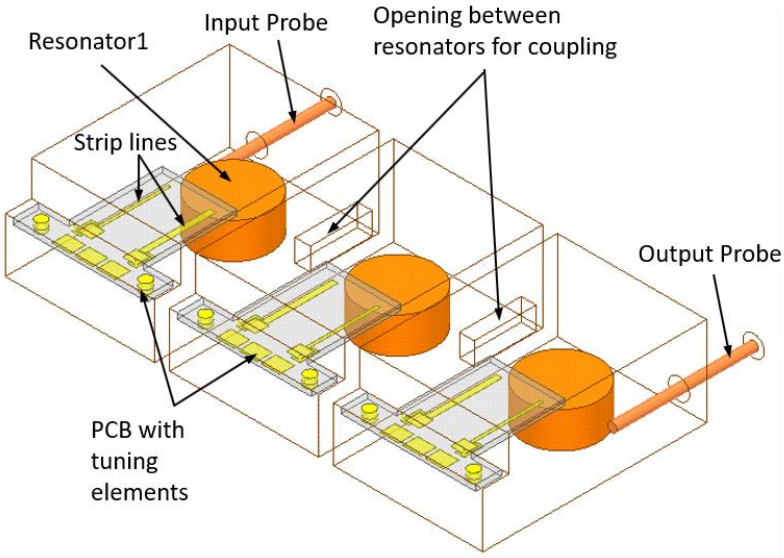

Figure 5-8 EM simulation model for three-pole tunable filter.

A three-pole tunable combline filter is designed. The configuration of the design is shown in Figure 5-8. Whereas Figure 5-9 shows the image of the fabricated filter.

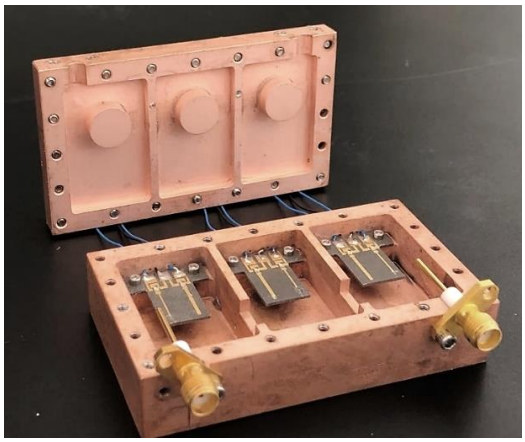

Figure 5-9 Image of three-pole combline filter.

Figure 5-10 shows the simulated results for the three-pole filter. The center frequency, insertion loss, and bandwidth are listed in Table 5-1. The simulated results show a tuning range of 240 MHz from 4.78 GHz to 5.02 GHz. The filter demonstrates almost a constant bandwidth from 46 MHz to 47 MHz at a 20-dB return loss, with the insertion loss varying from 1.390 dB to 1.412 dB.

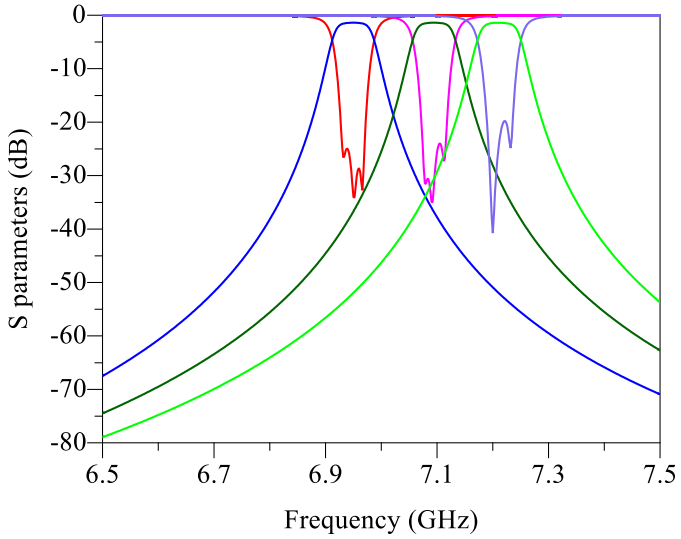

Figure 5-10 Simulation results for three-pole filter with wire bond connection.

Table 5-1 Simulation results for three-pole combline filter
(with R_s assigned to 1 Ω ON-state and 20 kΩ OFF-state)

State	Frequency (GHz)	Bandwidth	Insertion Loss (dB)
1	6.95	46 MHz @ 20 dB return loss	1.390
2	7.09	46 MHz @ 20 dB return loss	1.392
3	7.21	47 MHz @ 20 dB return loss	1.412

5.2.2 Measurement Results with Wire Bonding

Figure 5-11 shows the measurement results for a 2-bit tuning structure utilizing wire bond connections in order to determine the achievable insertion loss if an ideal switch is used. The center frequency, insertion loss, and bandwidth at 15 dB return loss are listed in Table 5-2. The measured results are in close agreement with the simulation, with a slightly smaller bandwidth. The bandwidth remains approximately constant throughout the tuning range of 160 MHz. The unloaded *Q* measured is higher than 2000 for all three states.

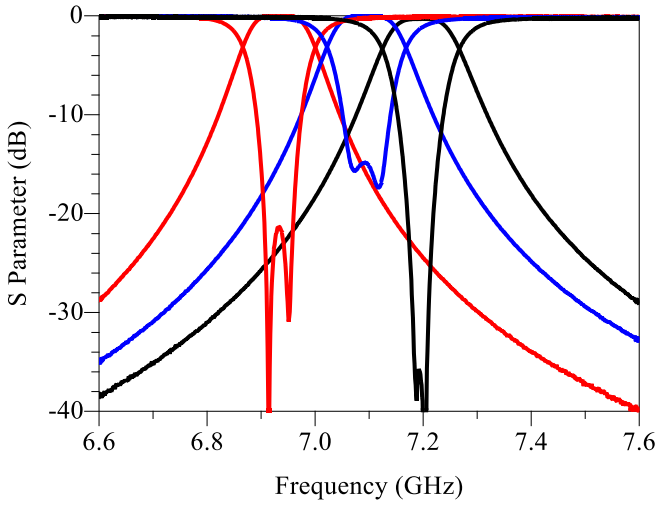

Figure 5-11 Measured results for 2-bit tuning structure with wire bond connections.

Table 5-2 Measurement results for 2-Bit tuning structure

State	f_0 (GHz)	Insertion loss (dB)	BW @ 15dB return loss (MHz)	Unloaded *Q*
1	6.933	0.24	66	3850
2	7.094	0.44	62	2320
3	7.195	0.32	63	3160

The measured S parameters of the three-pole combline filter with wire bond connections are shown in Figure 5-12. The center frequency, insertion loss, and bandwidth at 20 dB return loss are listed in Table 5-3. The bandwidth is between 50 MHz and 55 MHz, while the unloaded *Q* measurements vary from 1300 to 1700.

Figure 5-13 illustrates the measured results of the three-pole tunable filter with a large frequency span. It demonstrates a 1.8-GHz spurious free window for state 1 and a 2-GHz spurious free window for the other two states.

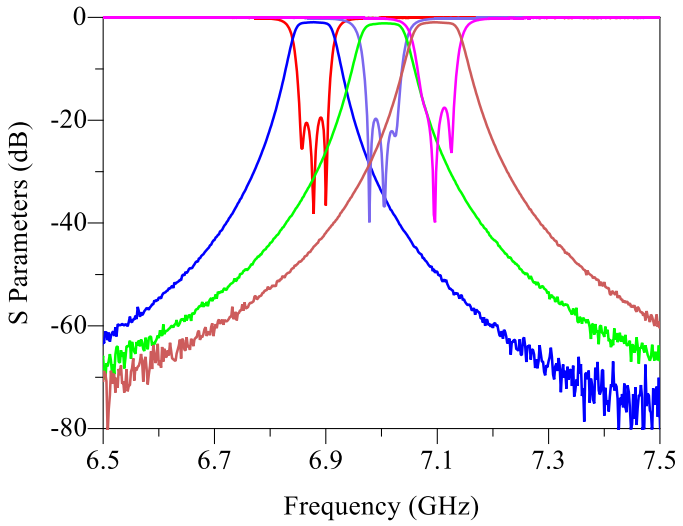

Figure 5-12 Measured results with wire bonding.

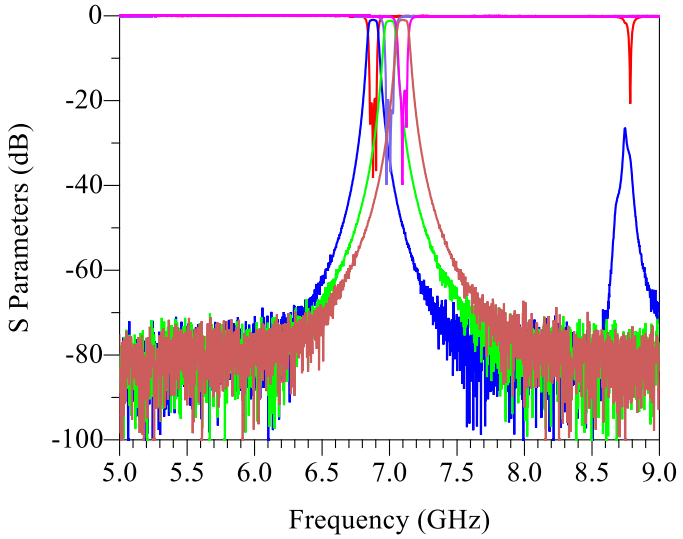

Figure 5-13 Measured results with wire bonding large span.

Table 5-3 Measurement results for three-pole combline filter with wire-bonding

State	Frequency (GHz)	Bandwidth	Insertion loss (dB)	Quality factor
1. No wire	6.88	50 MHz @ 20 dB return loss	0.94	1700
2. Wire for narrow beam ON	7.075	55 MHz @ 20 dB return loss	1.16	1300
3. Both wires ON	7.150	55 MHz @ 20 dB return loss	0.98	1500

5.2.3 Measurement Results with MEMS Switches

The measurement results for the 4-bit tuning structure with Omron RF MEMS switches are shown in Figure 5-14 and Figure 5-15. The insertion loss is relatively high due to the loss of the MEMS switch and other imperfections in the filter assembly. The contact resistance of the Omron MEMS switch is assumed to be 1.5 Ω in the simulation, while in measurement the contact resistance of the integrated OMRON switch appears to be much larger than 1.5 Ω. In addition, the package of the MEMS switch is of size 2 mm x 5 mm, which introduces additional loadings and losses to the resonators. In order to improve the loss performance, RF MEMS switches with a much smaller package size need to be used.

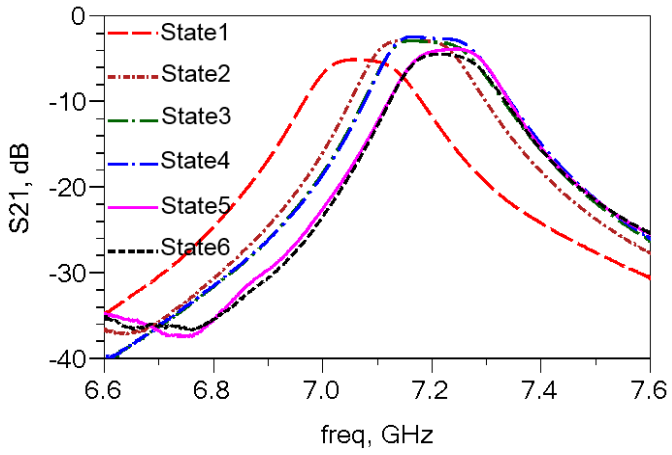

Figure 5-14 Measured insertion loss for 4-bit tuning structure using MEMS switches.

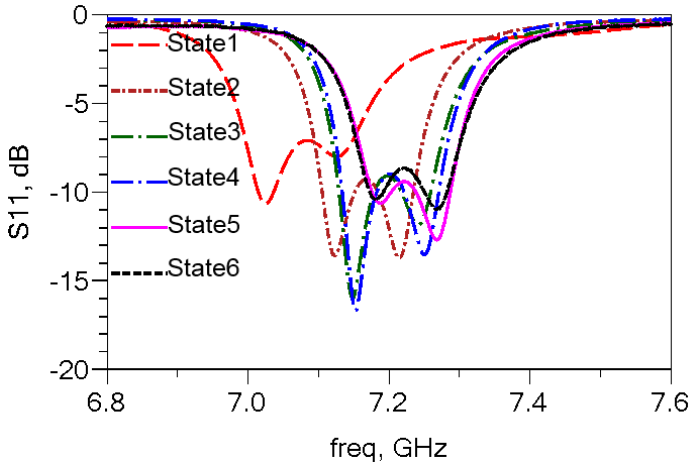

Figure 5-15 Measured return loss for 4-bit tuning structure using MEMS switches.

5.2.4 Measurement Results with VO_2 Switches

A six-layer micro-fabrication process is particularly developed to allow ease of integration with the tuning PCB circuit. Figure 5-16 shows the gold-based six-layer VO_2 fabrication process used for realizing the switches. A 200-nm thin-fim VO_2 is first deposited with RF reactive sputtering and patterned with wet etch. A 350-nm gold layer is then deposited with E-beam evaporation and patterned with lift-off. Next, a 500-nm SiNx layer is deposited with PECVD and patterned with RIE. After that, a 100-nm Cr layer is deposited with E-beam evaporation and patterned with lift-off. A 200-nm SiO_2 layer is then deposited with PECVD and patterned with RIE. Lastly, a 2-um gold two layer is realized with electro-plating and lift-off.

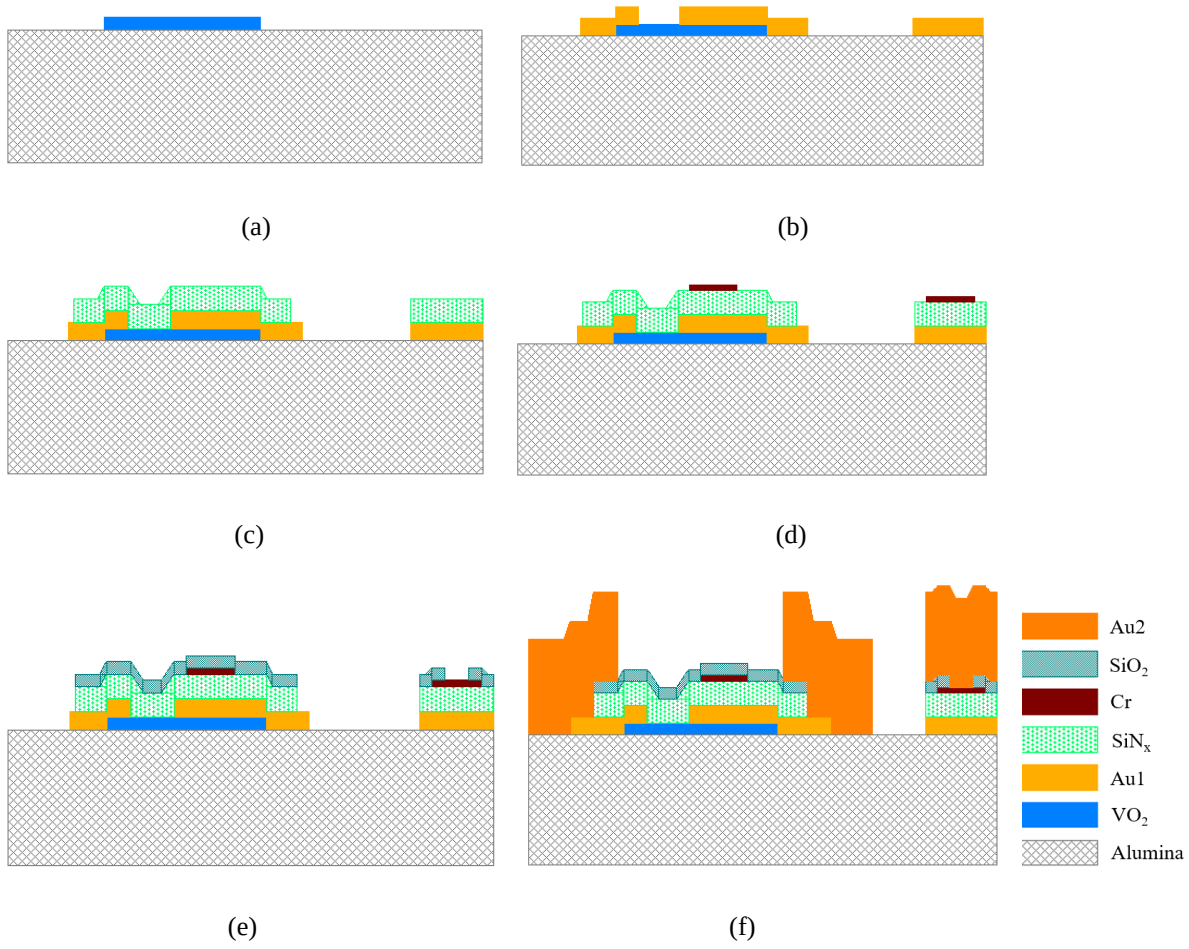

Figure 5-16 Six-layer fabrication process for VO_2.

Figure 5-17 shows the mask of the six-layer fabrication process, while Figure 5-18 shows the fabricated switch for the tunable filters. The switch consists of two RF pads and two DC pads. The RF_out pad in Figure 5-18 will be connected to the RF ground of the tunable filter that will be presented in later sections. The two DC pads are used for applying a DC bias on the micro-heater, which is realized with the Cr layer.

As can be seen from the fabricated picture, the micro-heater is not designed on top of the gap, which differentiates it from the series switches designed in Chapter 3. In the new six-layer process presented in this chapter, the VO_2 layer is deposited as the first layer. The advantage of this approach is that it will be much easier to realize thin-film VO_2 with a good ON-to-OFF-state resistivity ratio, due to the grid shape of the alumina being similar to that of thin-film VO_2. The disadvantage is that if the micro-heater is designed over the gap, there will be a step coverage problem with the thin heater layer. With the heater on one side of the switch, the problem of step coverage is solved; it will also reduce the OFF-state capacitor C_{off}. Figure 5-19 shows the hysteresis curve of the sputtered thin-film VO_2. The sheet resistance of the thin-film VO_2 is from 22.5 kΩ/□ to 14 Ω/□, which represents a resistivity ratio of greater than three orders of magnitude.

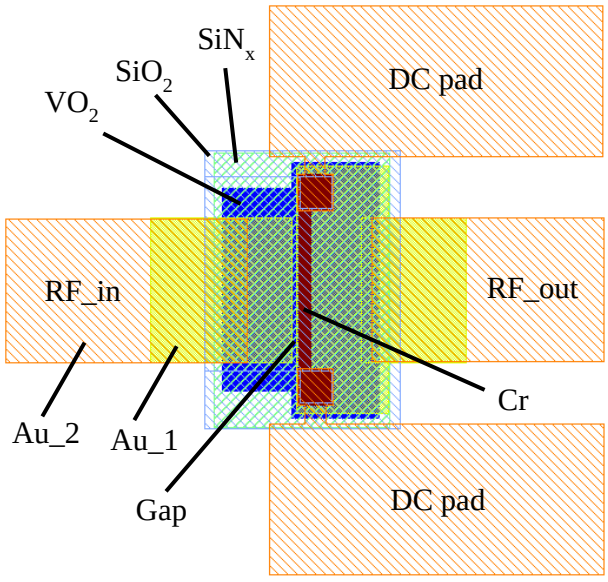

Figure 5-17 Mask of six-layer process.

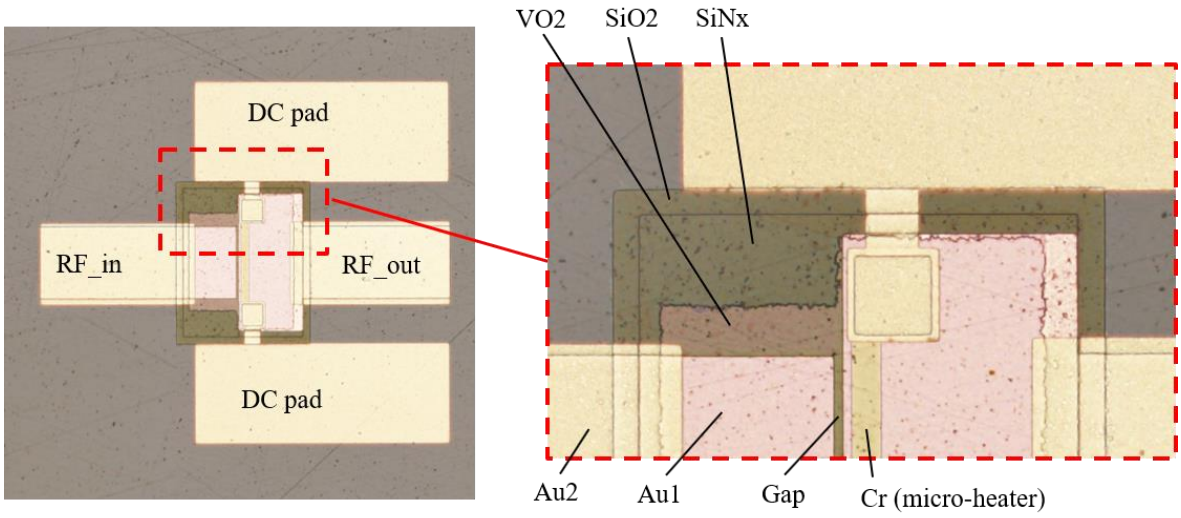

Figure 5-18 Picture of fabricated VO_2 switch for tunable filters.

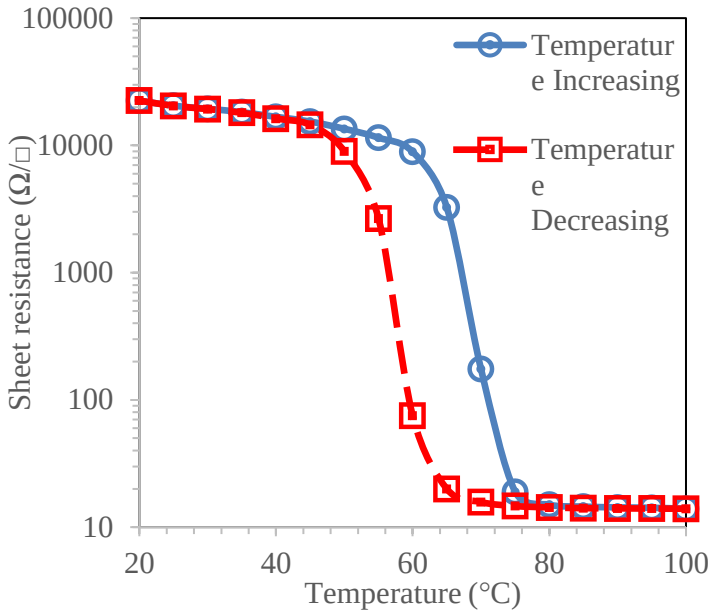

Figure 5-19 Hysteresis curve of thin-film VO_2.

Figure 5-20 shows the assembly of the VO_2-based switched two-pole tunable combline filter. The VO_2 switches are first mounted on the PCB with silver epoxy, after which the RF and DC pads on the VO_2 Switches are connected to the PCB with wire-bonding. Then the PCB with VO_2 switches are assembled on the housing cavity.

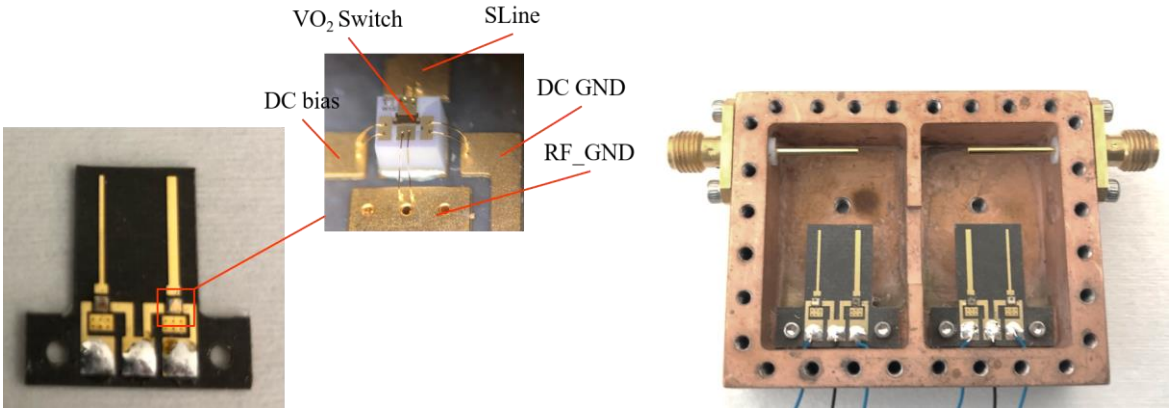

(a) (b)

Figure 5-20 Image of two-pole tunable filter assembled with VO_2 switches.

Figure 5-21 shows the measurement results for a two-pole tunable filter utilizing VO_2 switches. The center frequency, insertion loss, bandwidth at 15 dB return loss, and quality factor are listed in Table 5-4. At state 1, when all switches are OFF, the filter has a center frequency of 6.935 GHz and a quality factor of nearly 500. When all the switches are ON, the center frequency tunes to 7.150 GHz and the *Q* is 600. The tuning range is 215 MHz.

Figure 5-22 illustrates the measured results of the two-pole tunable filter with VO_2 switches in a large span. It demonstrates a 1.9-GHz spurious free window for state 1 and > 2 GHz spurious free window for the other two states.

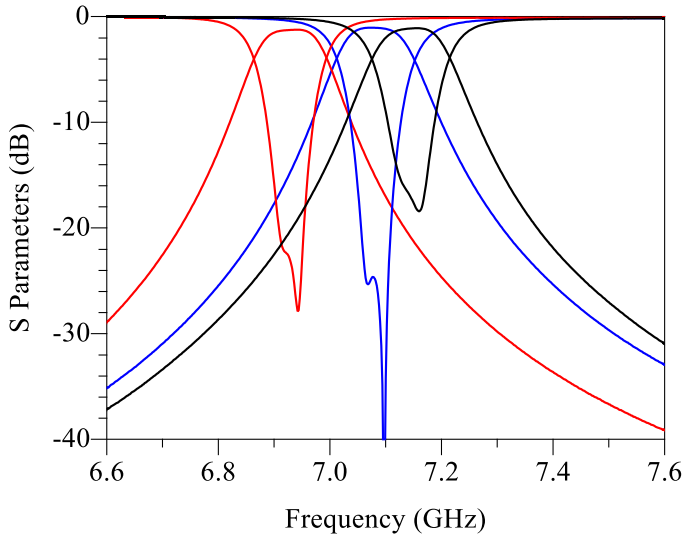

Figure 5-21 Measured results for two-pole combline filter with VO_2 switches.

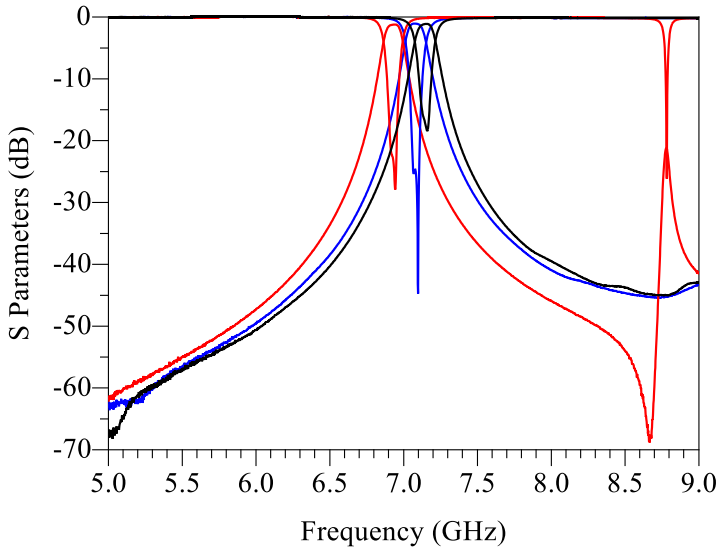

Figure 5-22 Measured results for two-pole combline filter with VO_2 switches with large span.

Table 5-4 Measurement results for two-pole combline filter with VO_2 switches

State	Center frequency (GHz)	BW @ 15dB return loss (MHz)	Insertion loss (dB)
All switches OFF	6.935	62	1.252
All switches ON	7.150	50	1.117

5.2.5 Insertion Loss Discussion

Insertion losses for the designed combline filters are highly related to the series resistance (R_s) of the VO_2 switch at both the ON and OFF states. EM simulations are done using the model shown in Figure 5-1, assigning R_s from 1 Ω to 10 kΩ for switches used in the two-pole filter. Figure 5-24 illustrates the simulated insertion loss, while Figure 5-24 shows the simulated return loss. From the results, we can see that when R_s is smaller than 100 Ω, the filters stay in a high frequency state with a slight frequency shift down and a significantly higher insertion loss as R_s decreases. However, when R_s is larger than 500 Ω, the filter center frequency shifts to a low frequency state with a slight frequency shift down and a lower insertion loss as the R_s decreases. The insertion loss remains low when R_s is smaller than 50 Ω for high-frequency states and larger than 2 kΩ for low-frequency states.

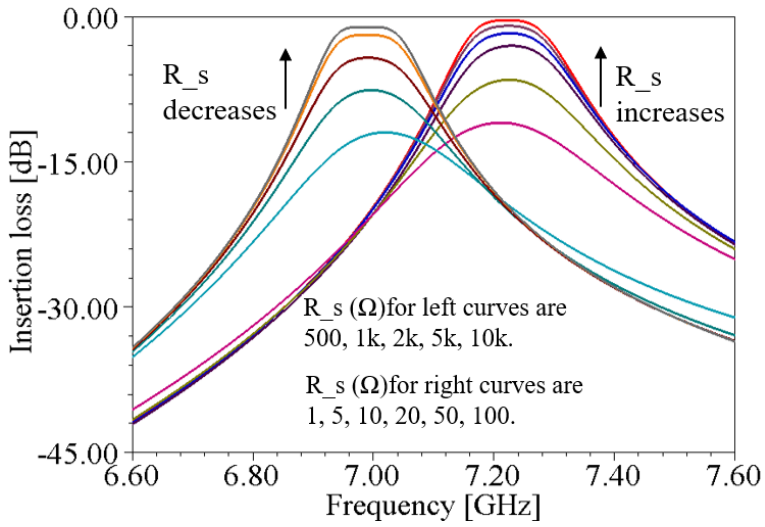

Figure 5-23 Insertion loss when assigning different R_s.

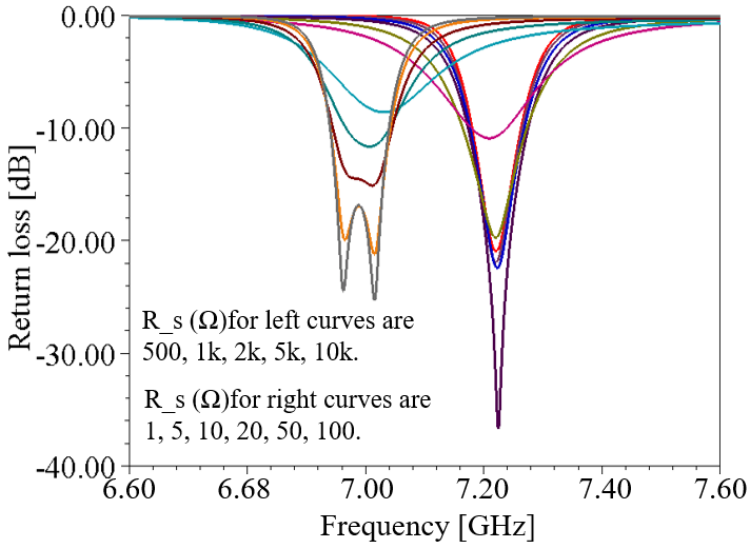

Figure 5-24 Simulation results when assigning different R_s.

Figure 5-25 shows the simulated results with R_s assigned to 2 Ω, 10 Ω, and 50 Ω. Measurement results with different DC voltages applied to the micro-heater of the VO_2 switches are shown in Figure 5-26. The voltages applied to the micro-heater are 5 V, 4.5 V, and 4.2 V, which makes the R_s of the VO_2 switch comparable to 2 Ω, 10 Ω, and 50 Ω. The insertion loss of the measured results matches well the simulated results.

In order to obtain a lower insertion loss for both states, a smaller ON state resistance and a larger OFF state resistance (i.e. a larger ON and OFF resistance ratio) are required for the VO_2 switches, which is determined by the purity of thin-film VO_2 that can be obtained.

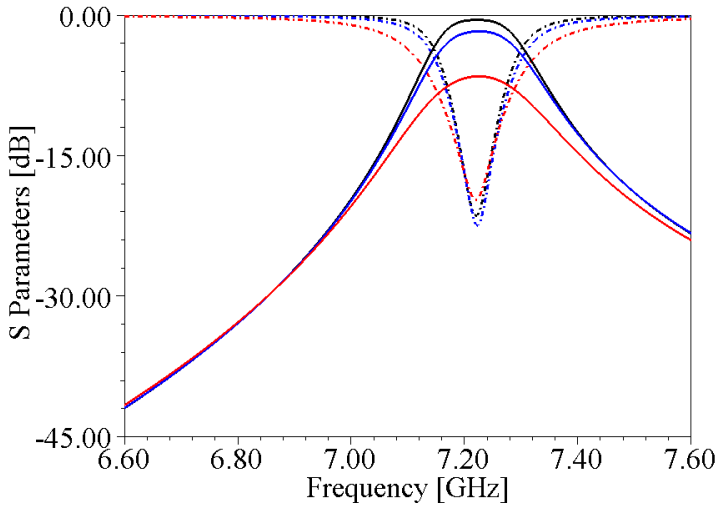

Figure 5-25 Simulated results with R_s assigned to 2 Ω, 10 Ω, and 50 Ω.

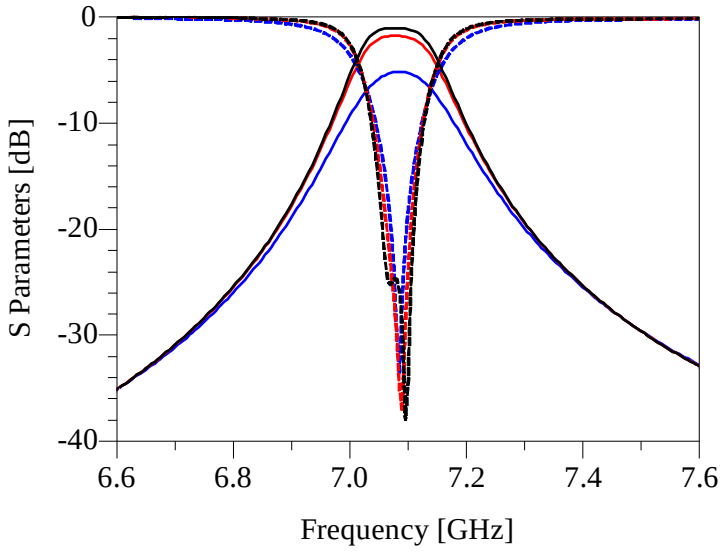

Figure 5-26 Measured results with voltage across micro-heater at 5V, 4.5V and 4.2V.

5.2.6 Power Handling Discussion

It is important to analyze the power handling of the combline filter limited by the power handling of the VO_2 switches. Because these VO_2-based switches can be actuated with high RF power, their OFF-state power handling is mainly related to the RF-self-actuating effect. RF self-actuating signatures were discussed in [41], [84], and [113]. Additionally, [114] reported that when the RF power is high enough in ON-state power handling for VO_2 switches, the thin-film VO_2 shows fracturing, which leads to failure of the switch.

To conduct our analysis, a six-port simulation is done using HFSS. The simulation model is the same as the structure shown in Figure 5-1, but replacing the RF switches with lumped ports, as illustrated in Figure 5-27. The simulated results are then imported into an S6P module in ADS for circuit simulation. Figure 5-28 shows the circuit simulation model. As can be seen, ports 1 and 2 of the S6P module are connected to two 50 Ω terms, while ports 3-6 are connected to an equivalent circuit of the VO_2 switch. Note that the series resistance (R_s) of the equivalent circuit is replaced by a term with a characteristic impedance of R_s.

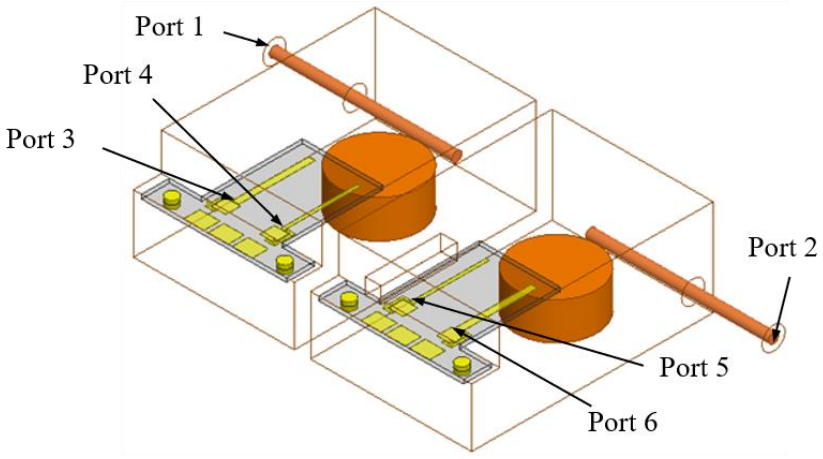

Figure 5-27 Simulation model showing port locations.

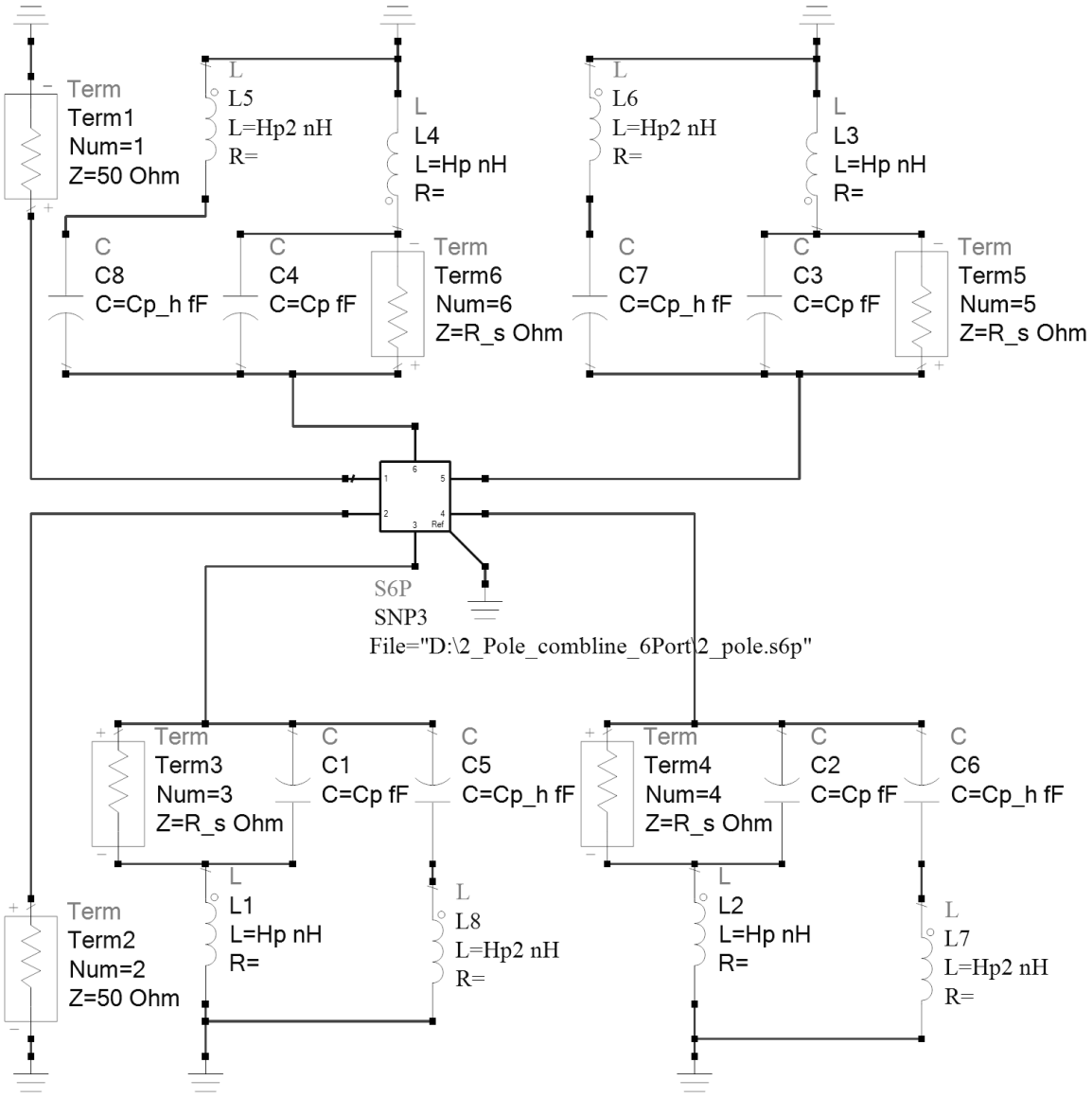

Figure 5-28 Simulation schematic with 6 ports.

Figure 5-30 depicts the simulated results with R_s assigned to 1 **Ω**, 4 **Ω**, 7 **Ω** and 10 **Ω**. The results show that the RF energy decreased by > 20 dB from port 1 (input port) to ports 3-6 (the ports where the VO_2 switches will be assembled) for R_s = 1 **Ω**. In other words, if the VO_2 switch has power handling of 30 dBm in the ON-state, the filter power handling limited by the VO_2 switch will be more than 50 dBm.

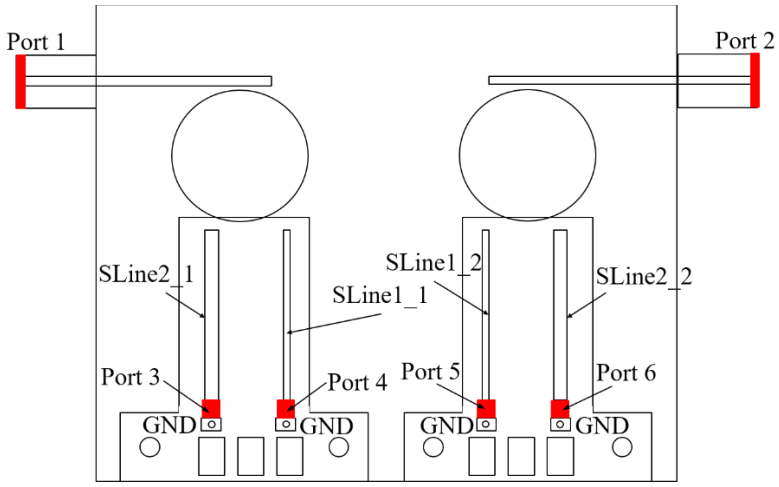

Figure 5-29 Top view of the simulation port setup for the two-pole filter.

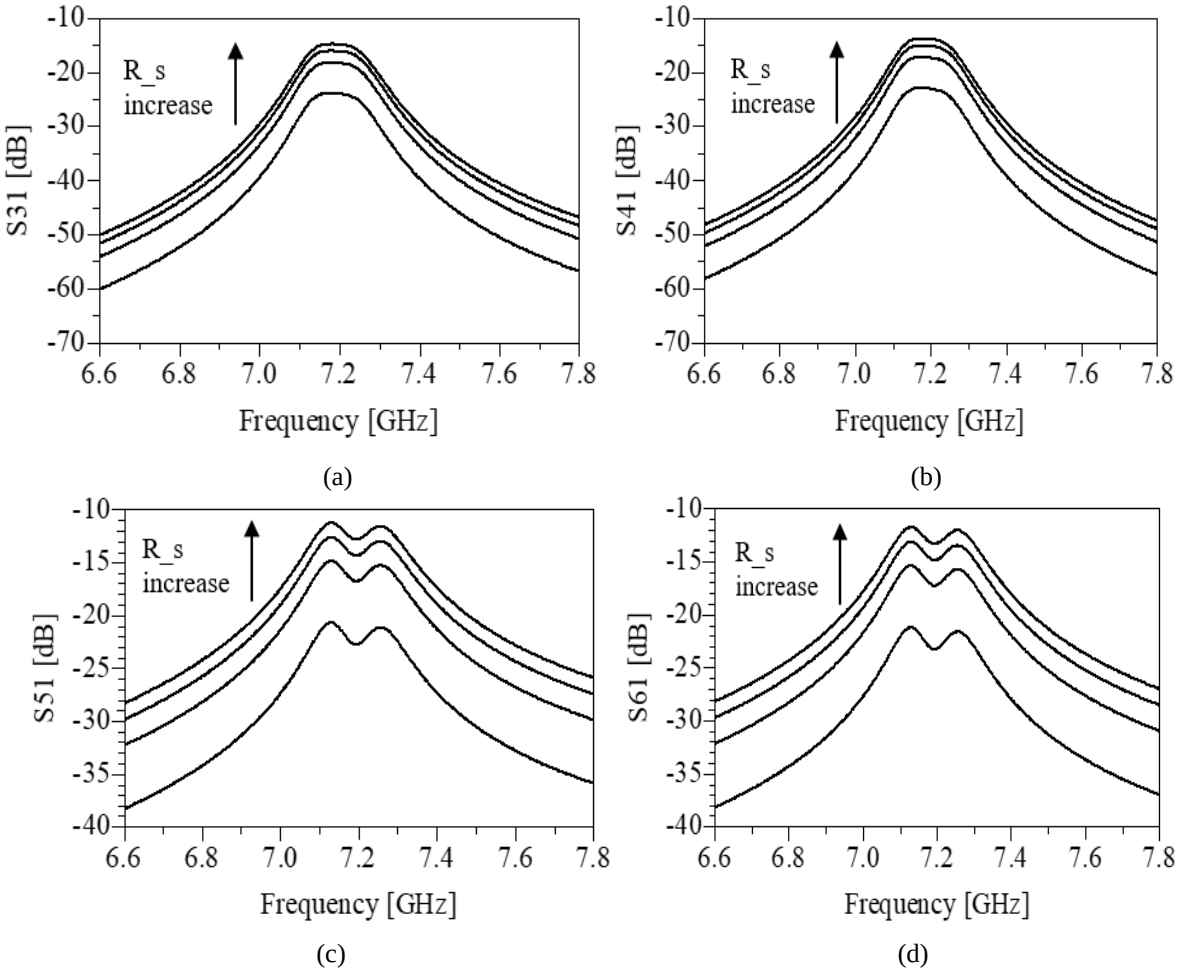

Figure 5-30 Simulated results with R_s assigned to 1 Ω, 4 Ω, 7 Ω and 10 Ω.

The simulated results with R_s assigned to 1 kΩ, 10 kΩ, 100 kΩ and 1 MΩ are shown in Figure 5-31. As can be seen, the RF energy from port 1 (input port) to ports 3-6 (the ports where the VO_2 switches will be assembled) is > 20 dB for R_s > 100 k Ω. It should be mentioned that the OFF-state power handling of the VO_2 switch is related to the OFF-state R_s, because as the R_s increases, the power handling increases, which in turn increases the power handling of the filter. With a high ON- and OFF-state resistance ratio (five orders of difference) for VO_2 film, the VO_2 switch can have an ON-state R_s of 1 Ω and an OFF-state R_s of 100 kΩ, which makes the filter power limitation of the filter due to the VO_2 switch more than 50 dBm. In this case, the limitation could be the cavity combline filter itself, based on the size and design parameters of the cavity.

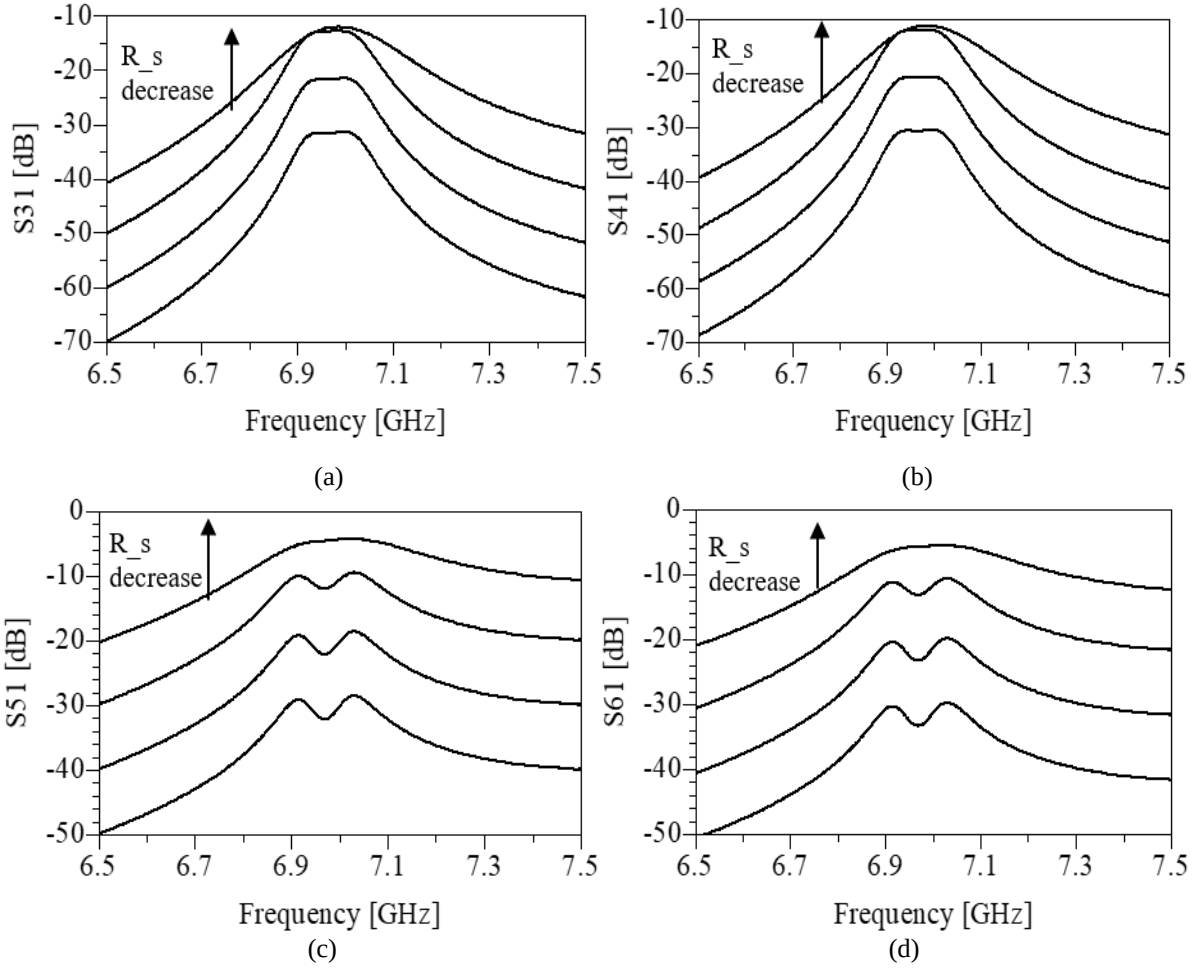

Figure 5-31 Simulated results with R_s assigned to 1 kΩ, 10 kΩ, 100 kΩ and 1 MΩ.

5.3 Tunable Dielectric Substrate-based Filter

In this section, a dielectric substrate-based tunable filter using VO_2 switches is presented. The dielectric substrates shown in Figure 5-32 are 2 inches × 2 inches × 1.5 mm, have a dielectric constant of 38, and a $Q \times f > 235{,}000$ [115], i.e., a $Q > 47{,}500$ at 5 GHz. These dielectric substrates can be accurately diced into small pieces with designed sizes using a dicing blade. Figure 5-33 shows a sample of the diced dielectric substrate. With a thickness of 1.5 mm, these dielectric substrates are thin enough to be used as a substrate for microfabrication. Since the roughness of the DSs is about 1 μm, however, additional polishing or process needs to be conducted before microfabrication can be done directly on these substrates.

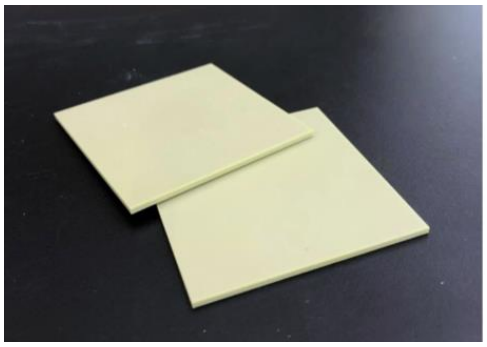

Figure 5-32 Dielectric substrates as ordered.

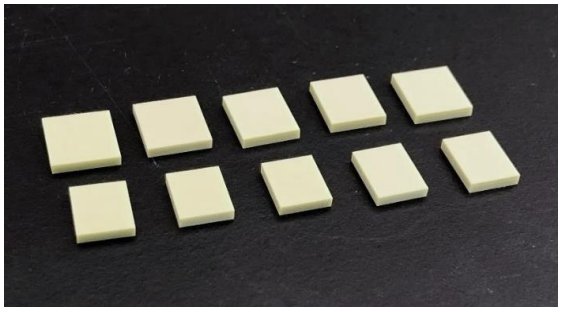

Figure 5-33 Diced dielectric substrates.

5.3.1 Design and Simulation Results

A dielectric filter design similar to that designed in Chapter 4 is employed to realize tunable dielectric filters. The 3D diagram of the three-pole tunable filter is shown in Figure 5-34. The filter contains two covers, input and output probes, six diced DSs, and a PCB with a tuning structure for holding the DSs. Coupling irises are designed on the covers for controlling the inter-resonator coupling. The DSs have a width of w_{DS} and a height of h_{DS}. All DSs are with the same height, while the width of the DSs is varied to adjust the resonance frequency of each resonator to account for iris loading.

The EM simulation model for the three-pole tunable filter is shown in Figure 5-35. The boundary of the airbox is assigned to aluminum. Figure 5-36 illustrates the simulated S-parameters of the filter. The simulated results are shown in Table 5-5. As can be seen, the filter demonstrates a tuning range of 240 MHz. The insertion loss varies from 0.121 dB to 0.131 dB, while the designed bandwidth is from 310 to 330 MHz, at a 20-dB return loss. The achievable *Q* is more than 1430 for all three states. A constant absolute bandwidth has been achieved (less than 5% over the tuning range).

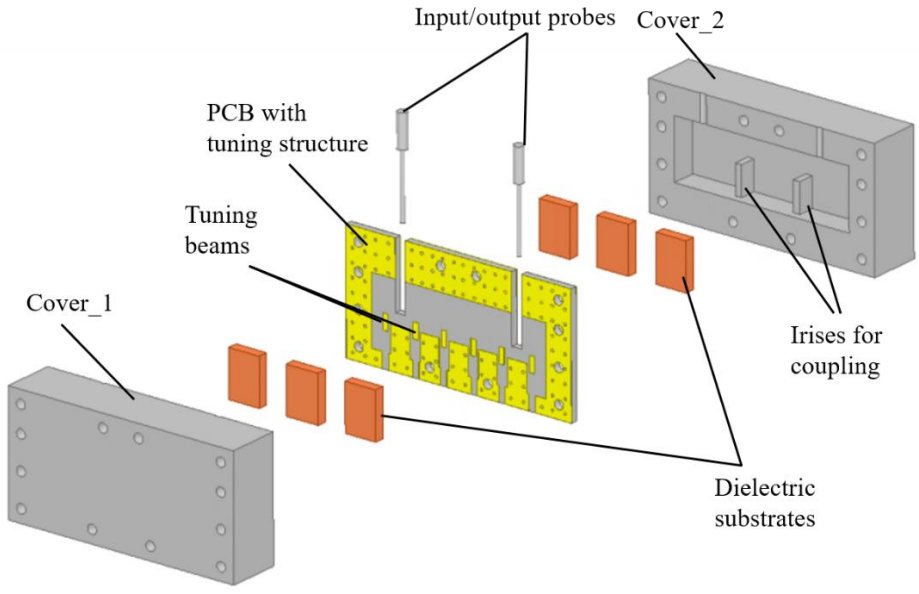

Figure 5-34 3D diagram of three-pole tunable filter.

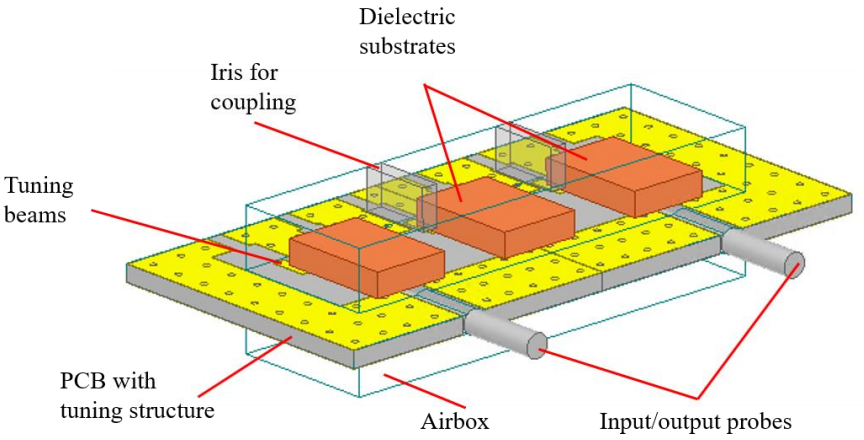

Figure 5-35 EM simulation model of three-pole tunable filter.

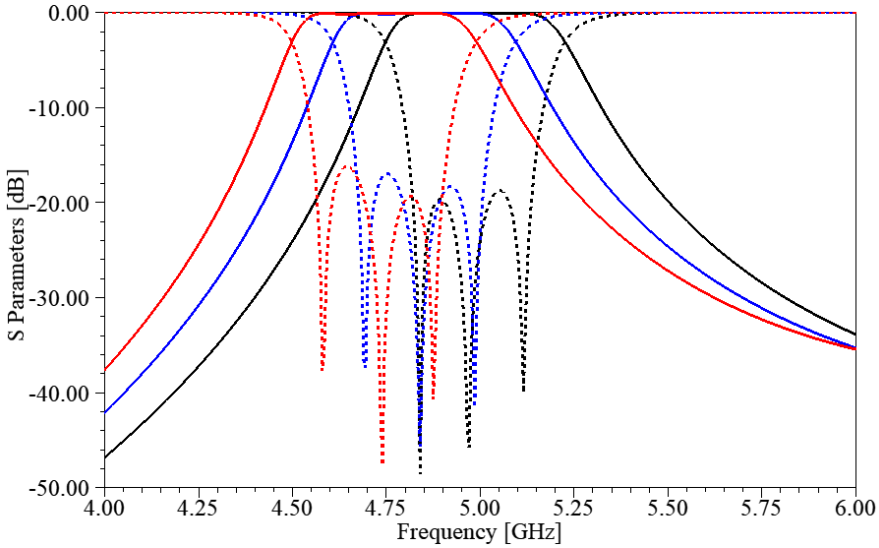

Figure 5-36 Simulation results for three-pole tunable filter.

Table 5-5 Simulation results for three-pole tunable filter

State	Frequency (GHz)	Bandwidth	Insertion Loss (dB)	Quality Factor
1. All tuning beams not connected to the ground	4.98	310 MHz @20dB return loss	0.131	1480
2. Half of the tuning beams connected to the ground	4.84	330 MHz @20dB return loss	0.125	1430
3. All tuning beams floating	4.74	330 MHz @20dB return loss	0.121	1440

5.3.2 Measurement Results with Wire Bonding

Figure 5-37 shows the images of the fabricated tunable filter. The VO_2 switches and DSs are first assembled on PCB with silver epoxy, as shown in Figure 5-37 (a) and (b). The DC bias wires are then soldered on PCB, as shown in Figure 5-37 (b). Figure 5-37 (c) illustrates how the PCB lies on one of the covers, while Figure 5-37 (d) depicts the assembled filter after assembling the covers and the PCB board.

The measurement results for the three-pole tunable filter with wire bonding to emulate the case of an ideal low loss switch are shown in Figure 5-38. The center frequency, insertion loss, and bandwidth are listed in Table 5-6. The measured results show that the filter can be tuned from 4.87 GHz to 5.16 GHz, with the insertion loss changing from 0.82 dB to 0.84 dB. The bandwidth at a 15-dB return loss varies from 284 MHz to 298 MHz. Figure 5-39 illustrates the measurement results for the three-pole tunable filter over a large span. The spurious free window is larger than 1.8 GHz.

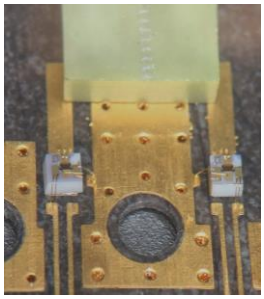

(a)

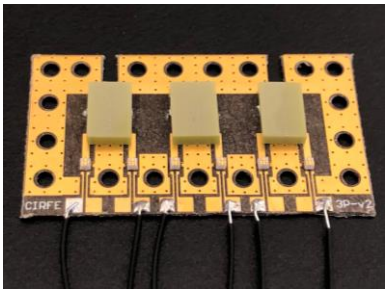

(b)

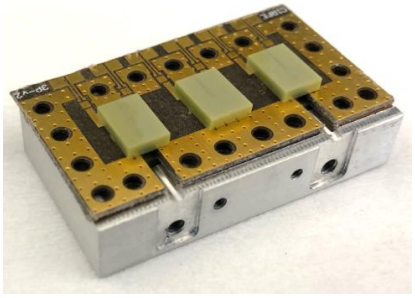

(c)

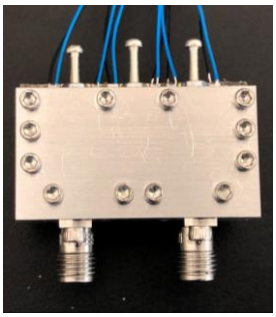

(d)

Figure 5-37 Image of fabricated three-pole tunable filter: (a) VO_2 switch on PCB; (b) full image of DSs and VO_2 switch assembled on PCB; (c) PCB on a cover; (d) assembled filter

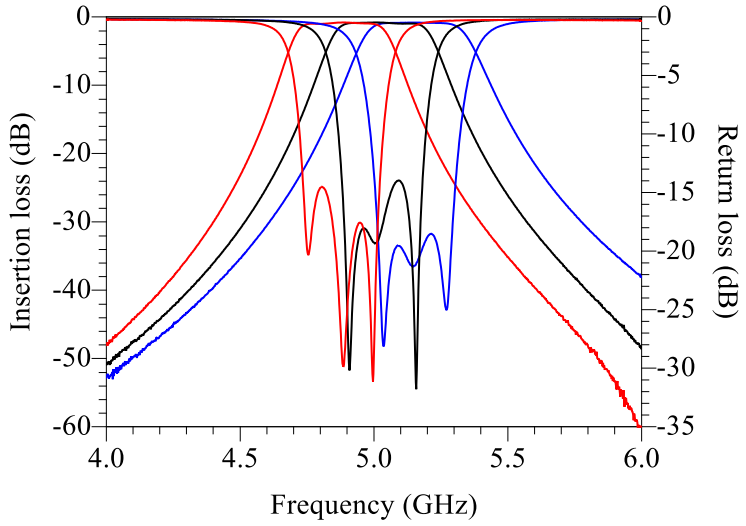

Figure 5-38 Measured results with wire bonding.

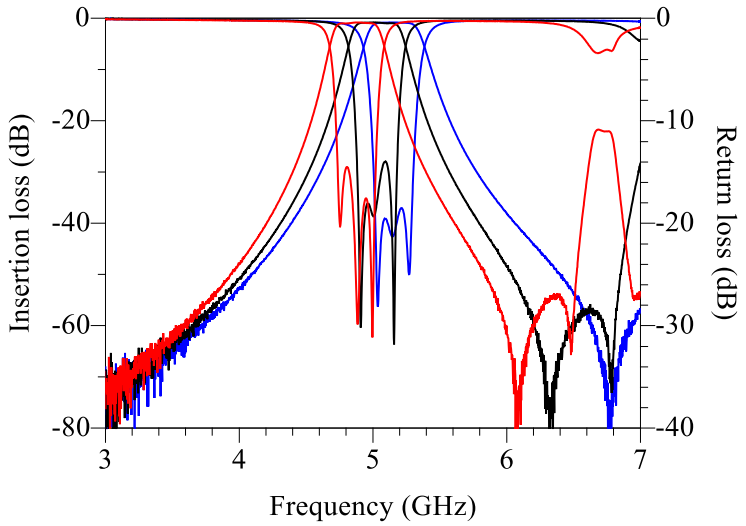

Figure 5-39 Measured results with wire bonding.

Table 5-6 Measured results for three-pole tunable filter with wire bonding

State	Center Frequency (GHz)	Bandwidth	Insertion Loss (dB)
1. All wires connected	4.87	284 MHz @15dB return loss	0.84
2. One wire connected	5.01	298 MHz @15dB return loss	0.82
3. No wires connected	5.16	296 MHz @15dB return loss	0.84

5.3.3 Measurement Results with VO_2 Switches

Figure 5-40 illustrates the measured results for the tunable filter with VO_2 switches. The bandwidth varies from 292 MHz to 330 MHz at a 10-dB return loss, the insertion loss varies from 4.34 dB to 5.36 dB. A tuning range of 240 MHz from 4.78 GHz to 5.02 GHz is demonstrated. The loss is mainly due to the adhesive used for assembling the DSs onto the PCB tuning circuit as well as the thin-film VO_2 not having high enough ON to OFF resistivity ratio. In order to improve the loss of the filter, low loss adhesive needs to be used. Also, the sputtering recipe for depositing thin-film VO_2 needs to be tuned for realizing high performance VO_2 switches.

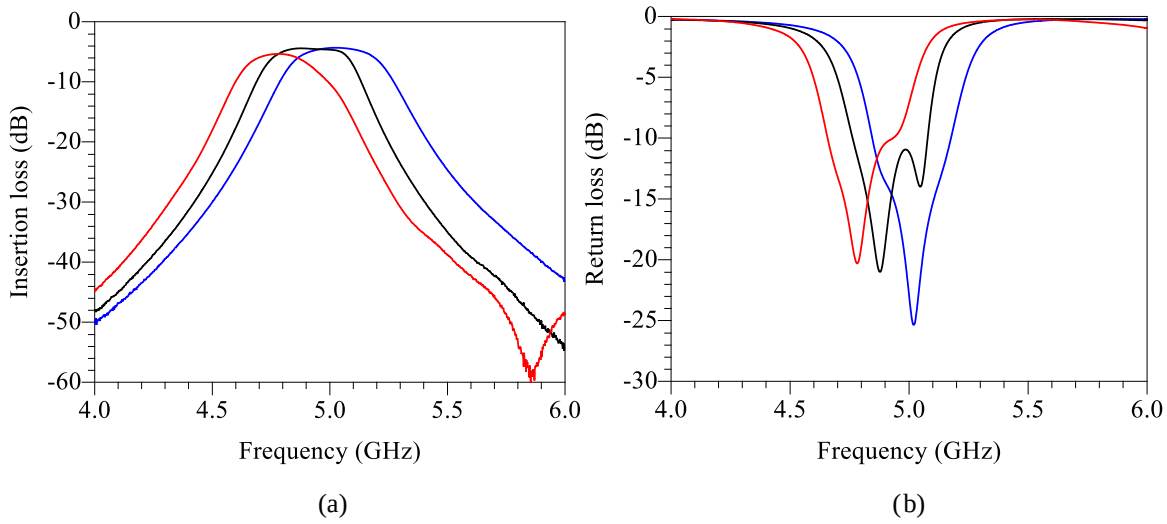

Figure 5-40 Measured results with VO_2 switch: (a) insertion loss; (b) return loss.

5.4 Summary

In this chapter, a tuning structure with multiple strip lines is proposed. The proposed tuning concept eliminates the need to use variable capacitor loading, which is known to degrade the filter's loaded *Q* over the tuning range. Two- and three-pole combline filters are designed, fabricated and measured with wire bonding, MEMS switches, and VO_2 switches. With wire bonding, all states demonstrate measured *Q* higher than 2000, while with VO_2 switches, the *Q*

varies from 500 to 680. The test data confirms the tunability and feasibility of using the proposed tuning scheme to realize high-*Q* tunable filters that maintain their *Q* value over the tuning range. A DS-loaded three-pole tunable filter is designed, fabricated, and measured. The results show the potential of realizing a tunable filter with relatively high *Q* with a very low-loss VO_2-based switch. A much better insertion loss can be potentially achieved with use of VO_2 switches with a low ON state resistance and a larger OFF state resistance. A better epoxy also needs to be used to assemble the DSs and VO_2 switch chips on the PCB tuning circuits.

Chapter 6
Conclusion

The main focus of this thesis has been on the research and development of MIT/PCM RF switches and their integration with RF passive devices, particularly high-*Q* three dimensional filters. The major contributions of the work are summarized below, followed by some of the unsolved research problems for future work.

6.1 Contributions of the Thesis

The major contributions of this thesis are as follows:

- Development of a fabrication process for VO_2/GeTe switches

  VO_2/GeTe-based RF switches have been fabricated using a microfabrication process developed on an alumina substrate. The simulation results show the potential for these switches to operate up to 75 GHz. The proposed fabrication process allows monolithic integration of VO_2/GeTe-based switches with a wide range of RF circuits.

- Development of reconfigurable RF passive devices integrating VO_2/GeTe switches

  VO_2-based variable attenuators operating over X-band and Ka-band have been designed, fabricated, and measured. A monolithic fabrication process for the VO_2-based attenuator on a single chip is described in detail. Micro-heaters using Cr are fabricated on the same chip for thermally actuating the thin-film VO_2. This variable attenuator promises to be useful in a wide range of millimeter wave applications. A 4-bit GeTe-based capacitor bank has also been designed, fabricated and measured. A monolithic fabrication process for the GeTe-based capacitor bank on glass substrate has been presented in detail, with the switchable capacitor integrated monolithically with GeTe switches. The presented capacitor bank is highly compact in size and offers a wide tuning range and the convenience of monolithic integration with other RF components.

- Development of a dielectric resonator filter employing dielectric substrates

  A novel configuration of a dielectric substrate-based cavity filter has been presented. The structure of the filter offers ease of assembly capable of realizing large bandwidth and exhibits a relatively thin profile. Five-, four-, and three-pole prototype filter DS-loaded filters using the proposed structure have been designed, fabricated, and measured. The fractional bandwidth of the five-pole filter is 9.6%, with a spurious located at roughly 1.5 f_0. The three-pole filter realized a fractional bandwidth of 13%. A Teflon-based mounting structure is proposed to improve the Q factor of this type of filter structure. The theoretical results promise a quality factor above 1800. The filter promises to be useful in low-cost, wideband applications, and amenable to integrating with MIT/PCM switches.

- Development of VO_2-based 3D tunable filters

  A tuning structure with multiple strip lines is proposed. The proposed tuning concept eliminates the need to use lumped element capacitors which are known to degrade the filter's loaded Q over the tuning range. Two- and three-pole filters with combline configurations are designed, fabricated and measured with wire bonding, MEMS switches, and VO_2 switches. A DS-loaded three-pole tunable filter is also designed, fabricated, and measured. The test

data confirm the tunability and potential integrating VO_2 switches with three dimensional high-*Q* filters.

6.2 Future Work

As discussed in Chapter 5, the performance (e.g., insertion loss, power handling, etc.) of tunable filters relies on the ON-state and OFF-state resistivity ratio of thin-film VO_2. In this work, we have used RF sputtering to deposit the thin-film VO_2, achieving a reasonably good resistivity ratio between the ON-state and OFF-state. In order to further improve the resistivity ratio, PLD may need to be used for obtaining thin-film VO_2 with a higher purity.

Integrating VO_2/GeTe switches and tuning structures directly on a dielectric substrate with micro-fabrication would be a compelling future research endeavor. This approach would require the dielectric substrates to have a roughness of preferably < 100 nm. Presently, however, the best dielectric substrates provided by vendors have a roughness greater than 1μm. Therefore, a process needs to be developed either to polish these substrates or to coat them with a buffer layer, such as SiO2, that can be polished to achieve a roughness of less than 100 nm.

Bibliography

[1] R. C. Cameron, C. M. Kudsia and R. R. Mansour, “Microwave Filters for Communication Systems - Fundamentals, Design and Applications,” *Wiley*, 2007.

[2] F. Hunag and R. R. Mansour, “Tunable compact dielectric resonator filters,”, *European Microwave Conf.*, Rome, Italy Sept. 2009.

[3] J. F. De Natale, P. J. Hood, and A. B. Harker, "Formation and characterization of grain-oriented V02 thin films," *J. Appi. Phys.* 66(12), 5844—5950 (1989).

[4] N. El-Hinnawy et al., “A Four-Terminal, Inline, Chalcogenide Phase-Change RF Switch Using an Independent Resistive Heater for Thermal Actuation,” *Electron Device Lett.*, Aug. 2013.

[5] M. Wang, Y. Shim, and M. Rais-Zadeh, "A Low-loss directly heated two-port RF phase change switch," *IEEE Electron Device Letters*, in press, 2014.

[6] M. Wang and M. Rais-Zadeh, ‘‘Directly heated four-terminal phase change switches,’’ in Proc. *IEEE MTT-S Int. Microw. Symp.*, Tampa, FL, USA, Jun. 2014, pp. 1–4.

[7] Y. Shim, G. Hummel, and M. Rais-Zadeh, “RF switches using phase change materials,” *IEEE 26th Int. Conf. MEMS*, Jan. 2013, pp. 237–240.

[8] N. El-Hinnawy, et al., "A 7. 3 THz cut-off frequency, inline, chalcogenide phase-change RF switch using an independent resistive heater for thermal actuation," *IEEE Compound Semiconductor Integrated Circuit Symposium (CSICS)*, Oct. 2013, pp. 1-4.

[9] A. Crunteanu, F. Dumas-Bouchiat, C. Champeaux, A. Catherinot, A. Pofhier, and P. Blondy, “Microwave switching functions using reversible Metal-Insulator Transition (MIT) in VO2 thin films,” *37th EUMC, Oct. 2007*, pp. 12–15.

[10] S.D. Ha, Y. Zhou, C. J. Fisher, S. Ramanathan, and J. P. Treadway, “Abrupt Insertion Loss Drop by RF-Triggering of the Phase Transition in VO2 CPW Switches”, *IEEE microwave and wireless components letters,* vol. 24, no. 8, August 2014.

[11] C. Hillman and P. Stupar, “An ultra-low loss millimeter-wave solid state switch technology based on the metal-insulator-transition of vanadium dioxide,” *Microw. Symp. Dig. IEEE MTT-S Int.,* 2014.

[12] K. Pan, K. Freeman, D. Brown. “Vanadium dioxide thin film series single-pole single throw switch” *IEEE National Aerospace and Electronics Conference,* NAECON, 27 June 2014.

[13] C. Hillman, P.A. Stupar, Z. Griffith. “VO2 Switches for Millimeter and Submillimeter-wave Applications.” *IEEE Compound Semiconductor Integrated Circuit Symposium (CSICS),* 2015.

[14] J. Givernaud, C. Champeaux, A. Catherinot, and A. Pothier, “Tunable band stop filters based on metal-insulator transition in vanadium dioxide thin films,” *Microw. Symp. Dig. 2008 IEEE MTT-S Int.,* pp. 1103–1106, 2008.

[15] D. Bouyge, A. Crunteanu, J.-C. Orlianges, et al. "Reconfigurable bandpass filter based on split ring resonators and vanadium dioxide (VO2) microwave switches," Asia Pacific *Microwave Conference, APMC,* Dec. 2009.

[16] D. Bouyge and A. Crunteanu, “Applications of vanadium dioxide (VO2)-loaded electrically small resonators in the design of tunable filters,” *Eur. Microw. Conf.,* 2010.

[17] W.A. Vitale, M. Fernandez-Bolans, C. F. Moldovan, A. Paone, et.al, “Tunable capacitors and microwave filters based on vanadium dioxide metal-insulator transition.” *Transducers 2015, Anchorage*, Alaska, USA, June 21-25, 2015

[18] Y. Zhu, S. Vegesna, Y. Zhao, V. Kuryatkov, M. Holtz, Z. Fan, M. Saed, and A. A. Vernussi. “Tunable dual-band terahertz metamaterial bandpass filters” *OPTICS LETTERS* / Vol. 38, No. 14 / July 15, 2013

[19] E. Merced, R. Cabrera, R. Suarez, F. E. Ferrnandez, and N. Sepulveda. “Nanostructured VO2 film coatings for tunable MEMS resonators.” *IEEE Nanotechnology Materials and Devices Conference* Oct 12 - 15, 2010, Monterey, California, USA, 2010.

[20] T.D. James, S. Earl, J. Valentine, T.J. Davis, J. McCallum, R.F. Haglund Jr and A. Roberts. “Vanadium Dioxide based tunable plasmonic antennas” *COMMAD* 2012.

[21] V. D. Kucharczyk, and T. Niklewski. “Accurate X-ray determination of the lattice parameters and thermal expansion coefficients of VO2 near the transition temperature” *J. Appl. Cryst. (1979).* 12, 370-373.

[22] F. J. Morin. “Oxides which show a metal-to-insulator transition at the neel temperature”. *Physical Review Letters* V. 3 No. 1 July 1st, 1959.

[23] Z. Yang, C. Ko and S. Ramanathan, "Oxide electronics utilizing ultrafast metal-insulator transitions," *Annual Review of Materials Research*, pp. 337-366, 2011.

[24] J. B. Goodenough, “The two components of the crystallographic transition in VO_2” *J. of Solid state chemistry* 3, 490-500(1971)

[25] Woong-Ki Hong, SeungNam Cha, Jung Inn Sohn, and Jong Min Kim, “Metal-Insulator Phase Transition in Quasi-One-Dimensional VO2 Structures,” Journal of Nanomaterials, vol. 2015, Article ID 538954, 15 pages, 2015. https://doi.org/10.1155/2015/538954.

[26] N. F. Mott, “Metal-insulator transition,” *Rev. Mod. Phys.*, vol. 40, no. 4, pp. 677–683, Oct. 1968.

[27] N. F. Mott, and Z. Zinamon. “The metal-nonmetal transition” *Rep. Prog. Phys.*, 1970, 33, 881-940

[28] G. Gruner. “The dynamics of charge-density waves”, *Reviews of Modern Physics*, Vol. 60, No. 4, October 1988

[29] F. Evers, “Andersion Transitions”, *REVIEWS OF MODERN PHYSICS*, VOLUME 80, OCTOBER–DECEMBER 2008.

[30] M.W. Haverkort et al. “Orbital-Assisted Metal-Insulator Transition in VO2” *Phys. Rev. Lett. 95*, 196404 (2005).

[31] T. C. Koethe et al. “Transfer of Spectral Weight and Symmetry across the Metal-Insulator Transition in VO2” *Phys. Rev. Lett.* 97, 116402 (2006).

[32] S. Biermann et al. “Dynamical Singlets and Correlation-Assisted Peierls Transition inVO2” *Phys. Rev. Lett.* 94, 026404 (2005).

[33] M.F. Becker, A.B. Buckman, et al. “Femtosecond laser excitation of the semiconductor-metal phase-transition in VO2.” *Appl. Phys. Lett.* 65:1507–9, 1994

[34] A. Cavalleri, T. Dekorsy, H. Chong, et. al. “Evidence for a structurally driven insulator-to-metal transition in VO2: a view from the ultrafast timescale.” *Phys. Rev. B* 70:161102, 2004

[35] C. Kubler, H. Ehrke, R. Huber, et al. “Coherent structural dynamics and electronic correlations during an ultrafast insulator-to-metal phase transition in VO2.” *Phys. Rev. Lett.* 99:116401,2007

[36] H. Kim, Y. Lee, B. Kim, et al. “Monoclinic and correlated metal phase in VO2 as evidence of the Mott transition: coherent phonon analysis.” *Phys. Rev. Lett.* 97:266401, 2006

[37] V. Lobastov, J. Weissenrieder, J. Tang, A. Zewail. “Ultrafast electron microscopy (UEM): four-dimensional imaging and diffraction of nanostructures during phase transitions.” *Nano Lett.* 7:2552–58, 2007

[38] Raleigh, “Switching Applications Based on Reversible Insulator-Metal Transition of Vanadium Dioxide Thin Films Synthesized by Pulsed Laser Deposition” Ph.D. thesis North Carolina 2013.

[39] D.H. Kim, H.S. Kwok, “Pulsed laser deposition of VO2thin films,” *Appl. Phys. Lett.* 65 (1994) 3188–3190.

[40] G. Stefanovich, A. Pergament, and D. Stefanovich, “Electrical switching and Mott transition in VO2,” *Journal of Physics: Condensed Matter*, vol. 12, p. 8837, 2000.

[41] S. D. Ha, Y. Zhou, C. J. Fisher, S. Ramanathan, J. P. Treadway, "Abrupt insertion loss drop by RF-triggering of the phase transition in VO2 CPW switches, Vol. 24, No. 8, AUGUST 2014.," IEEE Microwave and Wireless Components Letters, vol. 24, no. 8, pp. 575 - 577, Aug. 2014.

[42] M. K. Liu,B. Pardo, J. Zhang, M. M. Qazilbash,Sun Jin Yun,Z. Fei, Jun-Hwan Shin, Hyun-Tak Kim,D. N. Basov,and R. D. Averitt, “Photoinduced Phase Transitions by Time-Resolved Far-Infrared Spectroscopy in V2O3” *Physical review letters*, PRL 107, 066403 (2011)

[43] M. Kang, I. Kim, S. W. Kim, J. Ryu, and H. Y. Park, “Metal-insulator transition without structural phase transition in V2O5 film” *APPLIED PHYSICS LETTERS* 98, 131907 _2011.

[44] H. Katzke, P. Toledano, and W. Depmeier, “Theory of morphotropic transformations in vanadium oxides” *PHYSICAL REVIEW B* 68, 024109 (2003)

[45] W. A. Vitale, C. F. Moldovan, a. Paone, A. Schuler, and A. M. Ionescu, “Fabrication of CMOS-compatible abrupt electronic switches based on vanadium dioxide”, *Microelectronic Engineering*, 145 (2015) 117-119.

[46] D. Ruzmetov, K. T. Zawilski, V. Narayanamurti, and S. Ramanathan, “Structure-functional property relationships in rf-sputtered vanadium dioxide thin films” *JOURNAL OF APPLIED PHYSICS* 102, 113715 _2007.

[47] M. B. Sahana, G. N. Subbanna, and S. A. Shivashankar, “Phase transformation and semiconductor-metal transition in thin films of VO 2 deposited by low-pressure metalorganic chemical vapor deposition” *JOURNAL OF APPLIED PHYSICS* V. 92, No. 11 1 DECEMBER 2002.

[48] Y.K. Dou, J.B. Li, M.S. Cao, D.Z. Su, F. Rehman, J.S. Zhang, H.B. Jin," Oxidizing annealing effects on VO2films with different microstructures" *Appl. Surf. Sci.* 345 (2015) 232e237.

[49] B. G. Chae, H. T. Kim, and S. J. Yun," Characteristics of W- and Ti-Doped VO2 Thin Films Prepared by Sol-Gel Method" *Electrochemical and Solid-State Letters,* 11 _6_ D53-D55 _2008.

[50] F.H. Chen, L. L. Fan, S. Chen,G. M. Liao,Y. L. Chen,P. Wu, Li Song, C. W. Zou, and Z. Y. Wu, "Control of the Metal−Insulator Transition in VO2 Epitaxial Film by Modifying Carrier Density", *ACS Appl. Mater.* Interfaces 2015, 7, 6875−6881.

[51] R. G. Mani and S. Ramanathan, "Observation of a uniform temperature dependence in the electrical resistance across the structural phase transition in thin film vanadium oxide (VO_2)" *APPLIED PHYSICS LETTERS* 91, 062104 _2007.

[52] J. A. Thornton, "Plasma-assisted deposition processes: Theory mechanisms and applications" *Thin Solid Films,* 107(1983) 3-19.

[53] J. Nag and R F H. Jr, "Synthesis of vanadium dioxide thin films and nanoparticles" *J. Phys.: Condens. Matter* 20 (2008) 264016 (14pp)

[54] Thornton J A 1983 Plasma-assisted deposition processes—theory, mechanisms and applications Thin Solid Films 107 3–19

[55] C.Y. Khoo, H. Liu, W.A. Sasangka, R.I. Made, N. Tamura, M. Kunz, A.S. Budiman, C.L. Gan, C.V. "Thompson Impact of deposition conditions on the crystallization kinetics of amorphous GeTe films" *J. Mater. Sci.,* 51 (4) (2016), pp. 1864–1872

[56] A. H. Gwin, C. H. Kodama, T.V. Laurvick, R. A. Coutu Jr., and P. F. Taday, "Improved terahertz modulation using germanium telluride (GeTe) chalcogenide thin films", *Applied Physics Letters* 107, 031904 (2015).

[57] E. Gouvest, C. Vallee, P. Michallon et al. "Plasma Enhanced Chemical Vapor Deposition of Conformal GeTe Layer for Phase Change Memory Applications," *Journal of Solid State Science and Technology*, 1 (6) Q119-Q122 (2012)

[58] M. Bouska, S. Pechev, Q. Simon, R. Bidin, et.al. "Pulsed laser deposited GeTe-rich GeTe-Sb2Te3 thin films" *Scientific Reports,* 2016.

[59] S. Jung, S. Yoon, Y. Park, S. Lee, and B. Yu. "Control of the Thickness and the Length of Germanium-Telluride Nanowires Fabricated via the Vapor-Liquid-Solid Method" *Journal of the Korean Physical Society,* Vol. 54, No. 2, February 2009, pp. 653-659.

[60] Zhou, J. D.; Gao, Y. F.; Zhang, Z. T.; Luo, H. J.; Cao, C. X.; Chen, Z.; Dai, L.; Liu, X. L. "VO2 thermochromic smart window for energy savings and generation" *Sci. Rep.* 2013, 3, 3029.

[61] K. Takebe, Y. Ikeshima, H. Miyashita, K. Takano, M. Hangyo and S.-S. Lee, "Design of H-shaped fractal antenna for microbolometer and its thermal performance estimation". *ELECTRONICS LETTERS* 25th September 2014 Vol. 50 No. 20 pp. 1410–1412.

[62] M. N. F. Hoque, G. Karaoglan-Bebek, M. Holtz, A. A. Bernussi, and Z. Fan, "High performance spatial light modulators for terahertz applications" *Opt. Commun*. 350, 309 (2015).

[63] A. Dhawan, Y. Sharma, L. Brickson and J. F. Muth, "Incorporation of vanadium oxide films in optical fibers for temperature sensing and optical switching applications" *Opt. Mater. Express,* 2014, 4(6), 1128–1139.

[64] M. Currie, V. D. Wheeler, M. G. Ancona, T. Feygelson, and K. D. Hobart, "Optical switching and thermal recovery of vanadium dioxide," *OSA Technical Digest* (Optical Society of America, 2018)

[65] M. Agaty, A. Crunteanu, C. Dalmay, et. al. "Ku Band High-Q Switchable Cavity Filter Using Vanadium Dioxide (VO2) Microwave Disk-Shaped Switch" *48th European Microwave Conference*, EuMC 2018.

[66] M. Wang, F. Lin, and M. Zadeh. "An X-band reconfigurable bandpass filter using phase change RF switches" *2016 IEEE 16th Topical Meeting on Silicon Monolithic Integrated Circuits in RF Systems (SiRF).*

[67] A. Ghalem, C. Guines, et. al, "Reversible, Fast Optical Switching of Phase Change Materials for Active Control of High-Frequency Functions" *IEEE MTT-S International Microwave Symposium Digest,* June 2018, pp. 839-842.

[68] G. M. Rebeiz, "RF MEMS–Theory, design and technology", *John Wiley & Sons*, 2003.

[69] H. Madan, H-T. Zhang, M. Jerry, et. al. "26.5 Terahertz electrically triggered RF switch on epitaxial VO2-on-Sapphire (VOS) Wafer" 2015 *IEEE International Electron Devices Meeting (IEDM),* 9.3.1-9.3.4.

[70] M. Wang, F. Lin, and M. Rais-zadeh. "Comparison and analysis of GeTe-Based Phase change RF switch Structures and Modeling of Their Power Handling Capability" web.eecs.umich.edu/~minar/pdf/27-1.pdf.

[71] S. Fouladi, F. Huang, D. Yan and R. R. Mansour, "Combline Tunable Bandpass Filter Using RF-MEMS Switched Capacitor Bank," *IEEE MTT-S Int. Microw. Symp. Tech. Dig.*, pp. 1 – 3, June 2012.

[72] Z. Yang, D. Psychogiou, and D. Peroulis, "design and optimization of tunable silicon-integrated evanescent-mode bandpass filters" *IEEE Trans. Microwave Theory & Tech.,* vol. 66, no. 4, pp. 1790-1803, April 2018.

[73] S. Park, I. Reines, C. Patel, and G. M. Rebeiz, “High-Q RF-MEMS 4-6-GHz tunable evanescent-mode cavity filter” *IEEE Trans. Microwave Theory & Tech.,* vol. 58, no. 2, pp. 381-389, February 2010.

[74] J. Jiang, G. Chugunov, and R. R. Mansour, “Fabrication and characterization of VO2-based series and parallel RF switches” *IEEE MTT-S International Microwave Symposium Digest*, June 2017, pp. 278-280.

[75] V. D. Kucharczyk, and T. Niklewski. “Accurate X-ray determination of the lattice parameters and thermal expansion coefficients of VO_2 near the transition temperature” *J. Appl. Cryst.* (1979). 12, 370-373.

[76] Fewa C. Hillman, P.A. Stupar, Z. Griffith. “VO_2 Switches for Millimeter and Submillimeter-wave Applications.” *IEEE Compound Semiconductor Integrated Circuit Symposium* (CSICS), 2015.

[77] K. Pan, W. Wang, E. Shin, K. Freeman, and G. Subramanyam, “Vanadium oxide thin-film variable resistor-based RF switches” *IEEE Transactions on Electron Devices*, Vol. 62, No. 9, Sept. 2015.

[78] ICSPI Corp., nGuage AFM system. http://www.icspicorp.com/.

[79] C. R. Trent, and T. M. Weller, “S-band reflection type variable attenuator,” *IEEE Micro. Wireless Compon. Lett*., Vol. 12, No. 7, pp. 243-245, Jul. 2002.

[80] C. Wang, H. Wu, M. Chiang, and C. Tzuang, “A 24 GHz CMOS Miniaturized Phase-Invertible Variable Attenuator Incorporating Edge-Coupled Synthetic Transmission Lines” *IEEE MTT-S Int. Microw. Symp. Dig*, pp. 841-844, 2009.

[81] K. Sun, M. K. Choi, and D. Weide, “A PIN diode controlled variable attenuator using a 0-dB branch-line coupler” *IEEE Micro. Wireless Compon. Lett*., Vol. 15, No. 6, pp. 440-442, Jun. 2005.

[82] L. Pierantoni, D. Mencarelli, M. Bozzi, R. Moro and S. Bellucci, “Graphene-based Electronically tunable microstrip attenuator” *IEEE MTT-S Int. Microw. Symp. Dig.*, pp. 1-3, Jun. 2014.

[83] L. Pierantoni, D. Mencarelli, M. B， R.Moro， S.M， et. al., “Broadband microwave attenuator based on few layer graphene flakes” *IEEE Transactions on Microwave Theory and Techniquies*, Vol. 63, No. 8, Aug. 2015

[84] J. Givernaud, A. Crunteanu, J. Orlianges, A. Pothier, C. Champeaux, A. Catherinot, et al., "Microwave Power Limiting Devices Based on the Semiconductor–Metal Transition in Vanadium–Dioxide Thin Films," IEEE Tans. Microw. Theory & Tech., vol. 58, no. 9, pp. 2352-2361, Aug. 2010.

[85] J. Jiang, R. R. Mansour, and K. Wong, “A VO_2-Based 30 GHz Variable Attenuator,” *IEEE MTT-S International Microwave Symposium*, Hawaii, June 2017.

[86] P. R. Herczfeld, A. S. Daryoush, A. Rosen, A. K. Sharma, and V. M. Contarino, “Indirect subharmonic optical injection locking of a millimeter-wave IMPATT oscillator,” *IEEE Trans. Microw. Theory Tech.,* vol. 34, no. 12, pp. 1371–1376, Dec. 1986.

[87] http://www.psemi.com/.

[88] Cavendish Kinetics. (2012). [Online]. Available: http://www.cavendishkinetics.com.

[89] A. A. Aziz and R. R. Mansour, “Design, fabrication and characteri-zation of compact 4-bit RF MEMS capacitor bank in standard CMOS 0.35μm process” *IEEE MTT-S Int. Microw, Symp, Dig.,* Jun. 2017.

[90] J. Moon, et al., “11 THz Figure-of-Merit Phase-change RF Switch-es for Reconfigurable Wireless Front-ends” *IEEE MTT-S Int. Mi-crow. Symp. Dig.,* May 2015.

[91] N. EI-Hinnawy, et al., “12.5 THz Fco GeTe Inline Phase-Change Switch Technology for Reconfigurable RF and Switching Applications” *IEEE Compound Semiconductor Integrated Circuit Symposium (CSICS),* 2014.

[92] M. Wang, F. Lin, and M. Rais-Zadeh., “Need a Change? Try GeTe: A Reconfigurable Filter Using Germanium Telluride Phase Change RF Switches” *IEEE Microwave Magzine,* Vol. 17, Issue 12, Dec. 2016.

[93] J. Jiang, and R. R. Mansour, “Design, fabrication and characterization of a PCM-based compact 4-bit capacitor bank,” *IEEE MTT-S International Microwave Symposium*, Philadelphia, June 2018.

[94] A. E. Williams, “A Four-Cavity Elliptic Waveguide Filter,” *IEEE Trans. Microw. Theory Tech.,* vol.18, no. 12, pp. 1109-1114, Dec. 1970.

[95] K. Zhou, J. Ding, C. Zhou, and W. Wu, “W-band dual-band quasi-elliptical waveguide filter with flexibly allocated frequency and bandwidth ratios,” *IEEE Microw. Wireless Compon. Lett.,vol.* 28, Issue 3, pp. 206-208, Mar. 2018.

[96] X. Wang, and K. Wu, “A TM01 mode monoblock dielectric filter,” *IEEE Trans. Microw. Theory Tech.,* vol.62, no. 2, pp. 275-281, Jan. 2014.

[97] C. Wang, H. W. Yao, K. A. Zaki, and R. R. Mansour, “Mixed modes cylindrical planar dielectric resonator filters with rectangular enclosure,” *IEEE Trans. Microw. Theory Tech.,* vol. 43, no. 12, pp. 2817–2823, Dec. 1995.

[98] X. Chen, K. Wu, “Self-packaged sillimeter-save substrate integrated waveguide filter with asymmetric frequency response,” *IEEE Trans. Compon. Packag. Manuf. Technol.,* vol. 2, no. 5, pp. 775–782, May 2012.

[99] J. Jiang, and R. R. Mansour, “High-Q tunable filter with a novel tuning structure,” *46th Euro. Micro. Conf.,* London, UK, Oct. 2016.

[100] R. R. Mansour, “Fiter Technologies for wireless base station,” *IEEE Micro. Mag.*, pp. 68-74 Mar. 2004.

[101] C. Tomassoni, S. Bastioli, and R. V. Snyder, “Compact mixed-mode filter based on TE101 cavity mode and TE01δ dielectric mode,” *IEEE MTT-S Intl. Micro. Sym., San Francisco*, CA, USA, Aug. 2016.

[102] V. Nocella, L. Pelliccia, C. Tomassoni, and R. Sorrentino, “Miniaturized dual-band waveguide filter using TM dielectric-loaded dual-mode cavities,” *IEEE Microw. Wireless Compon*. Lett.,vol. 26, Issue 5, pp. 310-312, Apl. 2016.

[103] P. Rezaee, M. Hoft, “A new class of compact dual-mode dielectric resonator filters,” *IEEE MTT-S Intl. Micro. Sym.,* San Francisco, CA, USA, Aug. 2016.

[104] R. Zhang, and R. R. Mansour, “Low-cost dielectric-resonator filters with improved spurious performance,” *IEEE Trans. Microw. Theory Tech.,* vol.55, no. 10, pp. 2168-2175, Oct. 2007.

[105] M. S. Bakr, I. C. Hunter, and W. Bosch, “Miniature triple-mode dielectric resonator filters” *IEEE MTT-S Intl. Micro. Sym.,* Philadelphia, PA, USA, Jun. 2018.

[106] M. S. Bakr, I. C. Hunter, and W. Bosch, “Miniature triple-mode dielectric resonator filters” *IEEE Trans. Microw. Theory Tech.,* vol.66, no. 12, pp. 5625-5632, Dec. 2018.

[107] M. S. Bakr, I. C. Hunter, and W. Bosch, "Broadband dual-mode dielectric resonator filters," in *ICMMWT*, Chengdu, 2018.

[108] https://www.2spi.com/catalog/documents/05001-2SilverConPaint_RoHS2-20190430.pdf

[109] Y. Marchives, N. Delhote, S. Verdeyme, and P. M. Iglesias, “Wide-band dielectric filter at C-band *manufactured* by stereolithography,” *44th Euro. Micro. Conf., Rome*, Italy, Dec. 2014.

[110] F. Huang, S. Fouladi, and R. Mansour, “Hi-Q tunable dielectric resonator filters using MEMS *technology*” *IEEE Trans. Microwave Theory & Tech.,* vol. 59, no. 12, pp. 3401-3409, December 2011.

[111] S. J. Park, I. Reines, C. Patel, and G. M. Rebeiz, “High-Q RF-MEMS 46-GHz tunable evanescent-mode cavity filter,” *IEEE Trans. Microwave Theory & Tech.,* vol. 58, no. 2, pp. 381-389, February 2010.

[112] R. Stefanini, M. Chatras, A. Pothier, C. Guines, P. Blondy. "High-Q 3D tunable RF MEMS filter with a constant fractional bandwidth," *Microwave Integrated Circuits Conference (EuMIC),* 2013 European , vol. 6.,no. 8, pp. 312-315, October, 2013.

[113] J. Givernaud, A. Crunteanu, A. Pothier, C. Champeaux, A. Cath- erinot, and P. Blondy, "CPW self-resetting power limiting devices based on microwave power induced semiconductor-metal transi- tion in vanadium dioxide," *IEEE MTT-S Int. Microwave Symp. Dig.*, Boston, MA, 2009, pp. 109–112.

[114] S. Pi, M. Ghadiri-Sadrabadi, J. C. Bardin, and Q. Xia, "Nanoscale memristive radiofrequency switches" *Nat. Commun.*, vol. 6, no. 7519, pp. 1–9, June 2015.

[115] http://www.mcv-microwave.com/mcv-catalog-substrate-052714.pdf